UHV STUDIES OF THE ADSORPTION OF SMALL ADSORBATE MOLECULES ON LOW INDEX PLATINUM SINGLE CRYSTALS

By

Christopher John Baily

A thesis submitted for the degree

of doctor of philosophy

Department of Chemistry

August 2003

Acknowledgements

Firstly, I would like to thank Dr. Andrea Russell for all of her assistance, encouragement and ideas during the course of my PhD. I would also like to thank Dr. Mark Surman for his enthusiasm and help during my experimental beamtime at Daresbury.

A big thanks goes to Adrian, Barry, and Nic at Daresbury, and to Barbara at Imperial for all their wonderful help with the calculations, and for taking time to explain the theory to a sometimes-confused experimentalist.

I would like to thank the EPSRC for the research studentship. Thanks also go to past and present members of the Russell and Hayden groups at Southampton for generally keeping me sane and being great friends; in particular, Tim – for his help with UHV and RAIRS and introducing me to the sport of rugby league, Fabrice – for making me feel welcome when I first joined the group, Mike – for help with UHV and electrochemistry problems and for being a friend I know I can trust, Abbe – for help with running CV's, being great fun to be around (verging on the edge of insane at times!) and scoffing Jaffa cakes, Scott – for helping with UHV difficulties and sending me amusing emails while I'm writing up, and Oli for help with ruthenium solutions and being a good laugh.

Finally, I would like to thank my parents for all the support, both emotional and financial, they have given me throughout my entire life, and especially at university. The biggest thanks of all goes to Frances. Without your constant encouragement (not nagging!) and helpful words the last three and a half years would have been significantly more difficult. Thanks xx.

Abstract

The aim of this thesis was to investigate the bonding of small adsorbate molecules to platinum single crystal surfaces using UHV synchrotron far-infrared RAIRS and DFT calculations. The use of UHV synchrotron far-infrared RAIRS enabled the substrate-adsorbate vibration to be observed in a data collection time of a few minutes. The principal adsorbate molecule that was studied was carbon monoxide because of its large infrared absorption factor and its importance in the fuel cell process. DFT calculations were used to confirm the conclusions drawn from the RAIRS experiments.

When CO was adsorbed in a $c(4 \times 2)$ arrangement on Pt(111) at 260 K, two peaks were observed at 376 cm^{-1} and 464 cm^{-1}. These peaks were assigned to the Pt-CO stretch of CO adsorbed in bridge and atop sites respectively. There was no sign of a Fermi resonance in the bridging peak. The distinct difference in the energies of the Pt-CO stretches highlights the sensitivity of the Pt-CO stretching vibration to the local bonding environment

Studies were also carried out on the CO induced lifting of the Pt(110)-(1×2) reconstruction. It was shown that two distinct Pt-CO bands are present depending on whether the CO is bonded to the reconstructed surface (466 to 469 cm^{-1}) or the unreconstructed surface (475 to 478 cm^{-1}). The high sensitivity of RAIRS also allowed the lifting of the reconstruction to be detected at a temperature some 50 K lower than previously reported.

The first far-infrared RAIRS observation of the Pt-benzene stretch for benzene adsorbed on the Pt(110) surface at room temperature is also reported (310 cm^{-1}). Also, an electrochemical transfer system was designed and built onto an existing UHV chamber. This will allow *ex-situ* experiments, such as cyclic voltammetry, to be used in conjunction with UHV experiments, such as XPS and RAIRS, to better understand the interactions between adsorbates and substrates.

Table of Contents

Chapter One – Introduction

This thesis is primarily concerned with the bonding of carbon monoxide to platinum, which is of considerable technological importance because CO acts as a potent poison of platinum fuel cell catalysts. Through a series of experiments presented in this thesis the nature of the Pt-CO bond has been probed by the use of far-infrared RAIRS (reflection absorption infrared spectroscopy) and by complementary *ab initio* calculations.

1.1 The development of fuel cells

In recent years there has been an environmental and economic push to find an alternative to the combustion engine. Environmental issues such as global warming and atmospheric pollution are at the forefront of society's mind, with the combustion engine being one of the major contributors to these problems. Also, the increased use of combustion engines to power vehicles leads to a greater dependency on fossil fuels. As fossil fuels are a non-renewable source of energy the combustion engine using fossil fuels can only continue to exist for a finite time. The combination of the depletion of fossil fuel reserves with public concerns over the safety and disposal of nuclear fuels and waste materials has led to fuel cells emerging as a viable alternative. William Grove produced the first working fuel cell in 1839, but it was not until the 1960's that their potential was recognised and concerted programs of research were initialised [1].

Fuel cells produce electrical energy, which can be used to power a motor vehicle, by the electrochemical oxidation of a chosen fuel at the anode and the reduction of oxygen at the cathode [2]. Since these two reactions occur at the two separate electrodes the fuel cell is a very clean way of producing electrical energy. The electrodes are separated by an ionically conducting electrolyte that completes

the circuit to form a single cell. A number of single cells (normally 10 to 100) can then be combined in series or parallel to form the working stack.

There are six different types of fuel cell, each with different operating conditions and therefore different possible commercial applications. They are:

- Proton Exchange Membrane Fuel Cell (PEMFC)
- Direct Methanol Fuel Cell (DMFC)
- Alkaline Fuel Cell (AFC)
- Phosphoric Acid Fuel Cell (PAFC)
- Molten Carbonate Fuel Cell (MCFC)
- Solid Oxide Fuel Cell (SOFC)

The PEMFC [2] and DMFC both run at the lowest temperature of all six fuel cells (60 – 90 °C, compared to well above 100 °C in the other fuel cells) giving them particular relevance to transport applications, and so will be discussed in greater detail. Information on the other high temperature fuel cells can be found in a review by Appleby [3].

The PEMFC single cell, shown in Figure 1.1, consists of two electrodes separated by a solid polymer electrolyte membrane [4, 5]. The fuel and oxidant are allowed to pass separately over the anode and cathode respectively. The fuel used is hydrogen, which is oxidised at the anode as displayed in Equation 1.1 [4]. Air is supplied to the cathode where the reduction of oxygen occurs according to Equation 1.2.

Anode	$H_2 \rightarrow 2H^+ + 2e^-$	Equation 1.1
Cathode	$\frac{1}{2}O_2 + 2H^+ + 2e^- \rightarrow H_2O$	Equation 1.2

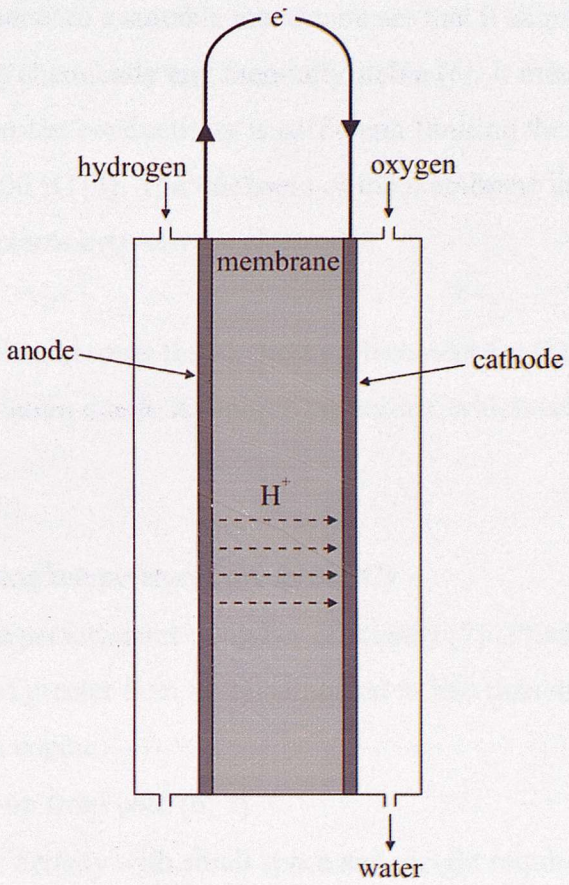

Figure 1.1 – Main components of the PEMFC

The electrode catalysts are platinum-based in both cases [4]. In general, platinum black or platinum on a carbon support are used. Platinum is chosen due to the high current densities obtained and due to its inherent stability within the fuel cell operating conditions.

The polymer electrolyte membrane was initially a cross-linked polystyrene divinylbenzene sulfonic acid when the first PEMFC was developed in the 1960's, however this was replaced in the 1980's by a perfluorinated sulfonic acid membrane that was of higher durability and ionic conductivity [2]. This consists of teflon-like fluorocarbon side-chains ending with sulfonic acid functional groups where the protons on the acid group are free to migrate throughout the membrane, completing the electrical circuit.

The requirements of a suitable membrane are that it should have high proton conductivity and be chemically and thermally stable [6]. It must be fully hydrated to ensure that the proton conductivity is sufficient, limiting the operation of the fuel cell to under 100 °C [4]. The thickness of the membrane is limited by the rate of crossover of reactants between the electrodes.

The PEMFC has become the likeliest replacement for the combustion engine for transportation due to its unique properties, which are summarised below:

- Low operating temperatures (60 to 90 °C)
- Comparable performance at higher efficiency [7] (PEMFC's have an efficiency of greater than 80 % compared to less than 40 % for a combustion engine)
- Rapid start-up from cold [6, 7]
- High power density with small space and weight requirements [2]
- Vastly reduced emissions of NO_x, CO, CO_2, and SO_x
- Noiseless
- Absence of corrosive liquid electrolyte
- Can withstand a pressure differential across the electrolyte unlike other fuel cell types [2]
- Many thousands of hours of operation with insignificant drop in performance
- Infinite life at open-circuit potential [6]

However, the release of commercially available PEMFC powered vehicles by the automotive manufacturers has been slowed due to a number of overriding considerations. Currently, the main obstruction is that of manufacturing costs. Many components would need to be produced more cheaply for the PEMFC to become economically viable. Flow field plates, for example, currently constructed from graphite, comprise 60 % of the cost of a fuel stack. In addition to this, there are problems due to high costs arising from the high platinum content in the

electrode catalysts. Work has been undertaken by several groups to reduce the platinum loading without compromising the performance of the fuel cell, by producing a larger active surface area [8, 9]. Another problem is that hydrogen, in addition to the dangers associated with storing it, is not yet economically available from renewable resources and therefore has to be reformed, usually from methanol or natural gas. This leads to the presence of approximately 1 % CO in the feed gas [4]. Due to the strong chemisorption of CO on platinum, ppm levels of CO in the fuel leads to 99 % of the anode catalyst being deactivated.

It is this interaction of CO with the platinum electrode that is investigated in this thesis. Various different solutions have been attempted. One idea was to promote the gas phase oxidation of CO by introducing a small amount of air into the anode chamber [10]. This method prevented the poisoning of the anode, but also significantly reduced the efficiency of the system. Another idea was to use hydrogen peroxide as an oxidising additive to chemically oxidise the CO [11]. This was only successful at high catalyst loadings (1 mg Pt/cm^2) that, if used, would lead to increased manufacturing costs due to the large amount of platinum required to make the anode. However, the most promising solution to CO poisoning is the use of a binary alloy as the anode. It had been shown that supported Pt/Ru 50:50 atomic percent electrodes are significantly more tolerant of CO in a hydrogen feed than supported Pt electrodes [12]. Nevertheless, this Pt/Ru electrode still only displayed tolerance to up to 30 ppm of CO in the feed at the low anode loadings (about 0.25 mg Pt/cm^2) considered to be commercially viable.

The direct methanol fuel cell (DMFC) is very similar in design to the PEMFC, shown in Figure 1.1, except it uses methanol as the feed instead of hydrogen. There are two commercial advantages arising from the DMFC's use of methanol as the fuel compared to the pure hydrogen used in the PEMFC. Firstly, there would be no need for a reforming step, which would lead to a smaller system for transportation purposes. Also, no hydrogen cylinders would be required, again reducing the amount of space the fuel cell tank would take up. The electrode reactions for the DMFC are shown in Equation 1.3 and 1.4.

Anode	$CH_3OH + H_2O \rightarrow CO_2 + 6H^+ + 6e^-$	Equation 1.3
Cathode	$\frac{3}{2} O_2 + 6H^+ + 6e^- \rightarrow 3H_2O$	Equation 1.4

The main problem with using platinum as the catalyst is that, when methanol is used directly, the oxidation process goes via a CO-like intermediate, which poisons the catalyst. In a similar way to the PEMFC, it has again been shown that the Pt/Ru system is favoured as a potential catalyst [13].

The improved tolerance of the Pt/Ru system towards CO poisoning over the pure platinum system is because the ruthenium acts as a promoter for the oxidation of CO [14]. It has been shown that the promotion occurs via the adsorption of an oxidising species, such as an OH radical, onto ruthenium. This oxidising species is then able to oxidise the CO that is bound to the platinum, thus slowing the rate of poisoning of the platinum.

This oxidative procedure occurs by a bi-functional mechanism [14], the role of which is two-fold. Firstly, there is thought to be an electronic effect in which the platinum sites in the Pt/Ru system are modified compared to pure platinum, such that carbon monoxide is less strongly adsorbed. Secondly, the ruthenium serves to make water activation easier, which leads to an increase in the amount of oxidising species on ruthenium atoms. This bi-functional mechanism is explained by the two steps shown below in Equations 1.5 and 1.6.

Step 1	$Pt\text{-}CO + Ru\text{-}OH \rightarrow Pt\text{-}COOH + Ru_{(s)}$	Equation 1.5
Step 2	$Pt\text{-}COOH \rightarrow Pt_{(s)} + CO_2 + H^+ + e^-$	Equation 1.6

In Equation 1.5, the CO bonded to the platinum atom is oxidised by the OH that is adsorbed on the ruthenium atom, leaving the ruthenium site empty and the COOH species bonded to the platinum atom. The COOH species then quickly reacts to form CO_2 and H^+, leaving the platinum site empty, as shown in Equation 1.6, and therefore still active as a site for H_2 or methanol oxidation.

Various vibrational studies on the chemisorption of CO on platinum single crystals have been carried out using HREELS (high resolution electron energy loss spectroscopy) [15-19], mid-infrared RAIRS [17, 20-23] and far-infrared techniques [24-29]. The synchrotron far-infrared RAIRS experiments presented in this thesis give additional information on the bonding of CO to the Pt(111) and Pt(110) surfaces. Part of this additional information arises from the fact that the Pt-CO vibration is highly sensitive to the substrate structure [30], for which far-infrared studies are necessary since these vibrations occur between 300 and 500 cm^{-1}. Also, HREELS experiments, because of the tail of the inelastic scattering peak, and mid-infrared experiments, due to the low brightness of "black-body" sources in the far-infrared, are too noisy in this region, making useful low wavenumber data very difficult to obtain. Another advantage of synchrotron far-infrared RAIRS is that the data accumulation time is considerably less, about one thousandth, than other far-infrared techniques [24-29]. This allows less time for background contaminants to adsorb on the surface and possibly affect the infrared experiment.

1.2 How the work in this thesis relates to fuel cell development

Given that the major problem in using platinum as a catalyst in either the PEMFC or DMFC is that poisoning from CO adsorption on the platinum electrode dramatically decreases the catalytic activity of the electrode [4], it is of great importance to gain a better understanding of how the CO species bonds to both the platinum and platinum/ruthenium surfaces.

One of the most powerful techniques to probe the bonding of a chemisorbed molecule is infrared spectroscopy. The vibrational frequencies of a molecule tell us how the atoms are bonded together and even the local environment of these bonds. It is this sensitivity of RAIRS to the local environment that is so important in its use to determine the nature of the bonding between the CO and the surface,

and hence derive information about the nature of the surface, as well as the adsorption sites occupied by the CO molecules.

The vibrations of bonds within adsorbate molecules are readily probed with infrared light emitted from a conventional "black body" source. However, the vibration directly associated with the substrate-adsorbate bond occurs at lower frequencies, where the output from thermal sources is drastically reduced. However, the synchrotron source is much brighter and is perfectly matched to the experimental requirement of grazing reflection. However, it is not sufficient for the source to be bright; it is also of great importance for it to be stable, and the SRS at Daresbury, where all the infrared spectra in this thesis were recorded, has a high beam stability, allowing the weakest low frequency spectral features to be detected.

The catalysts in both the PEMFC and DMFC consist of small particles of platinum on a carbon support. Since these particles are so small, it follows that their surface must consist of platinum atoms arranged into combinations of the simplest face centred cubic terminations – the (111) and (100) faces, as defined by Miller indices [31], which constitutes one reason why the Pt(111) and Pt(110) surfaces were studied. The other reason these particular surfaces were studied lies in the varied topography of the surfaces themselves. The Pt(111) surface has a hexagonal arrangement of platinum atoms, which leads to three distinctly different bonding sites for the CO molecule. The Pt(110) surface undergoes a "missing row" reconstruction when placed in ultra high vacuum (UHV) [32, 33]. This reconstruction is lifted when CO is adsorbed on the surface [32-36]. By studying the bonding of CO on these varied surfaces a range of information can be obtained.

All the surface analysis presented in this thesis was carried out in UHV. This provides an environment that is free from atmospheric contaminants, thus ensuring any information obtained regarding the bonding of CO to the platinum

surface is due only to the topography of the surface or other molecules that were specifically introduced.

Chapter four of this thesis discusses the bonding of CO to a clean Pt(111) single crystal, as investigated by far-infrared RAIRS of CO adsorbed in both atop and two-fold bridged sites. These studies combine to give a clear bonding model of CO on Pt(111) and show which adsorption sites are used by CO.

Chapter five presents a comprehensive study of the Pt-C stretching vibration as the reconstruction of the Pt(110) surface is lifted, and a set of complementary *ab initio* calculations of CO adsorbed in various sites on both substrate structures.

Chapter six discusses the adsorption of benzene and pyridine on the Pt(110) surface. The substrate-adsorbate bond for both adsorbate molecules is again probed by far-infrared RAIRS. Only in the case of benzene is the substrate-adsorbate stretching vibration detected, but both molecules show signs of adsorption given by a distinctive "derivative" style feature in the Pt-CO stretching vibration region.

Finally, chapter seven outlines the use of electrochemical transfer experiments as a means of both investigating the bonding of CO more fully via cyclic voltammetry, and a way of depositing a second metal, in this case ruthenium, onto the platinum surface from solution.

1.3 References

1. G. Hoogers, Phys. World 11 8 (1998) 31.
2. K. B. Prater, J. Power Sources 51 1-2 (1994) 129.
3. A. J. Appleby, Energy 21 7-8 (1996) 521.
4. R. A. Lemons, J. Power Sources 29 1-2 (1990) 251.
5. K. Strasser, J. Power Sources 37 1-2 (1992) 209.

6. O. J. Murphy, G. D. Hitchens, and D. J. Manko, J. Power Sources 47 3 (1994) 353.
7. G. A. Hards, Plat. Met. Rev. 37 (1993) 24.
8. T. R. Ralph, Plat. Met. Rev. 41 (1997) 102.
9. M. S. Wilson and S. Gottesfeld, J. Electrochem. Soc. 139 2 (1992) L28.
10. S. Gottesfeld and J. Pafford, J. Electrochem. Soc. 135 10 (1988) 2651.
11. V. M. Schmidt, H. F. Oetjen, and J. Divisek, J. Electrochem. Soc. 144 9 (1997) L237.
12. H. F. Oetjen, V. M. Schmidt, U. Stimming, and F. Trila, J. Electrochem. Soc. 143 12 (1996) 3838.
13. S. Surampudi, S. R. Narayanan, E. Vamos, H. Frank, G. Halpert, A. Laconti, J. Kosek, G. K. S. Prakash, and G. A. Olah, J. Power Sources 47 3 (1994) 377.
14. M. Watanabe and S. Motoo, J. Electroanal. Chem. 60 (1975) 267.
15. H. Froitzheim, H. Hopster, H. Ibach, and S. Lehwald, Appl. Phys. 13 (1977) 147.
16. H. Steininger, S. Lehwald, and H. Ibach, Surf. Sci. 123 2-3 (1982) 264.
17. S. R. Bare, P. Hofmann, and D. A. King, Surf. Sci. 144 2-3 (1984) 347.
18. C. Klunker, M. Balden, S. Lehwald, and W. Daum, Surf. Sci. 360 1-3 (1996) 104.
19. P. Hofmann, S. R. Bare, and D. A. King, Phys. Scr. T4 (1983) 118.
20. R. A. Shigeishi and D. A. King, Surf. Sci. 58 (1976) 379.
21. F. M. Hoffmann and A. M. Bradshaw, J. Catal. 44 (1976) 328.
22. B. E. Hayden, A. W. Robinson, and P. M. Tucker, Surf. Sci. 192 1 (1987) 163.
23. R. K. Sharma, W. A. Brown, and D. A. King, Surf. Sci. 414 1-2 (1998) 68.
24. R. G. Tobin and P. L. Richards, Surf. Sci. 179 2-3 (1987) 387.
25. F. H. Scholes, A. Locatelli, H. Kleine, V. P. Ostanin, and D. A. King, Surf. Sci. 502 (2002) 249.
26. I. J. Malik and M. Trenary, Surf. Sci. 214 1-2 (1989) L237.
27. U. Engstrom and R. Ryberg, Phys. Rev. Lett. 78 10 (1997) 1944.
28. U. Engstrom and R. Ryberg, J. Chem. Phys. 115 1 (2001) 519.

29. D. Hoge, M. Tushaus, E. Schweizer, and A. M. Bradshaw, Chem. Phys. Lett. 151 3 (1988) 230.
30. M. Surman, P. L. Hagans, N. E. Wilson, C. J. Baily, and A. E. Russell, Surf. Sci. 511 1-3 (2002) L303.
31. P. W. Atkins, Physical Chemistry, Fifth Edition, Oxford University Press, Oxford, (1994).
32. P. Fenter and T. Gustafsson, Phys. Rev. B 38 15 (1988) 10197.
33. P. Fery, W. Moritz, and D. Wolf, Phys. Rev. B 38 11 (1988) 7275.
34. C. M. Comrie and R. M. Lambert, J. Chem. Soc., Faraday Trans. 72 (1976) 1659.
35. T. E. Jackman, J. A. Davies, D. P. Jackson, W. N. Unertl, and P. R. Norton, Surf. Sci. 120 2 (1982) 389.
36. S. Ferrer and H. P. Bonzel, Surf. Sci. 119 2-3 (1982) 234.

Chapter Two – Experimental Methods

2.1 Ultra High Vacuum (UHV) Techniques

The pressure region known as UHV is defined as any pressure below about 10^{-7} mbar [1]. In order to obtain a UHV experimental environment, all experiments are carried out in an argon-welded stainless steel chamber which is being continuously pumped by a combination of diffusion, turbo and rotary pumps. The chamber is designed so that it can be heated to a temperature of about 150 °C, a process known as baking, by the use of several bakeout heaters. Baking is a standard UHV process, used prior to performing any experiments, which enables the pressure in the chamber to be as low as possible. Baking the chamber accelerates the desorption of water vapour and other gases from the chamber walls, and so allows more gas molecules to be pumped away [2]. In general, the chamber is baked for 48 hours and, on cooling back down to room temperature, the base pressure in the chamber will change from approximately 10^{-8} mbar before the bakeout to about 10^{-10} mbar after the bakeout.

2.1.1 Dosing Set-up

Gases and liquids were attached to a single gas line on the chamber, and were dosed through a leak valve. Gas samples were opened to a small amount of gas line using Nupro valves to hold the pressure, and then expanded up to the leak valve. Liquids, such as benzene and pyridine, were placed in a glass sample tube which was attached to the gas line via a KF to mini flange adaptor. The liquids were purified by repeated freeze-pump-thaw cycles. Each of the substances was dosed by back-filling the chamber. All exposures are reported in Langmuir (L), where 1 L = 10^{-6} Torr s.

2.1.2 Sample Manipulation and Mounting

The platinum (111) and platinum (110) crystals were mounted on a manipulator which allowed movement in the x, y and z directions and full rotation around the z-axis. The manipulator was constructed so that the sample could be cooled by pouring liquid nitrogen into a hollow stainless steel reservoir at the top of the manipulator arm, which was in thermal contact with the sample.

Each crystal was mounted by being spot-welded to two tungsten wires, which were held onto the sample mount, also called a stub, by being wound around four small screws. The stub was designed so that the electrical connections for the heating and thermocouple were made via insulated metal rings on the back of the stub, which in turn were connected to the external feedthroughs via a set of springs on the back of the manipulator arm. The sample mounting is illustrated in Figure 2.1.

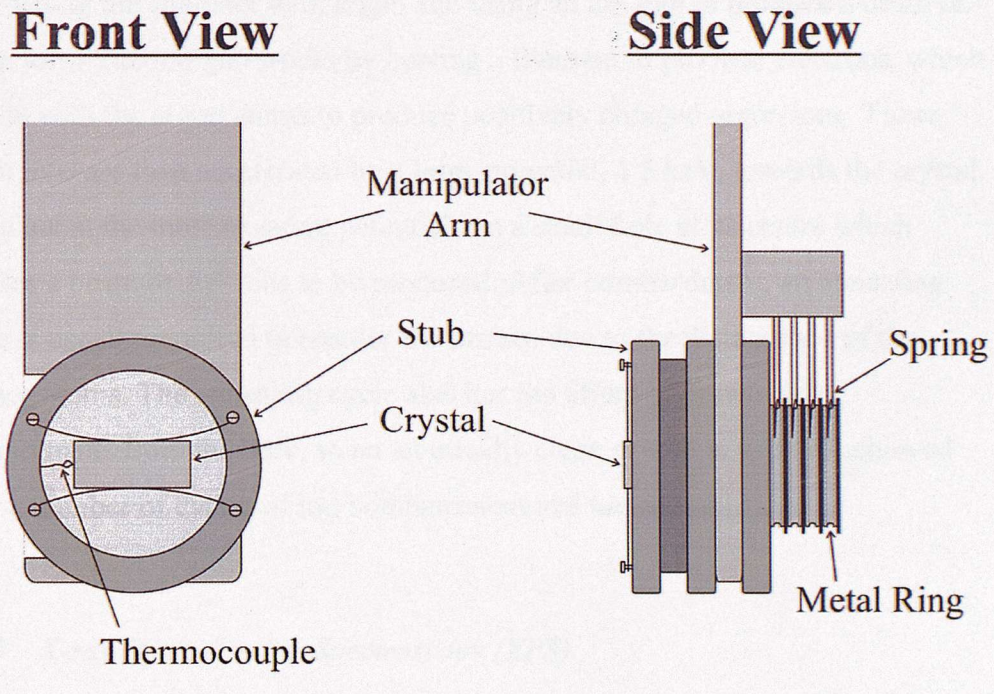

Figure 2.1 – Schematic diagram of the sample mounting

2.1.3 *Sample Cleaning*

Cleaning of both the platinum crystals was achieved by oxygen treatment, followed by ion bombardment and annealing *in vacuo*. The platinum crystals were cleaned by cycles of sputtering with argon, 3 x 10^{-5} mbar for 20 minutes with a beam energy of 1.5 keV and typical drain current of 7 μA, and annealing at 1225 K. The crystal was occasionally heated in an atmosphere of oxygen, 1 x 10^{-7} mbar for 20 minutes at 950 K. XPS (X-ray Photoelectron Spectroscopy) spectra were taken to confirm the cleanliness of the samples.

2.1.4 *Ion Bombardment*

By far the most common contaminant of platinum single crystals is carbon. The most effective method of removing this carbon is ion bombardment of the surface with noble gas ions e.g. Ar^+ or Ne^+. Ion bombardment is carried out by back-filling the chamber with argon and using an ion gun to produce a beam of argon ions. The ion gun works by heating a filament to produce electrons, which collide with the argon atoms to produce positively charged argon ions. These argon ions are then accelerated by a large potential, 1.5 keV, towards the crystal. The plate at the most negative potential has a small hole at its centre which enables a beam of Ar^+ ions to be produced. After bombardment, an annealing cycle is usually required to reorder the surface due to the disturbance of the surface atoms. The annealing cycle also has the effect of drawing out contaminants from the bulk, so an atomically clean crystal is usually achieved after a number of cycles of ion bombardment and annealing [3].

2.1.5 *X-ray Photoelectron Spectroscopy (XPS)*

XPS provides information about elemental surface composition [4]. The surface to be analysed is first placed in a vacuum environment and then irradiated with photons. For XPS, the photon source is in the X-ray energy range, typically

from an anode of magnesium or aluminium [5]. The atoms that make up the surface emit electrons, called photoelectrons, after direct transfer of energy from the photon to the core level electron. An energy analyser is then used to separate, according to energy, and count these emitted electrons. The energy of the photoelectrons is directly related to the atomic and molecular environment from which they originated and the number of photoelectrons emitted is related to the concentration of the emitting atoms in the sample [6]. The photoemission process is shown in Figure 2.2.

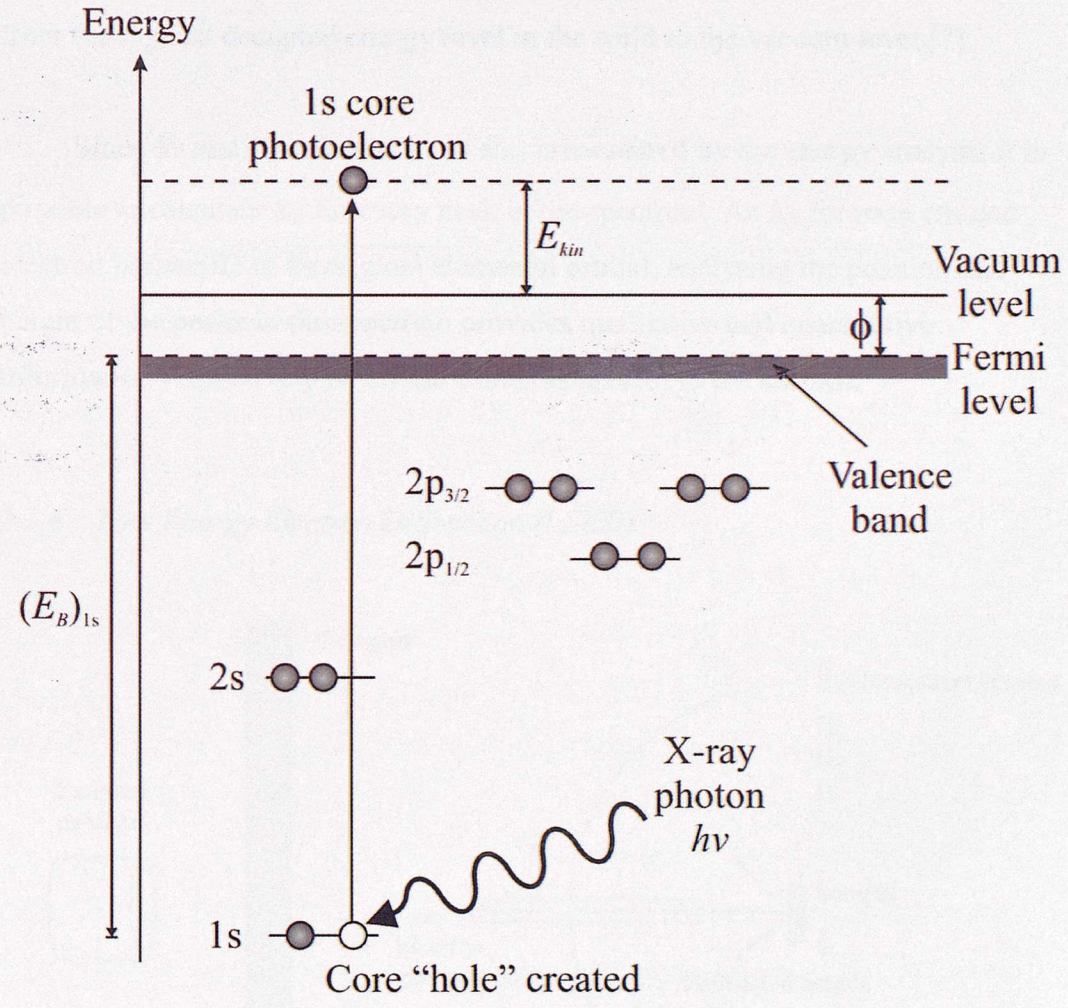

Figure 2.2 – X-ray photoemission of a 1s core level electron

Applying the principle of conservation of energy, the emitted photoelectrons have a kinetic energy, E_{kin}, equal to

$$E_{kin} = h\nu - E_B - \phi \qquad \textbf{2.1}$$

where $h\nu$ is the energy of the incident X-rays, E_B is the binding energy of the ejected electron and ϕ is the workfunction. The binding energy is defined as the energy of the core level of the emitted electron relative to the Fermi level, and the workfunction is defined as the minimum energy required to remove an electron from the highest occupied energy level in the solid to the vacuum level [7].

Since $h\nu$ and ϕ are known, and E_{kin} is measured by the energy analyser it is possible to calculate E_B for every peak in the spectrum. As E_B for each emitted electron is specific to its original elemental orbital, analysing the position and height of the peaks in the spectrum provides qualitative and quantitative information respectively on all the elements present in the surface.

2.1.6 Low Energy Electron Diffraction (LEED)

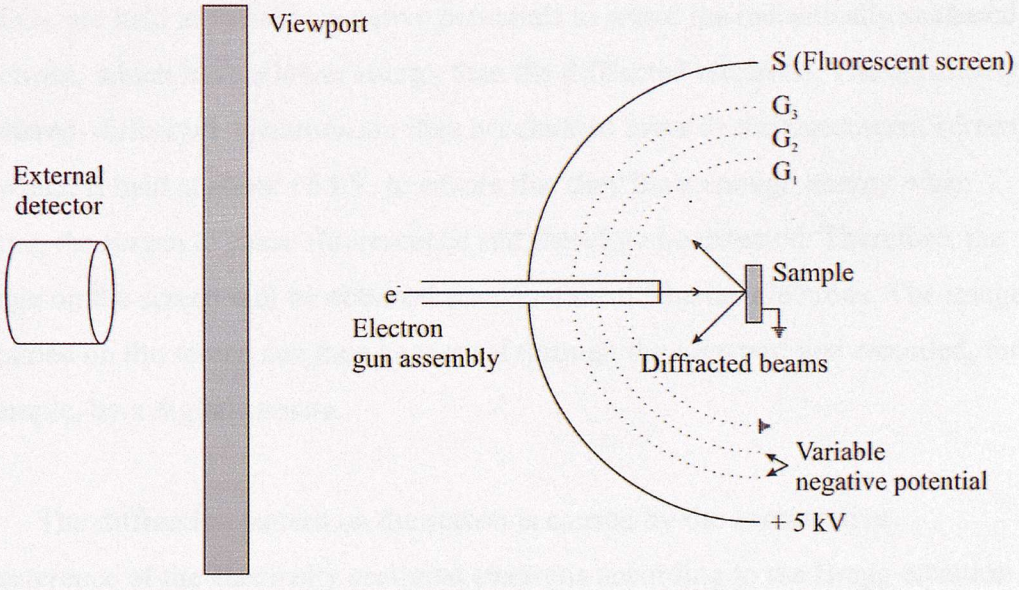

Figure 2.3 Diagram of the LEED optics used in the UHV chamber

Figure 2.3 shows a diagram of the reverse-view LEED optics used in the UHV chamber.

The LEED experiment works by firing a beam of electrons with incident energy from 30 to 300 eV at the sample. These low energy electrons have wavelengths of the order of 1 Å, as given by the de Broglie relationship [8]:

$$\lambda = \frac{h}{mv} = \sqrt{\frac{150}{E}} \qquad \textbf{2.2}$$

Where m is the mass of an electron, h is Planck's constant, v is the velocity of the electron, λ is the electron wavelength (in Å) and E is the energy of the electron (in eV). Since these electron wavelengths are comparable to the spacing between atoms comprising the crystal surface, the electrons are able to diffract (elastically backscatter) from the surface atoms onto the system of grids. This system of grids is used to minimise the diffuse background resulting from inelastically scattered electrons, which make up 99 % of the total scattered electrons. The first grid, G_1 is held at the same potential as the sample (earth) to provide a field-free region for the electrons to move within, enabling the electrons that are emitted from the sample to travel in a straight line. The next two grids, G_2 and G_3, are held at variable negative potentials to retard the inelastically scattered electrons, which have a lower energy than the diffracted electrons. The elastically scattered, diffracted, electrons are then accelerated towards the fluorescent screen, S, which is held at about +5 kV, to ensure that they have enough energy when hitting the screen to cause fluorescence and therefore be detected. Therefore, the image on the screen will be obtained from just the diffracted electrons. The image obtained on the screen can then be viewed through the viewport and recorded, for example, by a digital camera.

The diffraction pattern on the screen is caused by the constructive interference of the elastically scattered electrons according to the Bragg equation (Equation 2.3) as shown in Figure 2.4.

$$n\lambda = a \sin\theta \qquad \textbf{2.3}$$

Where, n = the order of diffraction, an integer

λ = electron wavelength / Å

a = interatomic distance / Å

θ = angle from incident

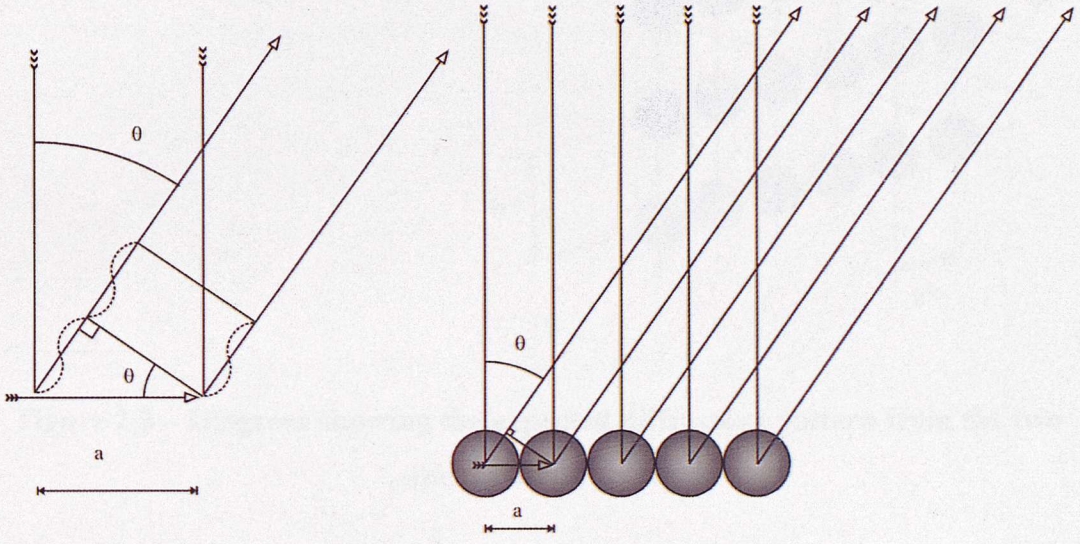

Figure 2.4 – Constructive interference from diffracted electrons from a one dimensional periodic array

When this theory is applied to a two dimensional surface, it is possible to obtain a diffraction pattern in two dimensions on the screen. This is shown in Figure 2.5.

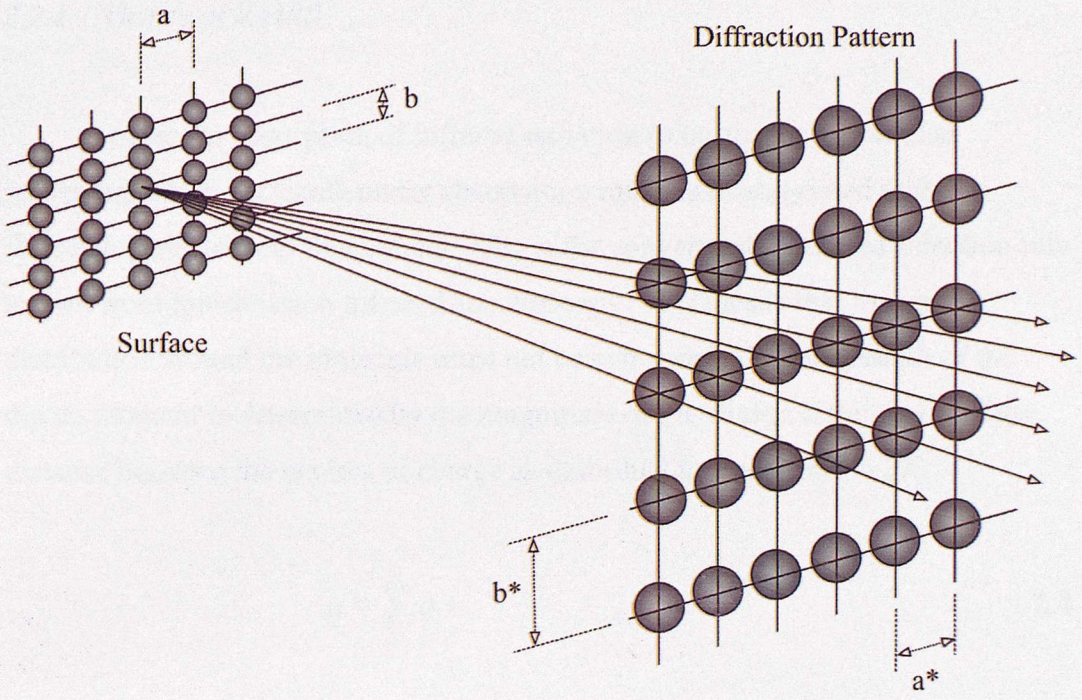

Figure 2.5 – Diagram showing the expected diffraction pattern from the two dimensional surface

Figure 2.5 shows that the diffraction pattern is directly related to the structure of the surface. Therefore, by studying the diffraction pattern, it is possible to gain information about the surface itself. For example, the symmetry of the surface is always the same as the symmetry of the diffraction pattern. Also, longer distances on the surface give shorter distances in the diffraction pattern. This enables the orientation of rectangular lattices to be recognised. If molecules or atoms adsorb on the surface, they will often form ordered structures themselves on the surface. The ordered layer will give rise to diffraction and an additional set of diffraction spots will be seen on the LEED screen.

2.2 Reflection Absorption Infrared Spectroscopy (RAIRS)

RAIRS is used in surface analysis to provide information about the structure and bonding of adsorbed species by the absorption of infrared radiation.

2.2.1 *Theory of RAIRS*

In order for absorption of infrared radiation to occur, the vibrational movement of the molecule under observation must have associated with it a fluctuating electric dipole moment. This is the conventional infrared selection rule known from transmission infrared spectroscopy. This means that the charge distribution around the molecule must not be symmetrical. The strength of the dipole moment is determined by the magnitude of the charge difference and the distance between the centres of charge as described in Equation 2.4 [9].

$$\underline{\mu} = \sum_{i=1}^{N} q_i \underline{r_i} \qquad \textbf{2.4}$$

Where, $\underline{\mu}$ = electric dipole moment vector

N = number of atoms in the molecule

q_i = electric charge on atom i

$\underline{r_i}$ = direction vector of atom i from a fixed point (e.g. centre of mass of the molecule)

As the molecule bends and stretches, the changing dipole moment establishes an electric field around the molecule. When the alternating electric field of the infrared radiation matches in frequency one of the natural oscillatory frequencies of the molecule, interaction between the two fields may occur, resulting in resonant energy transfer and a change in amplitude of the motion. It is this change in amplitude of the motion which is detected, giving information about the strength of the excited bonds.

Unfortunately, the electric field of the infrared radiation will also interact with the valence metal electrons at the surface [10]. This results in the excitation of both the electric dipole of the molecule and its image in the surface. This effect makes the vector sum of the fields of the electric dipole and its image of great importance.

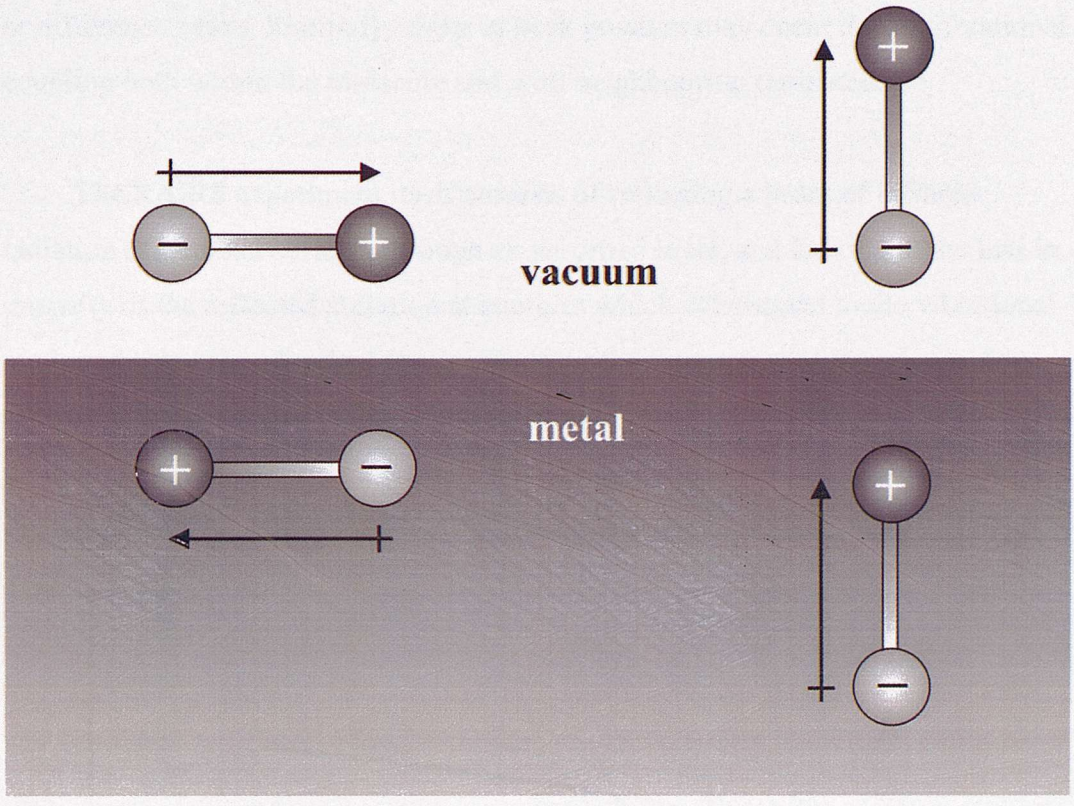

Figure 2.6 – The screening effect of a metal surface to a parallel dipole, and the enhancement of a metal surface to a perpendicular dipole

Figure 2.6 shows that if the dipole of the molecule is perpendicular to the surface, the dipole field will be enhanced by the incident electric field associated with the infrared radiation. In contrast, for a dipole which is parallel to the surface, the net result is a quadrupole, which leaves no dipole moment to interact with the electric field. This means that only vibrational modes with a component of their dipole change perpendicular to the surface can be observed by this technique.

The quantisation of vibrational and rotational movements in molecules results in discrete energy absorption. The number and position of absorption peaks in the spectra are affected by many influencing factors. Molecular symmetries, degenerate energy levels, low absorption coefficients and absorption peaks which lie out of the range of the detector can all contribute to "missing peaks".

Conversely, extra peaks can occur due to overtones, as well as from combination or difference peaks. Similarly, shifts in peak position may occur due to vibrational coupling both within the molecule and with neighbouring molecules.

The RAIRS experiment itself consists of reflecting a beam of infrared radiation off a metal surface, through an adsorbed layer, and looking at the loss in intensity of the reflected radiation at energies which correspond to the vibrational modes of either the adsorbed species itself, or the interaction of the adsorbed species with the surface atoms of the substrate.

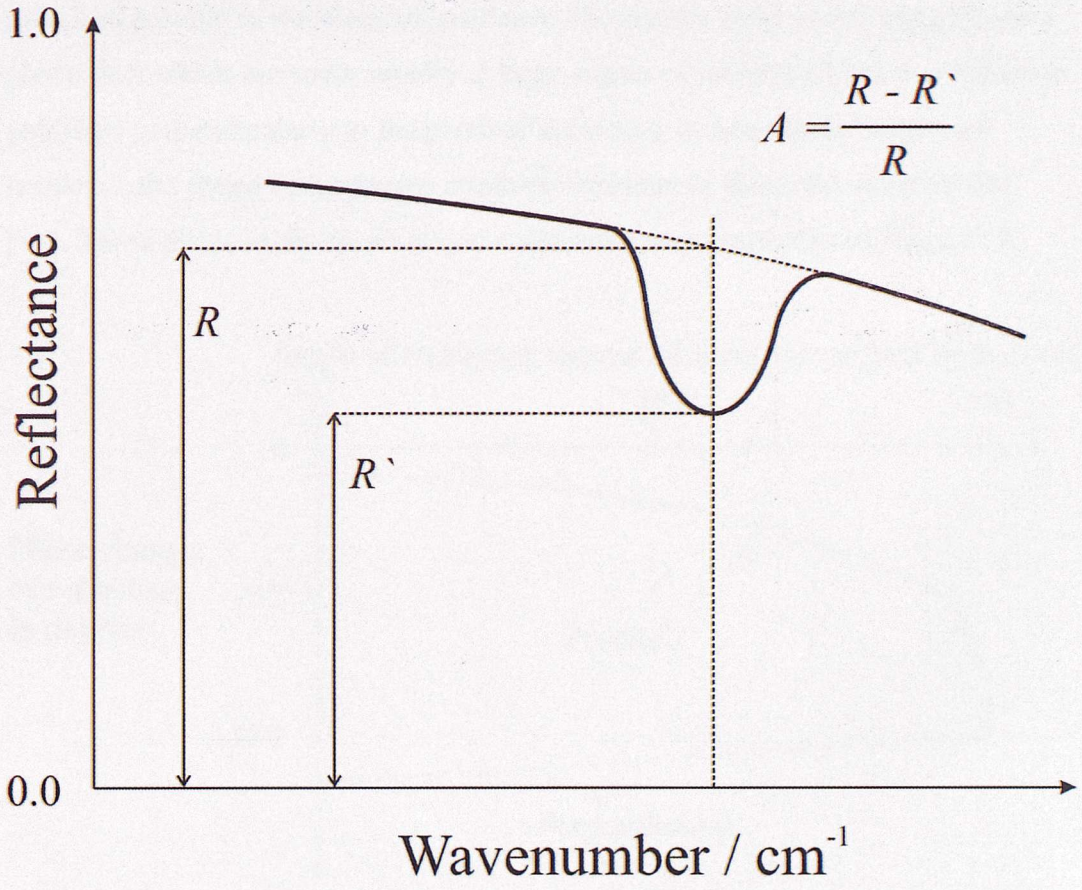

Figure 2.7 – The definition of the Absorption Factor, *A*, where *R'* is the reflectance of the modelled adsorbate, and *R-R'* is the reflectance in a three-phase system with a non-absorbing adsorbate

Until the physical parts of the RAIRS technique were fully understood, the method suffered from very poor absorption factors (see Figure 2.7) [11-13], which made obtaining satisfactory spectra impossible. At near normal incidence, the incident and reflected infrared waves combine to give a standing wave with a nodal point at the surface. The electric field vectors cancel out at this point and cannot interact with the fluctuating dipole moments of the adsorbed molecules. This makes up the most important selection rule in RAIRS: only radiation polarised parallel to the plane of incidence will have a sizeable component of its electric field normal to the surface. This links in with the point made earlier about it being necessary for molecules to have a component of their fluctuating dipole moment perpendicular to the surface in order to be observed. For radiation polarised parallel to the plane of incidence, the electric field vector experiences a phase shift which increases rapidly at large angles of incidence [11]. For radiation polarised perpendicularly to the plane of incidence, at non-normal angles of incidence the phase shift remains relatively constant at about the value of 180° [11]. These phase shifts are shown in a schematic representation in Figure 2.8.

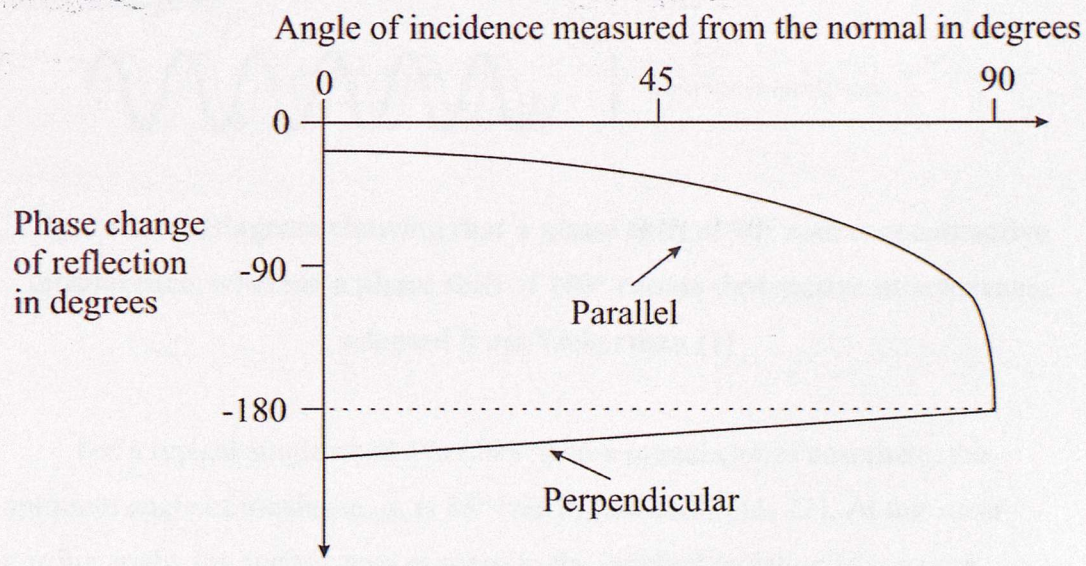

Figure 2.8 – The phase shift for light reflected from a metal surface as calculated for light polarised both parallel to (p) and perpendicular to (s) the plane of incidence, adapted from Greenler [11].

When the phase shift between the incoming and reflected wave is 90° the superposition of their respective electric field vectors normal to the surface is a maximum (see Figure 2.9). From Figure 2.8 it can be seen that a phase shift of 90° occurs at an angle of incidence, φ, of about 80°, so to obtain the best possible band intensity, this angle of incidence should be used.

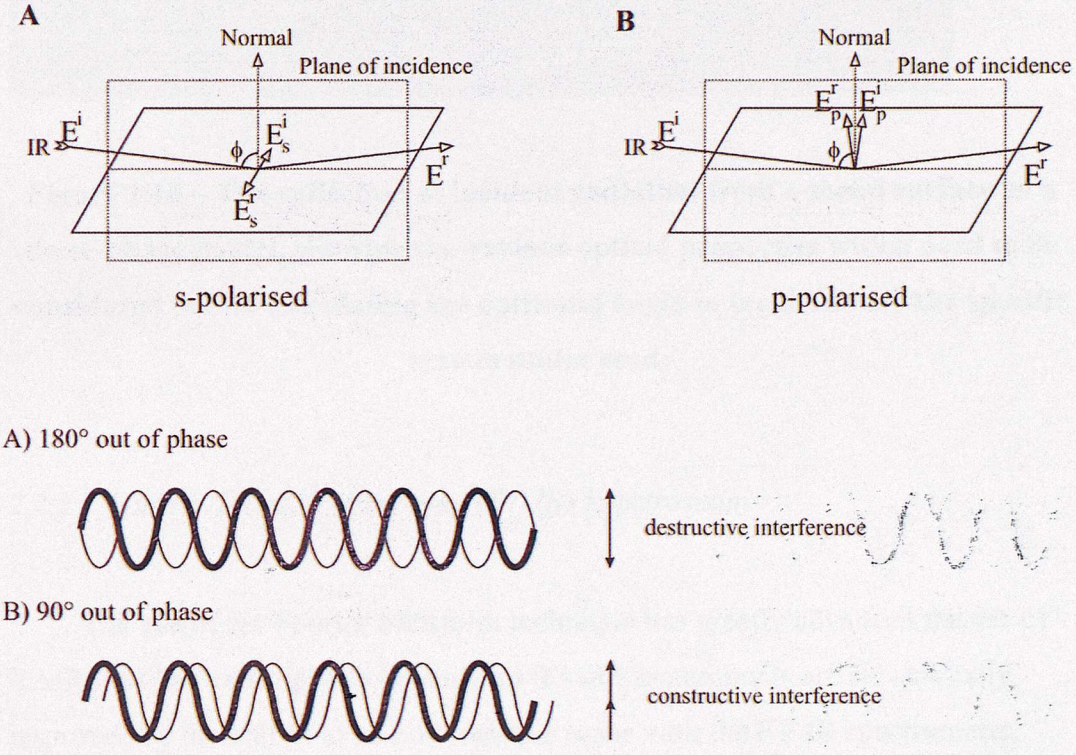

Figure 2.9 – Diagram showing that a phase shift of 90° causes constructive interference, whereas a phase shift of 180° causes destructive interference, adapted from Vickerman [1]

For a typical single crystal in UHV with a monolayer of adsorbate, the optimum angle of incidence, φ, is 88° (see Figure 2.10) [11, 12]. At this, near grazing angle, the surface area exposed to the incident radiation is at a near maximum. In practice, however, an angle of 80° is often used as a compromise between the theoretical optimum of 88° and the fact that at this angle the irradiated surface area is often much larger than the actual sample area.

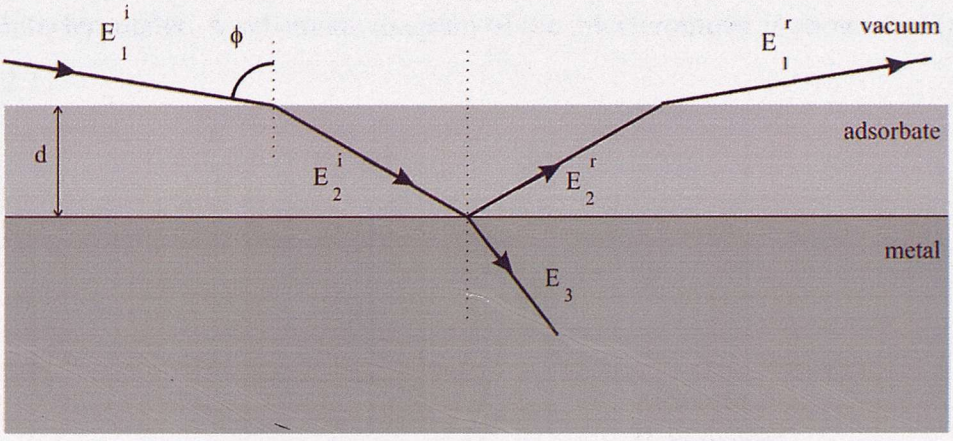

Figure 2.10 – The reflection of incident radiation from a metal surface as a three-phase model, showing the various optical properties which need to be considered before calculating the optimum angle in incidence for the specific system under study

2.2.2 Fourier Transform Infrared (FT-IR) Spectroscopy

The use of the Fourier transform technique has greatly advanced the use of RAIRS, as the weak spectra obtained in RAIRS experiments are substantially improved by the ability to co-add multiple scans with the FT-IR spectrometer, which improves the signal-to-noise ratio. The theory of FT-IR has been discussed by several authors [14-16] and is based on the mathematical treatment of the physical phenomenon of interferometry, and the use of Fourier transformation to obtain spectral information. A brief outline of these ideas is given below.

The application of FT in infrared spectroscopy originates from the development of the Michelson interferometer [17, 18] and the realisation by Rayleigh that the interpretation of the interferogram required the use of the Fourier transform [19].

The central component of a Fourier transform infrared spectrometer is a two beam interferometer. In modern machines, this is generally a Michelson

interferometer. A schematic diagram of the interferometer is shown in Figure 2.11.

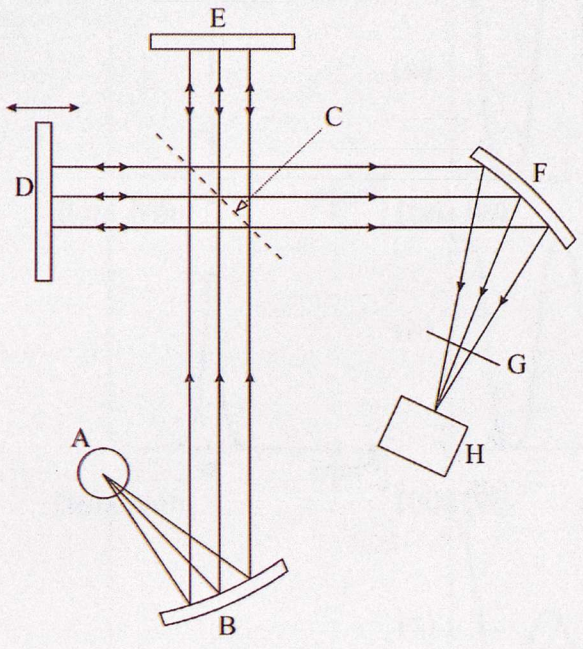

Figure 2.11 – A schematic of the Michelson interferometer optical system, adapted from Bell [15]

Light enters the system from an infrared source and this is then directed onto a beamsplitter. At the beamsplitter the radiation is then split in half, with half transmitted to a fixed mirror and the other half reflected to a moving mirror. These two mirrors are orientated perpendicular to one another, and when the beams recombine they create an interferogram which is due to the difference in the path length of the light introduced by the moving mirror. A Fourier transform of the signal reaching the detector is performed, and when plotted against wavenumber a graph of intensity versus wavenumber is produced, see Figure 2.12. The ratio of these intensity graphs is used to produce the infrared spectrum.

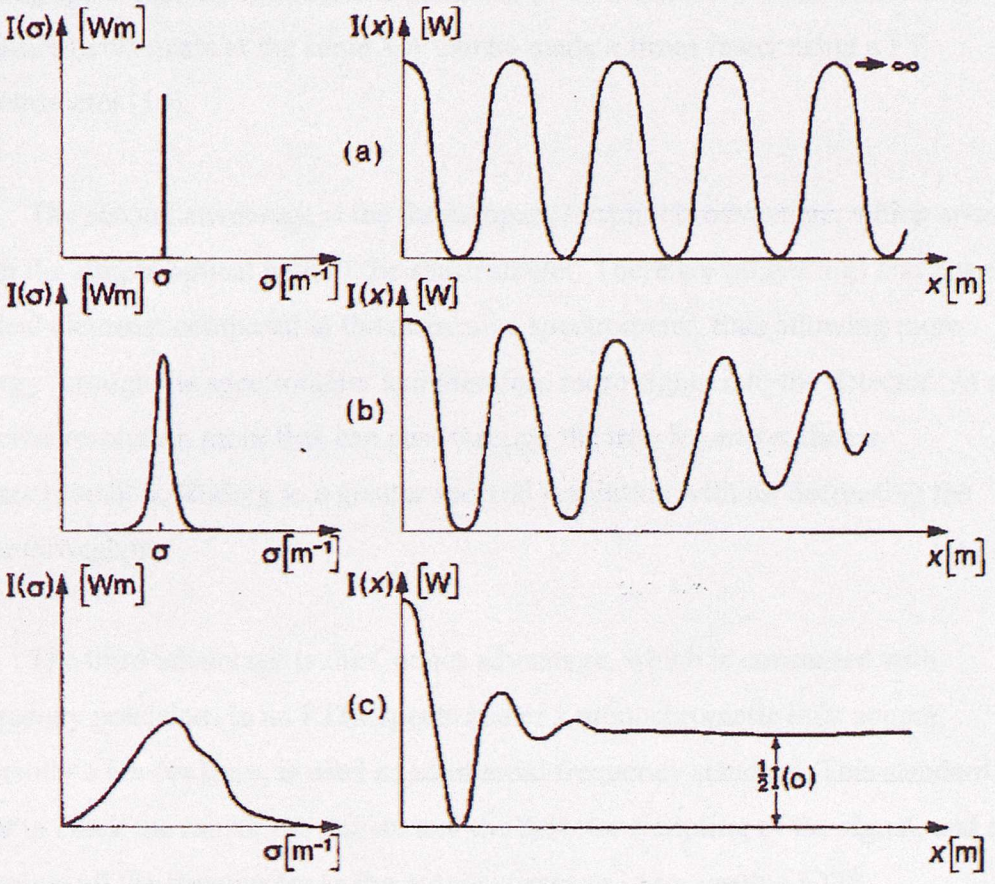

Figure 2.12 – Relation between the detected spectrum $I(\sigma)$ and the interferogram signal $I(x)$ produced by it: (a) monochromatic spectrum; (b) quasi-monochromatic spectrum; (c) broad-band spectrum, from Chamberlain [16]

There are three advantages of FT instruments over dispersive instruments. The main advantage is the multiplex (Fellgett) advantage. This is where all the light from the source can be detected by the detector at any instant, compared to a dispersive instrument where only one wavelength is detected at any given time. Each point on the interferogram contains information from each wavelength present in the input light signal. The Fellgett advantage also relates to the throughput of the signal. For measurements taken at equal resolution, over the same spectral range and in the same time, the signal-to-noise ratio, *S:N*, of the FT spectrometer will be $\sqrt{n}$ times greater than the *S:N* of spectra measured using the

grating spectrometer, where n is the number of resolution elements. Therefore, measurements made at the same $S:N$ can be made n times faster using a FT spectrometer [14].

The second advantage is the throughput (Jacquinot) advantage, which arises from the simple optical path of the spectrometer. There are no gratings and fewer optical elements compared to the dispersive spectrometer, thus allowing more energy through the spectrometer and therefore more signal into the detector. At a specific resolution more flux can pass through the interferometer than a monochromator, leading to a greater spectral resolution without decreasing the light throughput.

The third advantage is the Connes advantage, which is concerned with frequency precision. In an FTIR spectrometer a monochromatic light source, generally a He-Ne laser, is used as an internal frequency standard. This standard is used to clock the mirror movement and the detector sampling of the signal, and to calculate all the frequencies in the output spectrum. As a result a FTIR spectrometer easily achieves frequency precision and accuracy of better than 0.01 cm^{-1}.

2.3 UHV RAIRS at Daresbury SRS

The UHV RAIRS data presented in this thesis were obtained on beamline 13.3 at the SRS at Daresbury, UK. The UHV chamber was setup in a similar style to other surface science UHV chambers, with the only change being that synchrotron radiation was used as the infrared source instead of a glowbar, as is usual in infrared spectroscopy.

2.3.1 Synchrotron Radiation

At nonrelativistic velocities, electrons in circular motion radiate in a cosine distribution, see Figure 2.13, Case I. However, at relativistic velocities the distribution of the synchrotron radiation changes to become sharply peaked in the direction of the motion of the electrons, as in Figure 2.13, Case II.

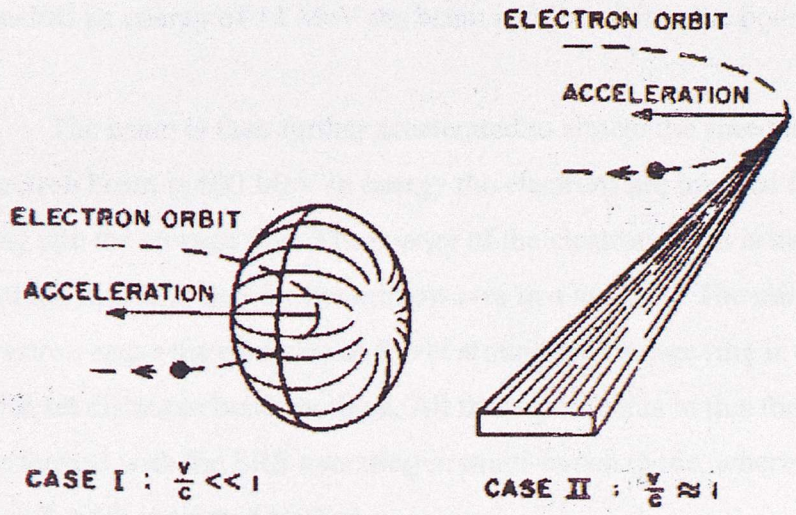

Figure 2.13 – Radiation emission pattern of electrons in circular motion, adapted from Winick and Doniach [20]

Synchrotron radiation is highly collimated, 100 % plane polarised in the orbit plane and it has a continuous energy distribution from the infrared to the hard X-ray part of the electromagnetic spectrum. Over the electromagnetic spectrum, synchrotron radiation has a brightness of typically 1000 times higher than a conventional black body source. This increased intensity enables experiments that were previously time or brightness limited to be carried out, making it a useful source for many new types of experiment across the electromagnetic spectrum.

2.3.2 *The SRS at Daresbury*

As with most storage ring facilities, the SRS at Daresbury consists of a LINAC (linear accelerator), a booster ring and finally a storage ring. The LINAC produces an electron beam which is accelerated to half the speed of light by a device called a klystron. A klystron works by producing microwaves which interact with the electrons and propel them along by giving them an energy boost, in a similar style to that of a surfer on a wave. When the LINAC beam has reached an energy of 12 MeV the beam is injected into the booster ring.

The beam is then further accelerated to almost the speed of light. When the electron beam is 600 MeV in energy the electrons are injected from the booster ring into the storage ring. The energy of the electron beam is increased in the storage ring to 2 GeV by the microwaves in a klystron. The microwaves from the klystron cause the electrons to travel around the storage ring in a series of bunches with set distances between them. All the experiments in this thesis were performed with the SRS operating in multi-bunch mode, where 160 bunches are stored, each separated by 2 ns.

The storage ring is kept under ultra high vacuum, typically 10^{-10} mbar, but the energy of the electrons is removed by collisions with gas molecules and so the beam current decays. At the time of writing this thesis, the beam at the SRS at Daresbury is typically refilled every 12 hours, during which the current decays from an initial value of approximately 250 mA down to approximately 140 mA.

2.3.3 *Far-IR spectroscopy using a Synchrotron Source*

In this thesis we are only concerned with the far-infrared region of the electromagnetic spectrum, which is defined as the region below 700 cm^{-1}. Calculations performed in the 1970's indicated that it is possible to use synchrotron radiation as a source of far-infrared light [21-23] as well as X-rays.

The ideas that resulted from these calculations were then put into practice by building IR ports at existing synchrotron sources. A set of characterising studies carried out by Yarwood *et al.* [24, 25], at the IR port at Daresbury in the mid 1980's, confirmed the results of the earlier calculations by showing that the radiation produced by the SRS would extend into the far-IR with a large flux.

The large flux of the synchrotron enables it to overcome the "energy limit" problem, in which good signal-to-noise ratios are difficult to achieve, in the far infrared region. Therefore, by using the synchrotron as a source of far-infrared radiation, the signal-to-noise ratio is improved and the data acquisition time is reduced.

As well as being significantly brighter than a laboratory source, the radiation from the synchrotron is also highly focussed and collimated. Combining these two properties with the increased brightness allows small samples to be studied (due to the high focussing) and the resolution to be high (due to the collimation of the radiation). This makes synchrotron radiation a useful source for studying far-infrared RAIRS of adsorbates on single crystal metal surfaces, where there are the requirements of small image size (because of using grazing incidence angles) and low beam divergence, the product of which is known as the étendue.

The RAIRS technique itself combines both high sensitivity (it is able to detect about 0.01 monolayer of a strong absorber) and high resolution (typically 1 cm^{-1}), which is not generally available from the alternative electron energy loss (EELS) technique, to become a powerful technique for studying vibrational spectra of adsorbed species.

2.3.4 Experimental setup of the far-IR beamline 13.3 at Daresbury

The infrared radiation required for the far-IR experiments on 13.3 is taken from the beam by placing a plane mirror (M1) as near as possible to the point of exit of the beam from the storage ring. Because of the large divergence of the

infrared beam, the M1 mirror must be placed very close to the ring in order to collect as much radiation whilst keeping the size of the mirror to a minimum. Mirror M1 deflects the beam vertically through the concrete shielding to the next mirror (M2, ellipsoidal), which deflects the beam horizontally. The arrangement of mirrors M1 and M2 are shown in Figure 2.14.

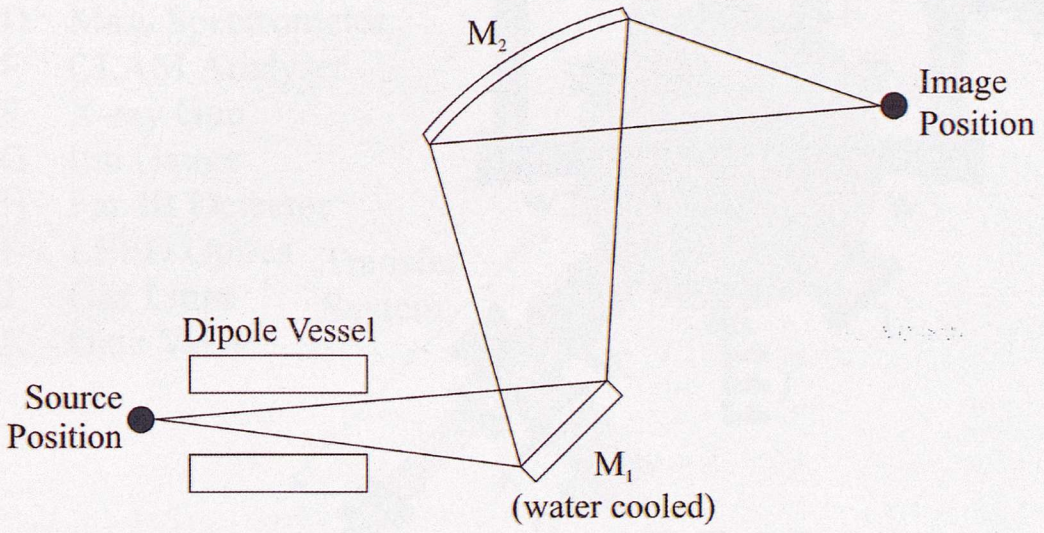

Figure 2.14 – The initial beam transport from the storage ring to the end station [26]

The system at 13.3, from mirror M2 onwards, is shown in Figure 2.15. The chamber is equipped with a quadrupole mass spectrometer (QMS), an ion gun, low energy electron diffraction (LEED), X-ray photoelectron spectroscopy (XPS), an electrochemical transfer system, and reflection absorption infrared spectroscopy (RAIRS).

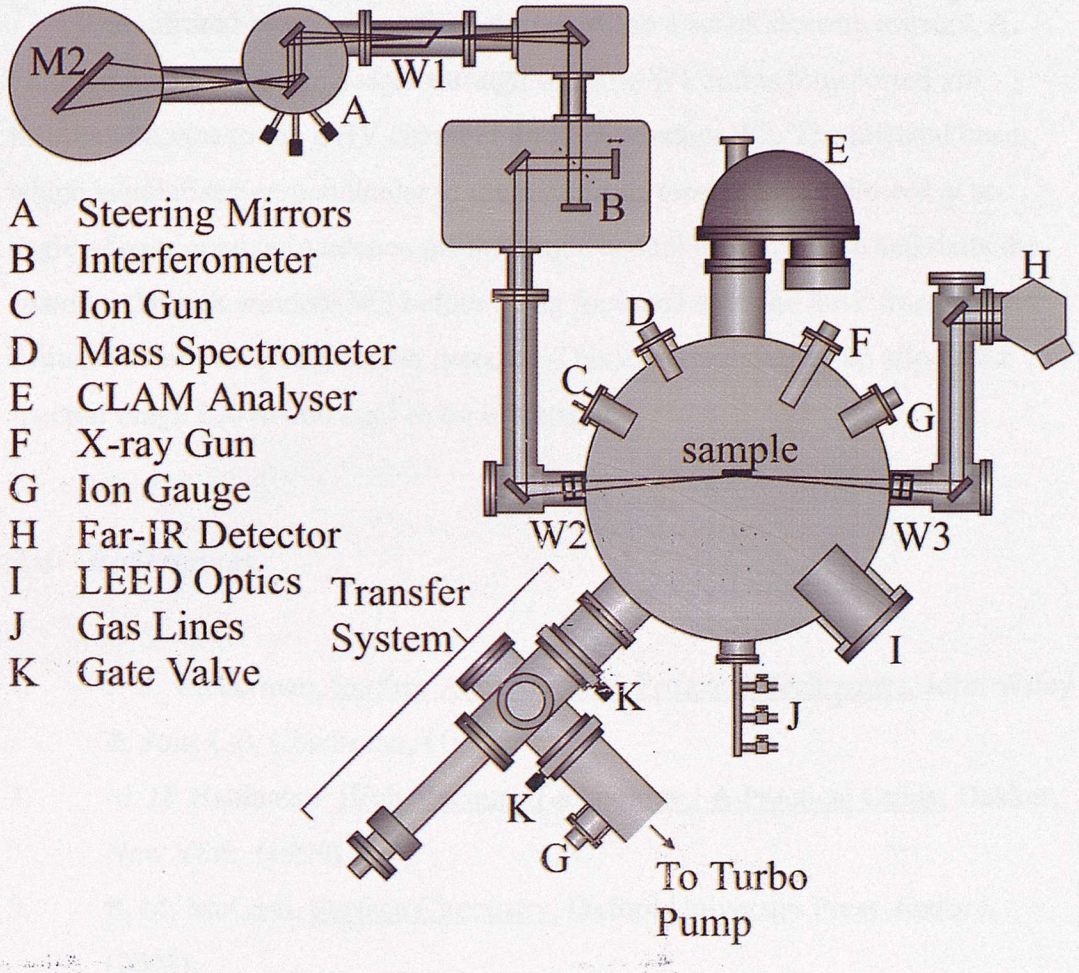

Figure 2.15 – Top view of the experimental set-up of station 13.3 at the SRS at Daresbury

The experimental set-up of the system at 13.3 is shown in Figure 2.15. W1 (window one) is made of CVD diamond, is wedged in shape, and is set at the Brewster angle to avoid reflection losses due to its high refractive index. This window is made from CVD diamond because it is free of absorption bands in the far-infrared region of the spectrum, 20 to 1000 cm^{-1}. Diamond is also chosen as it is a UHV compatible material, which is important since window one isolates the storage ring from the experimental area. Windows W2 and W3 isolate the UHV chamber from the rough vacuum of the beam transport manifolds, and are Brewster angle CsI (200 to 4000 cm^{-1}) windows, although CVD diamond windows are also available.

The infrared beam passes from mirror M2 to a set of steering mirrors, A. Following this, the beam passes through window W1 and is transported via additional optics to the UHV chamber through window W2. The infrared beam, which is polarised perpendicular to the sample surface, is then reflected at an angle of near grazing incidence off the single crystal metal surface and exits the chamber through window W3 before being focussed onto the far-infrared liquid helium cooled silicon bolometer detector. This experimental set-up allows the spectral range 200 to 600 cm^{-1} to be investigated.

2.4 References

1. J. C. Vickerman, Surface Analysis - The Principal Techniques, John Wiley & Sons Ltd, Chichester, (1997).
2. M. H. Hablanian, High-Vacuum Technology : A Practical Guide, Dekker, New York, (1990).
3. E. M. McCash, Surface Chemistry, Oxford University Press, Oxford, (2001).
4. G. A. Somorjai, Introduction to Surface Chemistry and Catalysis, John Wiley & Sons Ltd, New York, (1994).
5. D. P. Woodruff and T. A. Delchar, Modern Techniques of Surface Science, Cambridge University Press, Cambridge, (1986).
6. M. P. Seah and D. Briggs, Practical Surface Analysis by Auger and X-ray Photoelectron Spectroscopy, John Wiley, New York, (1990).
7. G. A. Attard and C. Barnes, Surfaces, Oxford University Press Inc., New York, (1998).
8. L. J. Clarke, Surface Crystallography - An Introduction to Low Energy Electron Diffraction, Academic Press, (1985).
9. P. W. Atkins, Physical Chemistry, 6th, Oxford University Press, Oxford, (1998).
10. J. D. E. McIntyre and D. E. Aspnes, Surf. Sci. 24 (1971) 417.
11. R. G. Greenler, J. Chem. Phys. 44 (1966) 310.

12. R. G. Greenler, J. Chem. Phys. 50 5 (1969) 1963.
13. R. G. Greenler, J. Vac. Sci. Technol. 12 6 (1975) 1410.
14. P. R. Griffiths, Transform Techniques in Chemistry, Heyden, London, (1978).
15. R. J. Bell, Introductory Fourier Transform Spectroscopy, Academic Press, New York, (1972).
16. J. Chamberlain, The Principles of Interferometric Spectroscopy, John Wiley, Chichester, (1979).
17. A. A. Michelson, Phil. Mag. 31 (1891) 256.
18. A. A. Michelson, Phil. Mag. 34 (1892) 280.
19. Rayleigh, Phil. Mag. 34 (1892) 407.
20. H. Winick and S. Doniach, Synchrotron Radiation Research, Plenium Press, New York, (1980).
21. J. R. Stevenson, H. Ellis, and R. Bartlett, Appl. Opt. 12 (1973) 2884.
22. P. Meyer and P. Lagarde, J. Phys. 37 (1976) 1387.
23. G. P. Williams, Nucl. Instrum. Method Phys. Res. 195 1-2 (1982) 383.
24. J. Yarwood, T. Shuttleworth, J. B. Hasted, and T. Nanba, Nature 312 5996 (1984) 742.
25. J. Yarwood, Chem. Br. 22 5 (1986) 423.
26. D. A. Slater, P. Hollins, M. A. Chesters, J. Pritchard, D. H. Martin, M. Surman, D. A. Shaw, and I. H. Munro, Rev. Sci. Instrum. 63 1 (1992) 1547.

Chapter Three – Theoretical Methods

3.1 Introduction

In order to aid the interpretation of the experimental infrared data, a series of *ab initio* calculations were preformed. These calculations aim to provide information on the adsorption structures and energetics together with details of the energies of the vibrational modes of each individual system being studied, and the atomic movements associated with each mode. This information can then be used firstly for comparison with, and then to explain, the far-infrared spectra recorded on the Pt(111)-CO and Pt(110)-CO systems.

The calculations presented in this thesis were performed in two stages. The first stage was to optimise the geometry of the desired system. This was performed using the CASTEP code [1], which is based on density functional theory (DFT) within a plane-wave pseudopotential formalism, aided by the CERIUS^2 front-end [2]. Once the geometry had been optimised, a series of calculations were performed to evaluate the force constant matrix for the system using a finite difference algorithm to construct second derivatives of the energy. Standard plane wave DFT enables forces to be rapidly determined with a high degree of precision. The derivatives of the forces can then be constructed using a three-point finite difference approach. This allowed us to construct the force constant matrix which, upon diagonalisation, yielded the gamma-point phonon modes of the system, and hence the infrared vibrations.

3.2 *Geometry Optimisation*

3.2.1 DFT using plane-wave pseudopotentials

Since most properties of macroscopic materials depend on microscopic phenomena, quantum mechanical methods, such as density functional theory, can be used to calculate these macroscopic properties from first principals (*ab initio*).

All *ab initio* calculations on a system involve following the same steps. These steps are:

1. Write down the Hamiltonian operator, H, for the system.
2. Select some mathematical functional form, φ, as the trial wavefunction, with variable parameters.
3. Minimise the energy in the Schrödinger equation,

$$H\varphi = E\varphi \qquad \textbf{3.1}$$

with respect to the variations in the parameters.

In practice, the complete hamiltonian is not usually used. The complete Hamiltonian includes nuclear and kinetic energy operators, electronic interactions between all charged particles, and interactions between all magnetic moments due to spin and orbital motions of nuclei and electrons. Also an accounting for the fact that a moving particle experiences a change in mass due to relativistic effects is included in the complete Hamiltonian. The resulting Hamiltonian is too complicated to work with. Usually, relativistic mass effects are ignored, the Born-Oppenheimer approximation is made (to remove nuclear kinetic energy operators), and all magnetic interactions are ignored (except in special cases where spin coupling is of interest). This results in the energy, written in terms of the electron wavefunction, being written in the form

$$E[\phi(x)] = T_s[\phi(x)] + E_{ee}[\phi(x)] + E_{ext}[\phi(x)] + E_x[\phi(x)] \qquad \textbf{3.2}$$

where, $T_s[\phi\ (x)]$ is the kinetic energy of non-interacting electrons as a function of the electron wavefunction,

$E_{ee}[\phi\ (x)]$ is the electrostatic energy as a function of the electron wavefunction,

$E_{ext}[\phi\ (x)]$ is the potential energy of non-interacting electrons as a function of the electron wavefunction

and, $E_x[\phi\ (x)]$ is the exchange energy as a function of the electron wavefunction.

The existence of correlations between the electrons is the main formal difficulty encountered in determining a material's properties within quantum mechanics. The positions and motions of the particles that make up a molecule or material are correlated because the particles interact with each other and exert forces upon each other as they move. In quantum mechanics, the Pauli exclusion principle indicates that two spin parallel electrons will tend to avoid each other, which leads to a relatively small electrostatic interaction. Two spin antiparallel electrons do not have the same restriction from the Pauli exclusion principle and hence, on average, will be closer together and have a larger electrostatic interaction. This gives a situation where the spin of the electrons couples to their electrostatic energy, giving an extra energy term, known as the exchange energy, which is dependant on the spin of the electrons. The exchange energy enables the electrostatic interactions to be treated the same regardless of the spin of the electrons.

The correlation energy is defined as the difference between the answer given by Hartree-Fock calculations, which include the electrostatic, exchange and kinetic energy terms, and the true answer. By this definition, Hartree-Fock theory gives inaccurate answers to strongly correlated systems because the correlation

energy is large. Therefore, an alternative method is needed to more accurately calculate strongly correlated systems.

Several promising methods of dealing with the problem of strongly correlated systems have been developed in recent years but this is still at the cutting edge of research in condensed matter physics and none of these methods is sufficiently mature for use as a general software tool. An important advance in the calculation of the energy of collections of atoms and the forces on each atom was made by Kohn and Sham [3], who showed how a mean-field theory could be applied to this problem. In their method, the electron density plays a crucial role so that, although the term has more general applicability, the Kohn-Sham method is commonly referred to as density functional theory (DFT). This has since advanced to become a very important method for determining the energy of many-electron, and therefore many-atom systems. In addition, Kohn-Sham density functional theory is equally applicable to molecules (bonded collections of atoms) and crystalline materials (where a specific unit cell is repeated throughout space).

In density functional theory, the energy is not written in terms of the electron wavefunction (as is conventional in quantum chemistry) but instead is written as a functional of the electron density. Kohn and Sham showed that the energy functional for a system of electrons with external field $V_{ext}(x)$ can be written in the form

$$E[\rho(x)] = T_s[\rho(x)] + E_{ee}[\rho(x)] + E_{xc}[\rho(x)] + E_{ext}[\rho(x)] \qquad \textbf{3.3}$$

where, $T_s[\rho(x)]$ is the kinetic energy of non-interacting electrons having density $\rho(x)$

$E_{ee}[\rho(x)]$ is the electrostatic energy

$E_{xc}[\rho(x)]$ is the so-called exchange-correlation energy

and, $E_{ext}[\rho(x)]$ is the potential energy of non-interacting electrons having density $\rho(x)$ in the external field $V_{ext}(x)$.

The important advance of the Kohn and Sham functional was the correction of a defect of earlier forms for the density functional (such as the Thomas-Fermi-Dirac functional [4, 5]) with regard to reproducing the shell structure of atoms. This is achieved in the Kohn-Sham functional via the kinetic energy term which is expressed by a set of orbitals, ϕ_n, emanating from a one-particle Schrödinger equation;

$$T_S[\rho(x)] = \sum_n a_n \int dx \phi_n(x) \left\{ -\frac{\hbar^2 \nabla^2}{2m} \right\} \phi_n(x) \qquad \textbf{3.4}$$

The link between T_s and $\rho(x)$ is then indirect, via the orbitals, ϕ_n, in terms of which

$$\rho(x) = \sum_n a_n |\phi_n(x)|^2 \qquad \textbf{3.5}$$

Here the a_n are occupation numbers that determine the electron configuration. $T_s[\rho(x)]$ and $\rho(x)$, as given by Equations 3.4 and 3.5 respectively, provide the required link between a density and the kinetic energy with which it is associated.

For purposes of practical calculation, the Kohn-Sham functional must be supplemented by an approximation for the exchange and correlation term. The traditional approximation, proposed by Kohn and Sham, is referred to as the local density approximation (LDA) and takes the form

$$E_{xc}^h[\rho(x)] = \int dx \rho(x) \varepsilon_{xc}^h(\rho(x)) \qquad \textbf{3.6}$$

where $\varepsilon_{xc}^h(\rho(x))$ is the exchange correlation energy of a uniform electron gas having density ρ. Although this form of the exchange correlation energy appears to be valid only in the limit that the electron density is slowly varying (in

which case Equation 3.6 is the first term in a gradient expansion), other calculations have shown that the expression remains relatively accurate in general, even when the density is so rapidly varying that a gradient expansion of it does not exist. Arguments of a dimensional nature having nothing to do with gradient expansions help to explain the general accuracy of Equation 3.6 and suggest why this expression gives a reasonable estimate of the exchange correlation energy irrespective of the nature of the density distribution. The quantity $\varepsilon_{xc}^{h}(\rho(x))$ has been calculated in several ways by different groups. The calculations give similar, but not identical results. The differences to be expected on switching from one LDA functional to another are, in general, only marginal.

The LDA remained the approximation of choice for most calculations for many years (and still is for some applications, particularly in extended systems). In applications to molecules, however, it was found that the LDA tends to over-bind (too large values of molecular binding energies). This can be understood as a consequence of a known defect of Equation 3.6 in regions of low electron density. Here, the exact form of $\varepsilon_{xc}^{h}(\rho(x))$ is known (it is an electrostatic interaction having the functional form of a power law) and deviates greatly from the LDA which falls off exponentially with the electron density. This means that the exchange correlation contribution emanating from regions of low electron density is underestimated, which, in turn, implies that the difference in energy between two systems whose electron distributions have different surface areas will be in error. This is the case when two atoms combine to form a molecule and the sign of the effect is consistent with overbinding of the molecule.

Over the past decade, a class of corrections to the LDA has been developed that correct this deficit to a large extent by going over explicitly to the power law form in regions of low density. This is usually done by introducing a dependence on the gradient of the density and the new class of corrected exchange-correlation functionals is referred to as gradient corrected or Generalized Gradient Approximations (GGA). The use of gradient corrections has little influence on local properties such as bond lengths or vibration frequencies, but does lead

usually to a significant improvement in global changes in the energy such as those that result when two atoms form to make a molecule, or a molecule binds on a surface. The hunt for yet further improvement in exchange-correlation functionals continues, (particularly via the inclusion of non-local exchange and correlation potentials), though this is unsystematic and there is no guarantee that higher accuracy can be attained than is already exhibited by the functionals commonly in use today.

The energy of a system of electrons in an external field (such as that due to a collection of nuclei) is given by minimising the density functional energy given by Equation 3.3. This is equivalent to solving a set of Kohn-Sham equations comprising a one-particle Schrödinger equation together with a so-called self-consistency condition. The Schrödinger equation links the input potential to the output density:

$$\left\{-\frac{\nabla^2}{2m}+V_{eff}(x)-\varepsilon_n\right\}\phi_n(x)=0 \qquad \textbf{3.7a}$$

$$V_{eff}(x)=V_{ext}(x)+\Phi(\rho(x))+\mu_{xc}(\rho(x)) \qquad \textbf{3.7b}$$

where Φ is the Coulomb potential corresponding to $\rho(x)$,

$$\mu_{xc}(\rho)\equiv\frac{d}{d\rho}\left[\rho\varepsilon_{xc}^{h}(\rho)\right] \qquad \textbf{3.8}$$

and the output density, $\rho(x)$, is given in terms of the orbitals by Equation 3.5. Equations 3.7a and 3.7b are usually solved by iteration. Beginning with an initial potential, Equation 3.7a is solved to produce a new density calculated from the orbitals via Equation 3.5. Then this density is used to form a new potential for Equation 3.7a. The self-consistency cycle is then continued until the in potential and the out-density satisfy Equation 3.7b to some desired accuracy. This often

involves many iterations because the self-consistency procedure may be unstable. Sophisticated feedback techniques are necessary to prevent oscillations.

Once self-consistency is achieved, the output from the calculation includes the energy, Equation 3.3, its derivatives with respect to the nuclear coordinates (i.e., the atomic forces), the eigenvalues of Equation 3.7a (which in extended systems give the energy bands), and the one electron orbitals $\rho(x)$. According to formal density functional theory, only the energy and its derivatives (the forces on the atoms) have physical significance. However, practical calculation over many decades has shown that many other quantities, calculated approximately in a one-electron picture using the eigenvalues (energy bands) and orbitals or Equation 3.7a, are given with equal accuracy.

The solution of the Kohn-Sham equations, Equations 3.7a and 3.7b, for a collection of atoms, whether in a molecule, cluster or extended solid provides a wealth of information about the system. This includes structural information, such as the equilibrium geometry, and a wide variety of important electronic properties. In addition, dynamical and thermal behaviour can be studied using forces generated by the solution of the Kohn-Sham equation in, e.g., molecular dynamics calculations (so-called *ab initio* molecular dynamics). Although Equations 3.7a and 3.7b are very much simpler than standard quantum mechanics, because the electrostatic interaction is treated via a mean-field, this does not mean that they can be easily solved. The functional dependence of the exchange correlation energy density on the electron density is non-analytic, so exact, analytic solutions are not possible even for the hydrogen atom. Methods yielding numerically exact solutions are possible, but only for very small systems (atoms and small, light molecules). In general, approximate methods must be used. Over the years, a number of standard methods have been applied with varying degrees of success. Each has strengths and weaknesses in terms of the systems and/or properties for which it is most accurate.

The CASTEP programme, used in this thesis, employs weak plane-wave pseudopotentials [6, 7] to solve Equations 3.7a and 3.7b, as this is the most accurate method of representing atoms in a repeating lattice.

The electron orbitals used to express the single particle density in Equations 3.7a and 3.7b may be expanded in terms of any complete basis set. In practice a plane wave basis set is used as this gives a number of benefits.

1. A plane wave basis set is unbiased, it does not assume any preconceptions of the form of the problem.
2. Due to Bloch's theorem [8], plane waves are the natural choice for the representation of electron orbitals in a periodic system.
3. They are computationally simple because maths with exponentials is easy. Millions of plane waves are needed to accurately describe the system being calculated compared to a relatively small number of local basis functions, but the ease of manipulation makes the plane waves straightforward to work with.

The electronic wavefunction in a periodic system, according to Bloch's theorem [8], takes the form

$$\varphi_{n,\underline{k}}(\underline{x}) = \phi_{n,\underline{k}}(\underline{x}) \exp[i\underline{k}.\underline{x}] \qquad \textbf{3.9}$$

with a wavevector $\underline{k}$, a band index n, and a function $\phi_{n,\underline{k}}(x)$ which is periodic in space, with the periodicity of the primitive cell:

$$\phi_{n,\underline{k}}(\underline{x}+\underline{R}) = \phi_{n,\underline{k}}(\underline{x}) \qquad \textbf{3.10}$$

for any lattice vector $\underline{R}$. In the plane wave representation, this periodic function can therefore be expanded as:

$$\phi_{n,\underline{k}}(\underline{x}) = \frac{1}{\sqrt{\Omega}} \sum_{G} C_{n,\underline{k},\underline{G}} \exp[i\underline{G}.\underline{x}], \qquad \textbf{3.11}$$

where Ω is the volume of the primitive cell and $\underline{G}$ are the reciprocal space vectors.

The principal disadvantage of a plane wave basis set is its inefficiency. The number of basis functions needed to describe atomic wavefunctions accurately near to a nucleus would be prohibitive. This difficulty is overcome by the use of Pseudopotentials to represent the potential of the ionic cores. This approximation makes the assumption that only the valence electrons determine the physical properties of the system. The pseudopotential represents the potential of the nucleus and the core electrons subject to the following conditions,

1. The valence wavefunction remains unchanged outside the core region.
2. The pseudowavefunction within the core matches correctly at the boundary.
3. The pseudopotential is chosen to make the pseudowavefunction as smooth as possible

An example of a pseudopotential and pseudowavefunction can be seen in Figure 3.1.

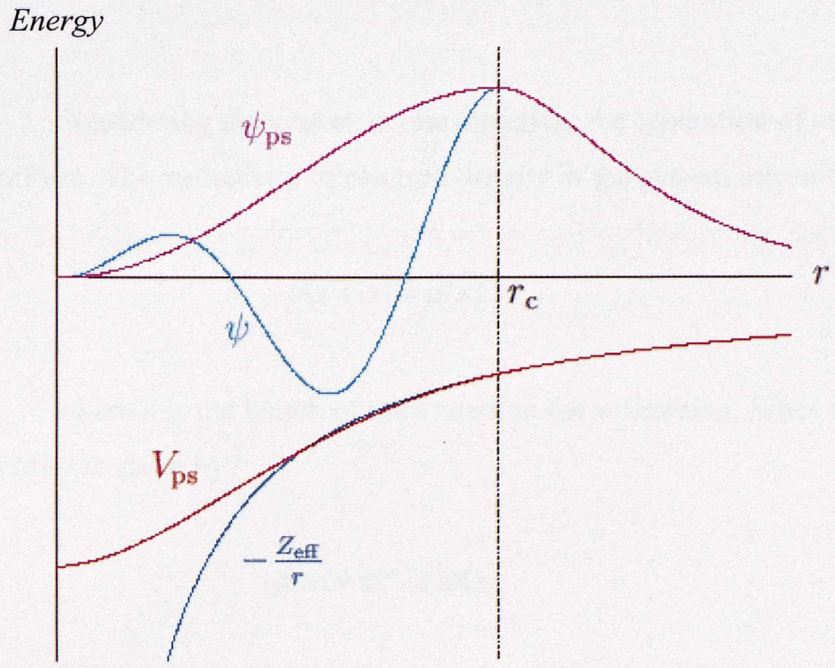

Figure 3.1 - A schematic illustration of all-electron (blue lines) and pseudoelectron (red lines) potentials and their corresponding wavefunctions. The radius at which all-electron and pseudoelectron values match is r_c [9].

3.3 Accuracy and Convergence

There are a number of main parameters that can be changed in the calculation set-up of the CASTEP program. A convergence test was carried out for each of these parameters to determine, in each case, the most appropriate value in order to give a balance between computing time and calculation accuracy.

3.3.1 k-points

The calculations in this thesis use the concept of periodic boundary conditions. This allows a smaller finite system to be used to calculate the properties of a much larger system by being repeated in all three directions in space. These periodic boundary conditions mean that the wavefunction must have the same value at opposite edges of the system to remain continuous.

Considering the system in one direction, the separation of each system is uniform. The periodicity of electron density in the system means that:

$$\rho(x+a)=\rho(x) \qquad \textbf{3.12}$$

where a is the length of the system in the x direction. Since the electron density is given by

$$\rho(x)=\varphi^{*}(x)\varphi(x) \qquad \textbf{3.13}$$

Equation 3.12 can only be achieved if

$$\varphi(x+a)=\mu\varphi(x) \qquad \textbf{3.14}$$

where μ is a complex number such that

$$\mu^{*}\mu=1 \qquad \textbf{3.15}$$

The effect of translation through a number of system lengths, say n, gives

$$\varphi(x+na)=\mu^{n}\varphi(x) \qquad \textbf{3.16}$$

The assumption of periodic boundary conditions then implies that μ must satisfy the equation

$$\mu^{n}=1 \qquad \textbf{3.17}$$

Thus μ must be given by a complex nth root of unity. There are n different solutions of Equation 3.17, given by the general formula:

$$\mu = \exp\left(\frac{2\pi i p}{n}\right) \qquad \textbf{3.18}$$

where p is an integer and $i = \sqrt{-1}$. p can be regarded as a quantum number that labels the wavefunctions. However, it is usual to define p in terms of another quantum number, k, where

$$k = \frac{2\pi p}{na} \qquad \textbf{3.19}$$

For a finite number of systems, k can only take on discrete values by putting $p = 0, \pm 1, \pm 2, \ldots$ in Equation 3.19. However, in the extended lattices studied in this thesis n is very large, and the difference between successively allowed values of k is very small. So, in practice, k can be regarded as a continuous variable.

Returning to Equation 3.14, it is seen that the effect of translating the system by one spacing is given by

$$\varphi(x+a) = \exp(ika)\varphi(x) \qquad \textbf{3.20}$$

One possible wavefunction that satisfies this equation is that corresponding to free electron waves:

$$\varphi(x) = \exp(ikx) = \cos(kx) + i\sin(kx) \qquad \textbf{3.21}$$

Therefore, from Equation 3.21, it can be seen that different values of k give different periodicities of wavefunctions. These wavefunctions all have different energies, related to their wavelengths, and hence related to k. The energy of the electrons plotted against k is shown in Figure 3.2.

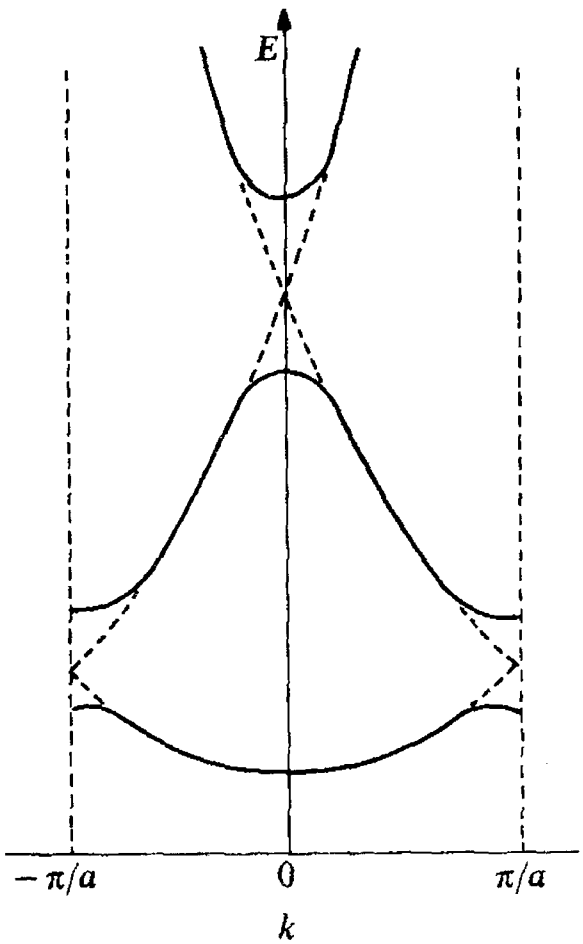

Figure 3.2 – Electron energy as a function of *k*.

k is only shown from $-\frac{\pi}{a}$ to $+\frac{\pi}{a}$, since to include values of *k* outside this region would lead to duplication of the crystal orbitals. The distribution of the energy of the electrons in the system is given by the horizontal integration of the curves in Figure 3.2. In order to define perfectly this distribution, every value of *k* from $-\frac{\pi}{a}$ to $+\frac{\pi}{a}$ must be sampled. In reality this would involve too much computation time, so only a certain number of *k*-points are sampled. The minimum number of *k*-points required for the calculations performed in this thesis to accurately describe the band structure was determined by a series of trial calculations, the results of which are shown in Figure 3.3. Figure 3.3 shows that 60 *k*-points, covering all three dimensions, were required to maintain a high level

of accuracy in the calculations. Therefore this was the number of *k*-points used in all the calculations reported in this thesis.

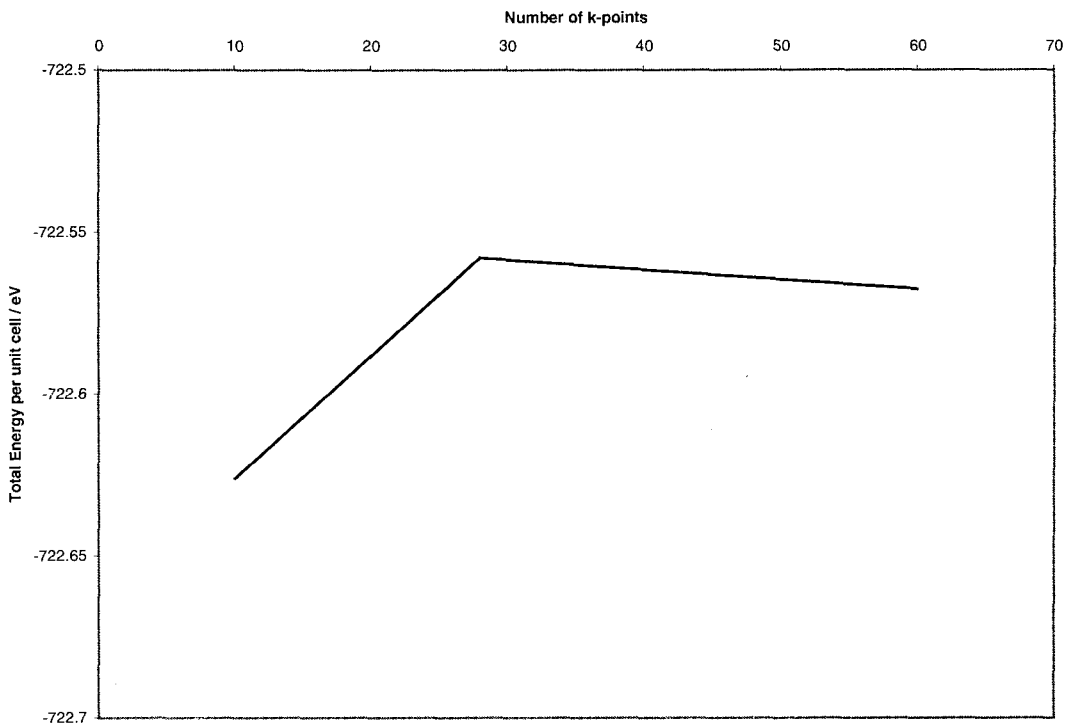

Figure 3.3 – Convergence test for the number of k-points on the Pt(110) system

3.3.2 Plane-wave energy cutoff

The accuracy of the calculation is determined by the number of plane waves in the series, as determined by Equation 3.11. In practice, this is commonly controlled through a maximum value for the contribution to the kinetic energy expression, shown in Equation 3.22

$$T_n = \frac{1}{2\Omega}\sum_G \left|\underline{k}+\underline{G}\right|^2 \left|C_{n,k}\right|^2 \qquad \textbf{3.22}$$

Only those vectors $\underline{G}$ are taken into account which satisfy

$$\frac{1}{2}|\underline{k}+\underline{G}|^2 \leq E_c \qquad \textbf{3.23}$$

Where E_c is the cut-off energy. This led to a set of test calculations being carried out on the Pt(110) system where only the energy cut-off parameter was altered. Figure 3.4 shows that by an energy cut-off value of 400 eV there was no significant lowering of the total energy of the system. Therefore this value was used as the cut-off energy for all calculations.

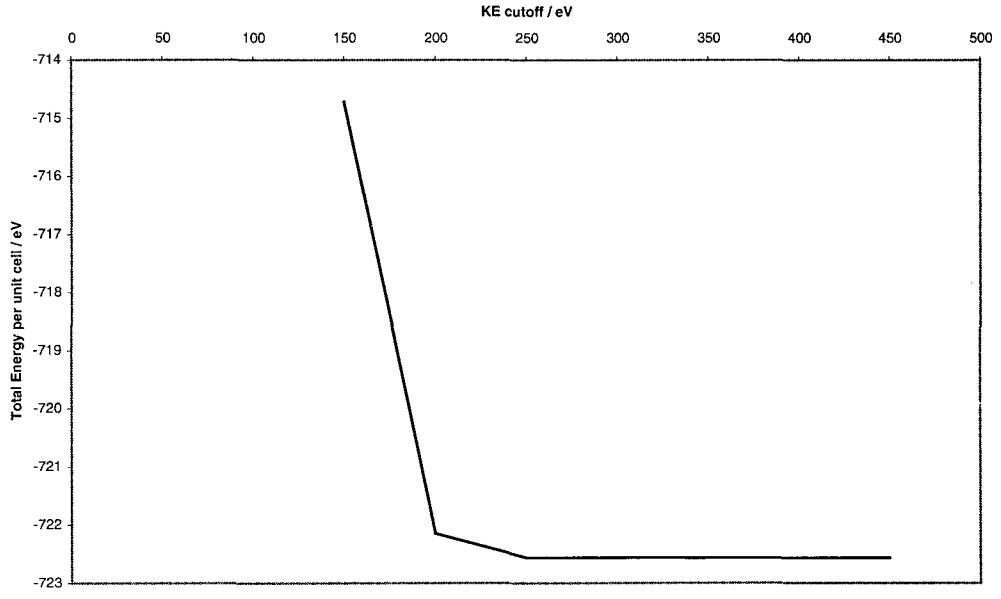

Figure 3.4 – Convergence test for the cut-off energy on the Pt(110) system

3.3.3 Slab thickness and slab separation distance

The calculations reported in this thesis are set up as an infinite number of parallel layers, or slabs, of a certain thickness and separation distance. This

enables the calculation to have periodic boundary conditions in all three principal directions as required if we are to use a plane wave basis set. Both parameters, thickness and separation distance, have direct influences on the accuracy of the calculation. Because the calculations are being used to model a surface with a depth of many billions of atoms, the larger the thickness of the slab in the calculation the more accurate the calculation will be. Unfortunately, as the slab thickness is increased, so too are the number of atoms in the primitive cell, and so the CPU time increases dramatically. Therefore, the next test to be carried out was to increase only the number of atomic layers in the slab on the Pt(110) system, and compare the total energies of each calculation, the results of which are shown in Figure 3.5. From Figure 3.5 it can be seen that the most appropriate slab thickness is 8 layers of platinum, and so this value was used for all subsequent calculations.

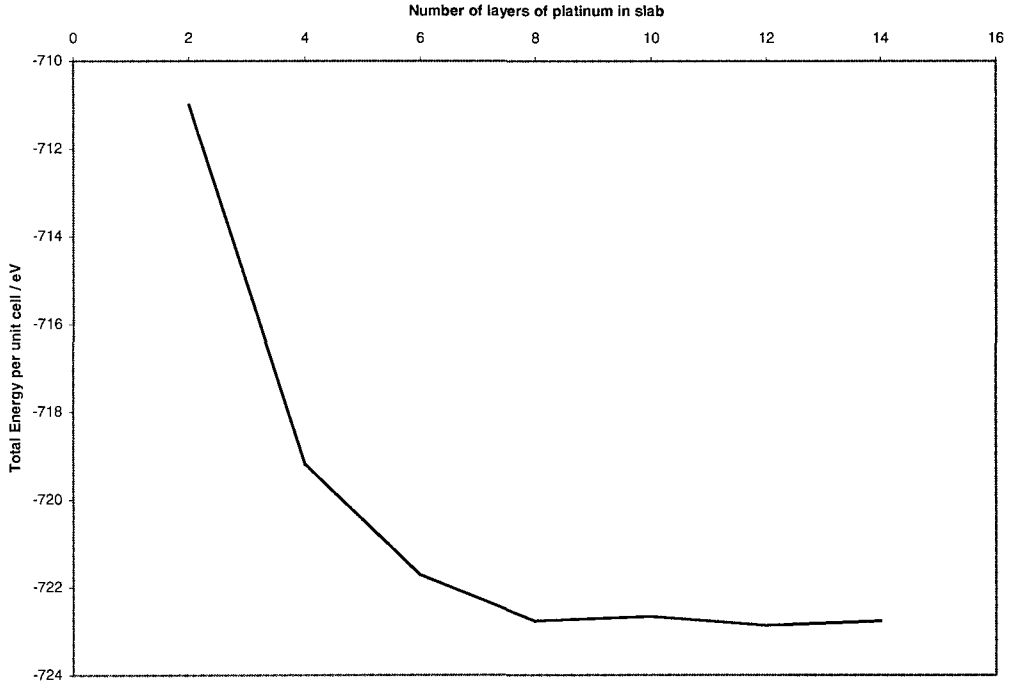

Figure 3.5 – Convergence test for the slab thickness on the Pt(110) system

It was also necessary for a convergence test to be carried out for the slab separation distance parameter. As the slabs move further apart the calculations

become more accurate because the interactions between each slab become less and less. The convergence test for slab separation distance, shown in Figure 3.6, shows that the slabs must be separated by at least 12.3 Å in order to be as accurate as possible.

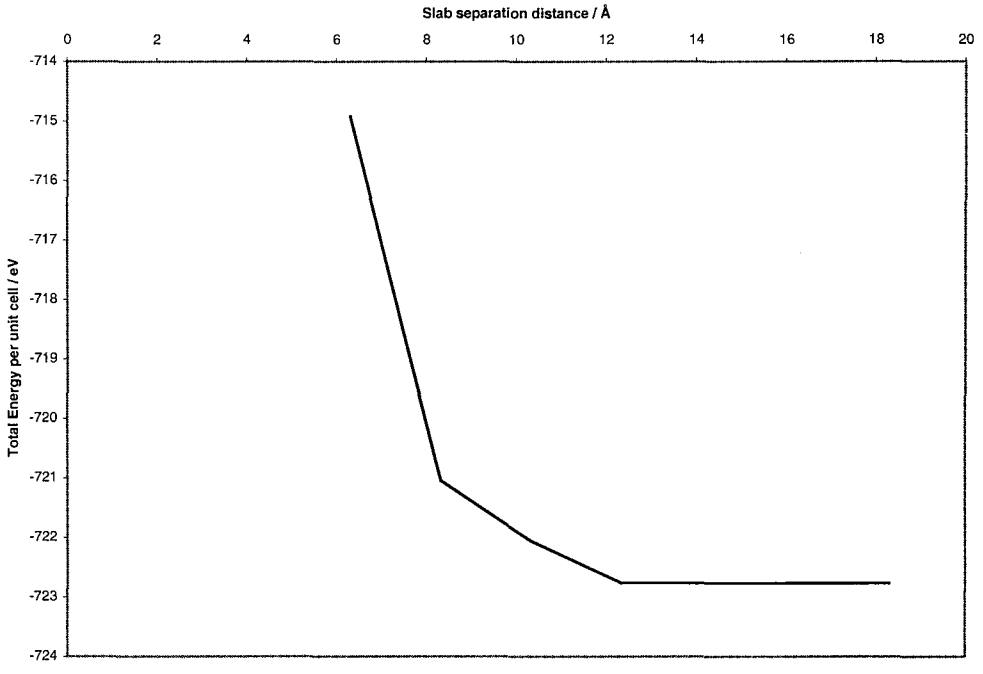

Figure 3.6 – Convergence test for the slab separation distance on the Pt(110) system

3.4 Calculation of Phonon Modes

In order to calculate the infrared vibrations it is first necessary to determine how the forces present on one atom in the system effect the movement of all the other atoms. To do this, a series of parallel calculations are carried out.

Each calculation comprises of moving one atom a very small distance, in either the x, y, z, -x, -y, or -z direction, away from its equilibrium position, as calculated in the geometry optimisation, and calculating the forces at that point

and the forces at the point twice that distance away. These values are then used to calculate the gradient of the force acting on the initial atom by a finite difference approach [10]. The same approach is then used to calculate the finite difference of the forces acting on each of the other atoms in the system about their equilibrium position, again in each of the six directions, whilst the other atom is one step away from equilibrium. This whole procedure is then repeated for all possible movements.

From this, a force constant matrix can be constructed which describes all of the movements of the system in terms of the movements of each of the atoms along the x, y, z directions [11]. The diagonalisation of this matrix gives the movements of the system in terms of a new set of eigenvectors, which are all linear combinations of the movements of the atoms along the x, y, and z directions. These movements are the infrared modes of the system, and the eigenvalues associated with each mode give the energy related to that mode. This means that not only are the energies of each vibration calculated, but also the associated movements of the atoms.

In this thesis, calculated vibrational frequencies for CO adsorption on Pt(110) are reported in Chapter five. Frequencies have been calculated for CO adsorbed in both atop and two-fold bridge sites on both the Pt(110)-(1x1) and Pt(110)-(1x2) substrates. Similar calculations on the Pt(111)-CO system performed by Hassel [12] are discussed in Chapter four.

3.5 References

1. M. C. Payne, M. P. Teter, D. C. Allan, T. A. Arias, and J. D. Joannopoulos, Rev. Mod. Phys. 64 4 (1992) 1045.
2. Acelrys, CERIUS, (1993).
3. W. Kohn and L. J. Sham, Phys. Rev. 140 4A (1965) 1133A.
4. L. H. Thomas, Proc. Cambridge Phil. Soc. 48 (1927) 542.

5. E. Fermi, Z. Physik 48 (1928) 73.
6. N. Troullier and J. L. Martins, Phys. Rev. B 43 3 (1991) 1993.
7. D. Vanderbilt, Phys. Rev. B 41 11 (1990) 7892.
8. P. A. Cox, The Electronic Structure and Chemistry of Solids, Oxford University Press, New York, (1987).
9. B. Jensen, Acta Chem. Scand. B 29 (1975) 531.
10. M. P. Allen and D. J. Tildesley, Computer Simulation of Liquids, Oxford University Press, New York, (1987).
11. G. P. Srivastava, The Physics of Phonons, Adam Hilger, Bristol, (1990).
12. M. Hassel, J. Chem. Phys. 114 1 (2001) 530.

Chapter Four – Far Infrared Studies of Carbon Monoxide Adsorption on Pt(111) [a]

4.1 Introduction

Bulk platinum metal has a face centred cubic structure [1]. When this is cut along the (111) plane, as defined by Miller indices [2], this leads to a surface of hexagonally arranged atoms, as shown in Figure 4.1. The ideal Pt(111) surface is entirely flat, and has three distinctly different adsorption sites. These adsorption sites are (a) atop, (b) bridged and (c) three-fold hollow, and are shown in Figure 4.1.

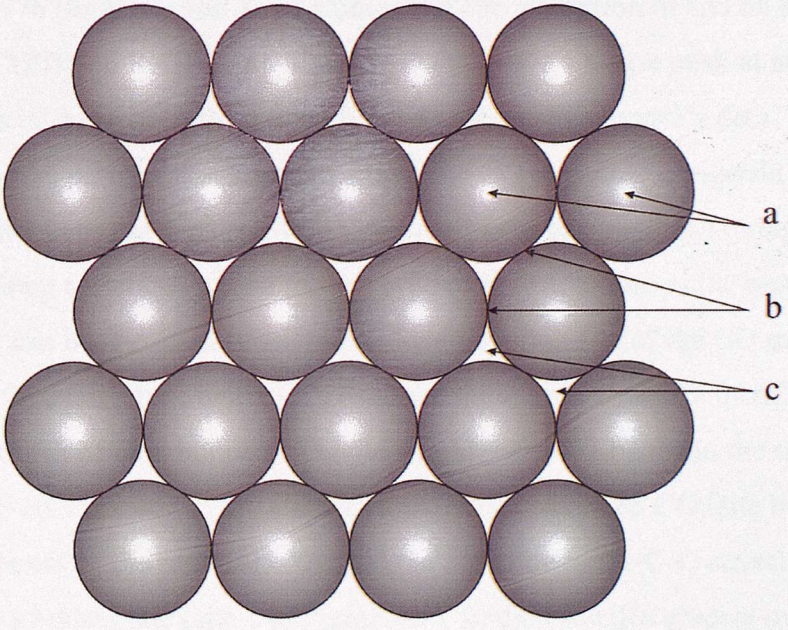

Figure 4.1 – Diagram of the arrangement of atoms in a Pt(111) surface and highlighting the three different adsorption sites

---

a) Portions of this chapter have been previously published.

M. Surman, P.L. Hagans, N.E. Wilson, C.J. Baily, A.E. Russell, Surf. Sci. 511 (2002) L303.

The structure of clean Pt(111), as shown above, was first confirmed in a series of LEED (low energy electron diffraction) studies by the Somorjai group in the late 1960's [3, 4]. They obtained a hexagonal LEED pattern from their Pt(111) crystal, which is exactly what would be expected from the structure shown in Figure 4.1. When carbon monoxide was adsorbed onto the Pt(111) surface a c(4 × 2) diffraction pattern was observed, which was said to be due to CO adsorbing in a c(4 × 2) arrangement with domains at 60° to each other. In 1974 Lambert and Comrie performed the first TPD (temperature programmed desorption) experiments for CO adsorbed on a Pt(111) recrystallised ribbon [5]. Their data showed only one peak at 573 K which was interpreted by CO adsorbing non-dissociatively on Pt(111) at 300K into a single binding state. This contrasts with the two peaks at 430 K and 520 K, denoted α and β respectively, seen in various TPD experiments of CO on polycrystalline platinum ribbon [6, 7].

In 1976 Shigeishi and King studied the chemisorption of CO on a Pt(111) ribbon by TPD and RAIRS [8]. Their TPD data gave a single peak at about 650 K, which was interpreted in the same way as Lambert and Comrie's data. To investigate the particular adsorption site of the CO molecule, Shigeishi and King used RAIRS to probe the stretching vibration of the adsorbed CO molecule. This is an excellent technique to use for this type of investigation, as the position of any bands can be specifically related to the adsorption site of the CO molecule. In the case of the adsorbate being CO, bands in the region 2000-2200 cm^{-1} are due to the C-O stretch of atop bonded CO (site a in Figure 4.1), bands in the region 1800-1900 cm^{-1} are due to the C-O stretch of bridge bonded CO (site b in Figure 4.1), and bands in the region 1700-1800 cm^{-1} are due to the C-O stretch of CO bonded in a hollow site (site c in Figure 4.1). In their RAIRS studies over the range 1500cm^{-1} to 2200 cm^{-1}, Shigeishi and King only observed one band. This band had an initial peak position of 2065 cm^{-1} at low coverages of CO which shifted continuously to 2100 cm^{-1} when saturation had occurred. This implied that there was only one CO species on the surface, and it was adsorbed in an atop site.

The chemisorption of CO on a platinum film was monitored using RAIRS by Hoffmann and Bradshaw [9]. As in the work by Shigeishi and King on the Pt(111) surface [8], Hoffmann and Bradshaw also observed only one peak, centred at about 2080 cm^{-1} and dependent on coverage, despite carefully searching down to 1750 cm^{-1}, and so also believed the CO to adsorb exclusively in atop sites.

Ertl *et al.* presented the first CO TPD experiments undertaken on a Pt(111) single crystal, rather than a recrystallised Pt ribbon [10]. Their TPD data showed a marked difference to those taken on the ribbons, as they observe a single, coverage dependant peak centred below 500 K in contrast to the TPDs from ribbons where the single peak is observed at temperatures above 500 K [5-7]. When CO was adsorbed on Pt(111) at 170 K, Ertl *et al.* observed a change in the LEED pattern from a $(\sqrt{3} \times \sqrt{3})R30°$ pattern at a coverage of $\theta = \frac{1}{3}$ (about 1 L exposure) to a $c(4 \times 2)$ pattern at $\theta = \frac{1}{2}$ (about 2 L exposure) [10]. This change in LEED pattern was attributed to a continuous uniaxial compression of the unit cell of the adsorbate structure along the [110] direction with increasing coverage, and is shown schematically in Figure 4.2.

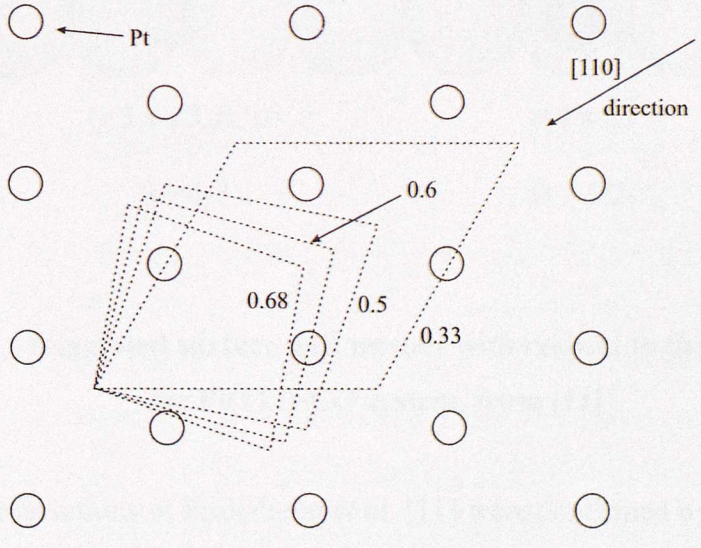

Figure 4.2 – Primitive unit cells for ordered adsorbate structures at different coverages, indicated by the numerical values, as derived from the LEED patterns, from [10]

An important breakthrough occurred in 1977, when Froitzheim *et al.* studied the Pt(111)-CO system using the HREELS (high resolution electron energy loss spectroscopy) technique [11]. At low coverages of CO (giving a $(\sqrt{3} \times \sqrt{3})/R30°$ LEED pattern), they observed two vibrational modes at 58 meV (464 cm^{-1}) and ~260 meV (2080 cm^{-1}). When the exposure of CO was increased to above 0.2 L (giving a c(4 × 2) LEED pattern), two additional modes developed at 45 meV (360 cm^{-1}) and 232 meV (1860 cm^{-1}). The low coverage modes were assigned to the Pt-CO stretch (58 meV) and C-O stretch (260 meV) of atop bonded CO (site a in Figure 4.1), and the additional modes were assigned to the Pt-CO stretch (45 meV) and C-O stretch (232 meV) of bridge bonded CO (site b in Figure 4.1). This led to Froitzheim *et al.* suggesting the surface unit meshes shown in Figure 4.3.

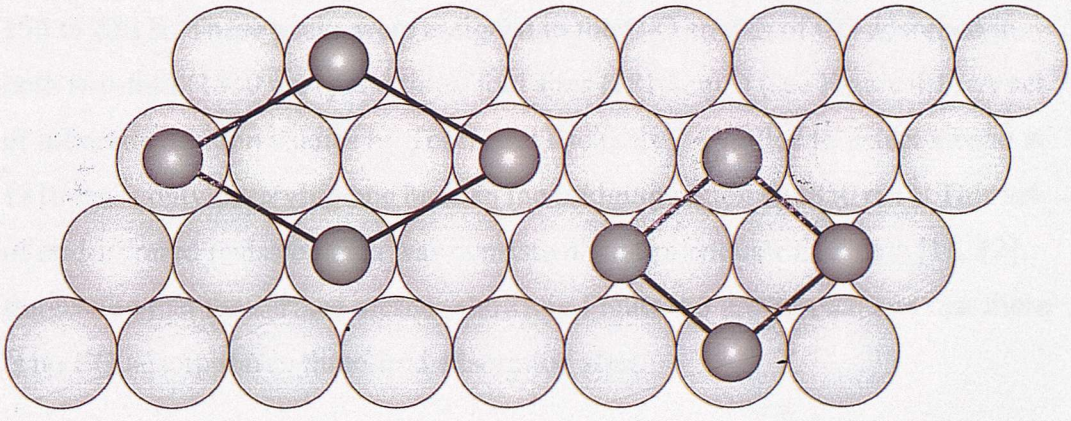

Figure 4.3 – Suggested surface unit meshes with respect to the substrate for the Pt(111)-CO system, from [11]

The observations of Froitzheim *et al.* [11] were confirmed by a set of experiments carried out by Steininger *et al.* combining the techniques of LEED and EELS [12]. Steininger *et al.* monitored the adsorption of CO on Pt(111) by recording the LEED and EELS data at different coverages of CO. Their data showed that at $\theta_{CO} = 0.17$ the LEED pattern was $(\sqrt{3} \times \sqrt{3})/R30°$ and there were

only peaks in the EELS spectrum due to atop bonded CO (2100 cm^{-1} and 470 cm^{-1}). Increasing the coverage to $\theta_{CO} = 0.5$ caused the LEED pattern to change to c(4 × 2), whilst in the corresponding EELS spectrum two extra peaks appeared due to bridge bonded CO (1850 cm^{-1} and 380 cm^{-1}). The work by Steininger *et al.* [12] therefore showed that the structure of the Pt(111)-CO system suggested by Froitzheim *et al.* [11], illustrated in Figure 4.3, was correct.

Following the EELS based work by Froitzheim *et al.* and Steininger *et al.* a RAIRS study was carried out by Hayden and Bradshaw to further investigate the bridging C-O stretch [13]. They carried out a series of coverage dependant RAIRS experiments covering adsorption temperatures of 95 to 300 K. The increased resolution of RAIRS over EELS allowed them to see two distinct peaks (1810 cm^{-1} and 1850 cm^{-1}) in the bridging region at adsorption temperatures of 150 to 250 K. These peaks were assigned to the C-O stretch of CO adsorbed in both two-fold (1850 cm^{-1}) and three-fold sites (1810 cm^{-1}) (see Figure 4.1). A set of infrared emission studies by Tobin and Richards [14] failed to detect a band at 1810 cm^{-1}, only observing one band in the bridging region at 1850 cm^{-1}. This set of mid-infrared emission data was consistent with previous EELS data [11, 12], suggesting that the surface meshes shown in Figure 4.3 are correct, and that there is no CO adsorption in three-fold adsorption sites.

Even more importantly, the work by Tobin and Richards [14] also included the first recorded infrared spectra of the Pt-C stretch for CO adsorbed on a Pt(111) single crystal. Several sets of experiments were carried out using both ^{12}CO and ^{13}CO varying both the coverage of CO and the adsorption temperature. The set of infrared emission spectra of ^{13}CO adsorbed on Pt(111) as a function of coverage (from 0.07 L to 0.5 L) showed only one band in the reported range of 400 cm^{-1} to 500 cm^{-1}, which was centred at 453 cm^{-1} and assigned to the Pt-C stretch of ^{13}CO adsorbed in an atop site. The adsorption temperature experiment probing the adsorption of ^{12}CO on Pt(111) also only showed one band, this time at 467 cm^{-1}, which was assigned to the Pt-C strtetch of ^{12}CO adsorbed in an atop site. These results gave good agreement with the LEED and EELS data recorded by

Steininger et al. [12], as both give the peak position of the Pt-C stretch of ^{12}CO adsorbed linearly on Pt(111) to be around 470 cm^{-1}. In Steininger's work it was shown that, as the coverage increased, CO started to adsorb in bridging sites as well as atop, giving rise to an additional feature in the spectrum at 380 cm^{-1} due to the Pt-CO_{bridge} stretch. Although Tobin and Richards performed a similar high coverage experiment using ^{13}CO, the range of the data presented did not go low enough in energy to determine whether this Pt-CO_{bridge} stretch can be detected by the infrared emission studies reported in their paper [14].

The first detection of the Pt-C stretch using RAIRS was by Hoge et al.[15]. They detected a single peak at 476 cm-1 for a low coverage of CO, which moved to 467 cm-1 when the coverage reached 0.5. Both of these peaks were assigned to the Pt-C stretch of atop-bonded CO. In the experiments where the coverage was 0.5 CO no bridge-bonded Pt-CO stretch was observed, despite its presence in EELS [11, 12] and the presence of the bridge-bonded C-O stretch in mid-IR experiments [13, 14].

Malik and Trenary provided another RAIRS investigation of the Pt-CO stretch of the Pt(111)-CO system [16]. Their experiment employed a commercial FT-IR spectrometer with a conventional infrared source. Each spectrum presented by Malik and Trenary was obtained by scanning for over two hours. They present a series of spectra showing the C-O_{atop} stretch, C-O_{bridge} stretch and the Pt-C_{atop} stretch as a function of coverage. The spectra show that the intensity of the Pt-C_{atop} peak is at a maximum at a coverage of $\theta = 0.2$, the same coverage at which the C-O_{bridge} stretch beings to appear in the mid infrared. As the coverage of CO is increased from 0.2, the C-O_{bridge} stretch increases in intensity whilst the Pt-C_{atop} stretch decreases in intensity and becomes broader. This confirms the theory that CO undergoes a uniaxial compression in the [110] direction, as shown in Figure 4.2, which forces certain CO molecules previously in atop sites to occupy bridge sites. Malik and Trenary were unable to probe the Pt-C_{bridge} stretching region (around 380 cm^{-1} using EELS [12]) because they were using a KBr beamsplitter,

which does not transmit below 400 cm^{-1}. This meant that the Pt-C_{bridge} stretch was still to be detected by RAIRS.

In a remarkable series of experiments, Engström and Ryberg, using a conventional thermal infrared source and a sampling time of three days, detected the Pt-CO stretch for CO adsorbed in both linear and bridge sites in a c(4 × 2) arrangement on Pt(111), which is formed at half monolayer coverage [17, 18]. They report spectra from the four isotopomers $^{12}C^{16}O$, $^{12}C^{18}O$, $^{13}C^{16}O$ and $^{13}C^{18}O$ at 100 K, shown in Figure 4.4 [17].

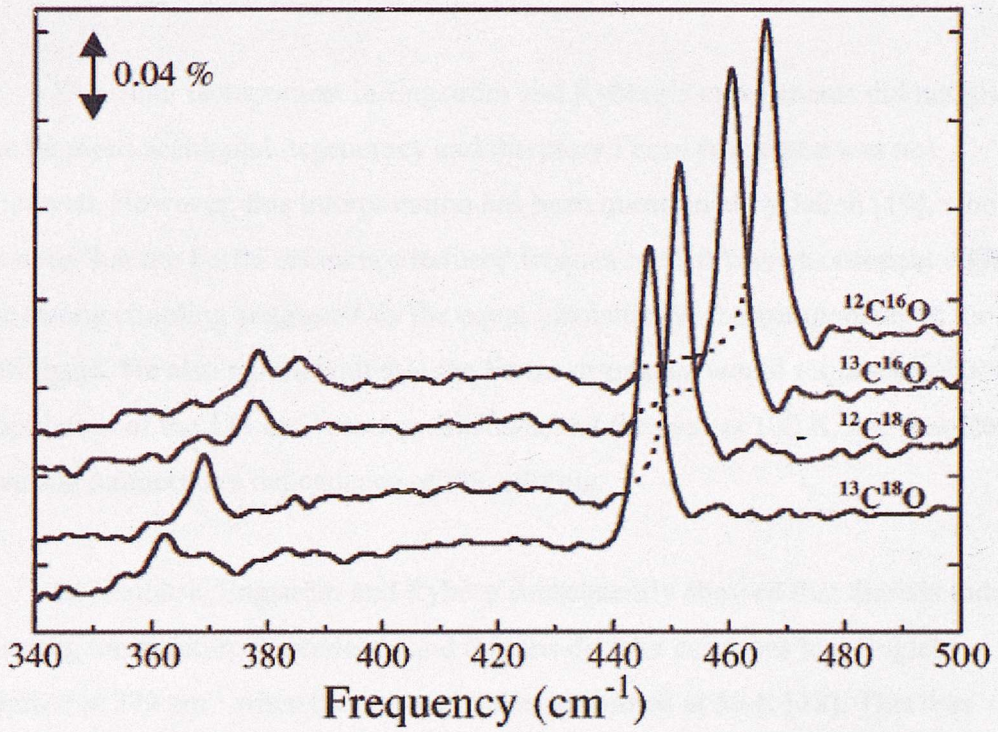

Figure 4.4 – Infrared spectra for four isotopes of CO on Pt(111) in the c(4 × 2) structure at 100 K, recorded by Engström and Ryberg, taken from [17].

The atop-bonded $^{12}C^{16}O$ gave a single peak at 466 cm^{-1}. The bridge-bonded $^{12}C^{16}O$ gave rise to a doublet feature (378 and 385 cm^{-1}), which they assigned to a Fermi resonance between the bridge-bonded Pt-$^{12}C^{16}O$ stretch and the

combination band consisting of a frustrated translation at 510 cm^{-1} and a frustrated translation at 133 cm^{-1}, since 510cm^{-1} – 133 cm^{-1} is close to 385 cm^{-1}. A Fermi resonance occurs in a polyatomic molecule when two vibrational levels belonging to different vibrational modes (or combinations of vibrations) have nearly the same energy. This accidental degeneracy leads to a perturbation of the energy levels where the levels "repel" each other. Therefore, one of the levels is shifted up and the other shifted down so that the separation of the two levels is larger than expected. In infrared spectroscopy this leads to the possibility of seeing two bands close together in energy where only one would be expected. The closer the energy levels are in energy before interaction leads to a larger amount of shifting of the energy levels.

The other isotopomers in Engström and Ryberg's experiments did not give the required accidental degeneracy and therefore Fermi resonance was not observed. However, this interpretation has been questioned by Jakob [19], who showed that the Fermi resonance induced frequency shift was inconsistent with the strong coupling suggested by the equal intensities in the components of the split band. He also pointed out that the Fermi resonance would require significant population of the 133 cm^{-1} mode, which was not the case at 100 K, and predicted a strong temperature dependence of the splitting.

In response, Engström and Ryberg subsequently showed that there is indeed a strong temperature dependence and that the doublet collapses to a singlet centred at 379 cm^{-1} when the experiment is performed at 50 K [18]. This was taken as confirmation of the Fermi resonance at 100 K. However, in their more refined model they suggested that the Fermi resonance involved the difference of the frustrated rotation of atop bonded CO, υ_4, and a frustrated translation of bridge bonded CO, υ_6. Inelastic helium scattering measurements by Graham [20] locate υ_6 at 64 cm^{-1}, and a DFT calculation by Hassel [21] gives 423 cm^{-1} for υ_4. The involvement of modes lower than 133 cm^{-1} appeared to address Jakob's objection to the thermal population of these modes at 100 K.

In this chapter RAIR spectra obtained for the Pt(111)-$^{12}C^{16}O$ system at 260 K are reported, which conflict with this new Engström and Ryberg model. These spectra were recorded using synchrotron radiation as the light source, as opposed to a conventional thermal infrared source as used by Engström and Ryberg. Since the brightness of a synchrotron source is about one thousand times greater than that of a thermal infrared source in the far-infrared region, this enabled the RAIR spectra in this chapter to be recorded in a time of 3 minutes each, rather than the 48 hours required for each of Engström and Ryberg's spectra. This substantial improvement in acquisition time by a factor of 1000 means that there is much less time for impurities to settle on the surface and affect the spectra.

4.2 Experimental

The experimental results presented in this chapter were obtained using the UHV chamber at beamline 13.3 at Daresbury laboratory. A diagram of the chamber can be found in Chapter 2 of this thesis, Figure 2.15.

The experiments at Daresbury were carried out in a diffusion pumped UHV chamber (base pressure 1×10^{-10} mbar) equipped for LEED (low energy electron diffraction), XPS (X-ray photoelectron spectroscopy) and RAIRS (reflection absorption infrared spectroscopy). The chamber was also fitted with a QMS (quadrupole mass spectrometer), an ion gun, and TPD (temperature programmed desorption) apparatus.

The Pt{111} crystal (15×5 mm^2) could be heated by electron beam bombardment or radiatively using a well outgassed tungsten filament, and cooled by conduction to a liquid nitrogen reservoir. The crystal was cleaned by roasting in 2×10^{-7} mbar of oxygen at 925 K and annealing *in vacuo* to 1225 K, followed by cycles of 1 keV Ar^+ sputtering with a drain current of 6 μA and annealing to 1225 K. During the sputtering the crystal was translated along its long axis, which

was in the plane perpendicular to the ion beam, to ensure that the whole of the surface was sputtered. The cleanliness of the crystal was confirmed by XPS and LEED.

The RAIR spectra were obtained at 4 cm^{-1} resolution with a custom vacuum interferometer based on the Nicolet impact modulator with a silicon beamsplitter and an Infrared Laboratories liquid helium cooled (4.2 K) silicon bolometer. The light was reflected at about 87°, off-normal, from the crystal surface. Interferograms were recorded in blocks of 256 scans (90 s accumulation time) and normalised to the stored current in the SRS. The apodisation function was triangular with a notch to remove a small sideband caused by interference in the detector itself. The bands in the RAIR spectra were fitted using a Grams-386 [22] curve-fitting routine and assuming Lorenztian peak shapes without deconvoluting the instrument resolution.

After fast heating of the crystal to remove any adsorbed CO, the crystal was rapidly cooled by liquid nitrogen to minimise readsorption, then a countering heating current passed through the filament to maintain a steady temperature of 260 K. This rapid cooling minimised CO adsorption from the background prior to recording a reference spectrum from the clean surface. CO was dosed by back filling the chamber to produce the half monolayer structure, which was confirmed by giving a c(4 × 2) pattern when measured by LEED.

4.3 *Results and Discussion*

4.3.1 Far-Infrared studies of Pt(111)-CO at 260 K

The RAIR spectrum of $^{12}C^{16}O$ adsorbed in an ordered c(4 × 2) structure ($\theta = 0.5$) on the Pt(111) single crystal at 260 K shown in Figure 4.5 is the average of three experimental runs. This spectrum has two key features; a band at 464 cm^{-1} (FWHM = 13 cm^{-1}) attributed to the Pt-CO stretch of CO adsorbed in atop sites, and a band at 376 cm^{-1} (FWHM = 19 cm^{-1}) attributed to the Pt-CO stretch of CO adsorbed in bridged sites, following the assignment of earlier studies [12, 14, 16-18, 21]. The ratio of the integrated intensity of these two peaks is 2:1, atop:bridged. This shows that the absorption factor of atop Pt-CO on Pt(111) is twice that of bridged Pt-CO on Pt(111), since the expected ratio of the integrated intensity would be 1:1 as this is the ratio of CO molecules in the two adsorption sites. The relative intensity of the atop CO band to the bridging CO band is substantially lower than reported by Engström and Ryberg [17], whose spectra have an atop:bridged peak intensity ratio of about 5:1 due to the strong atop features.

The line shape of the band attributed to the linearly adsorbed CO is more symmetric than that reported by Engström and Ryberg [17]. When their data, shown in Figure 4.4, is examined closely the peak is found to be broadened on the low wavenumber side. In addition, a distinct splitting of the 376 cm^{-1} band, as previously reported by Engström and Ryberg at 100 K [17], was not observed in the spectrum shown in Figure 4.5, and the peak was best fitted by a single Lorentzian at 376 cm^{-1}.

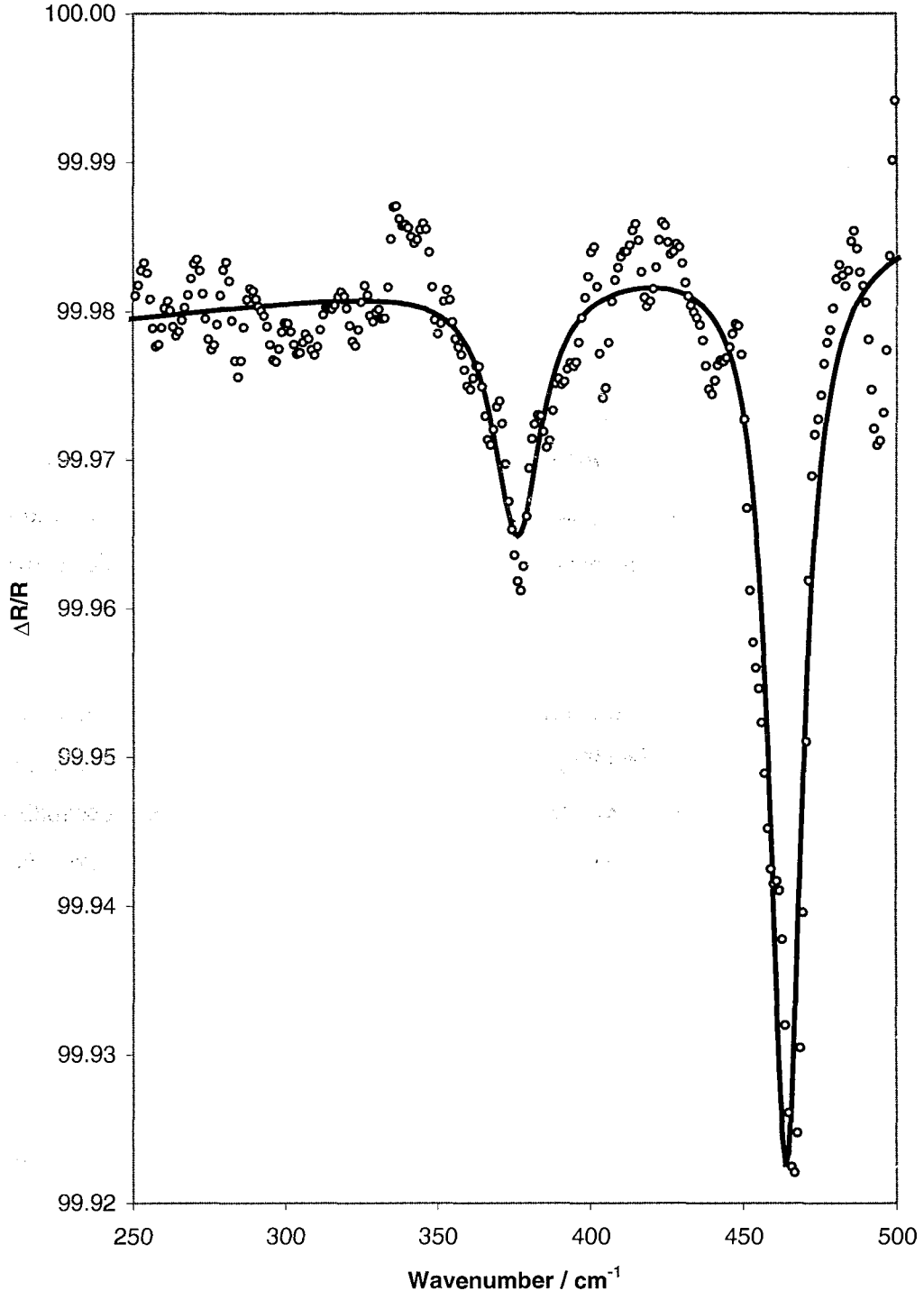

Figure 4.5 – Averaged synchrotron far-infrared RAIR spectrum, with baseline correction, of 0.5 monolayers of CO adsorbed on Pt(111) at 260 K, solid line = fit, circles = data points.

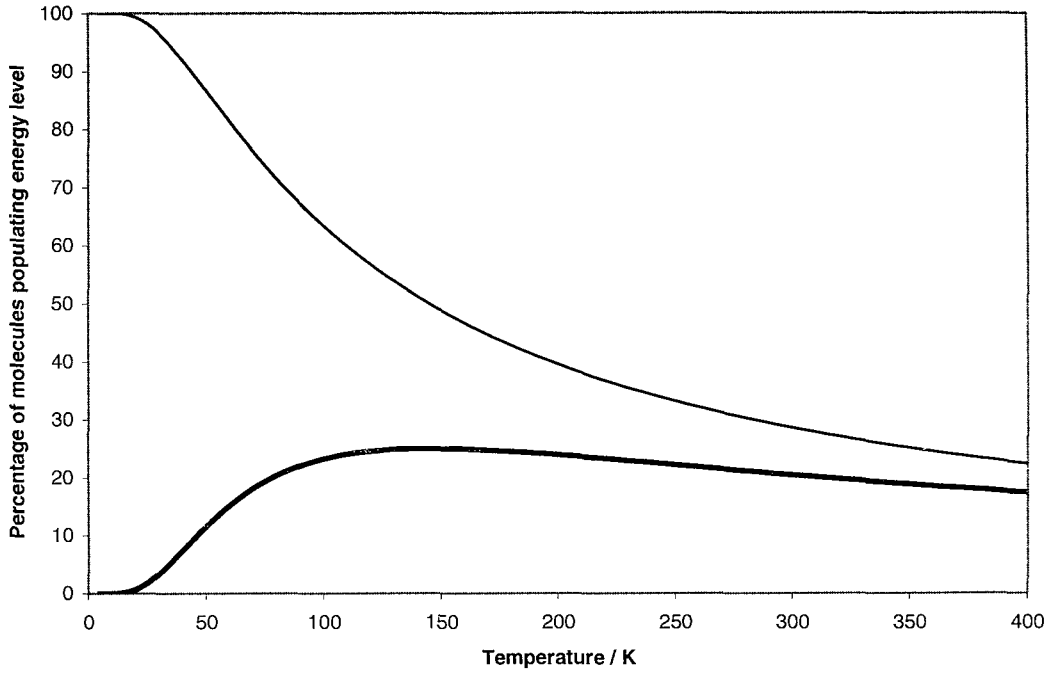

Figure 4.6 – The percentage of CO molecules populating the ground state, p_0 – thin line, and first excited vibrational state, p_1 – thick line, for a mode at 70 cm^{-1}, as a function of temperature, calculated using Equation 4.1.

Since the vibrational energy levels involved in vibrational transitions are low in potential energy, the potential energy curve in this near equilibrium region can be described by a parabola. This means that the vibrational energy levels in this region have a constant separation (using the harmonic approximation), which leads to Equation 4.1 [2] in which the fraction of population, p, for any given vibrational level, v, is be given by,

$$p_v = \left(1 - e^{-\frac{hc\tilde{\nu}}{kT}}\right) e^{-\frac{vhc\tilde{\nu}}{kT}} \qquad \textbf{4.1}$$

where, h is Planck's constant, c is the speed of light in a vacuum, $\tilde{\nu}$ is the vibrational wavenumber, k is Boltzmann's constant and T is the absolute temperature. The percentage of CO molecules populating the ground state, p_0, and

first excited vibrational state, p_1, for a mode at 64 cm^{-1}, as a function of temperature, derived from Equation 4.1, is shown in Figure 4.6.

In their analysis, Engström and Ryberg [18] relied on the frustrated translational mode of bridge bonded CO at 64 cm^{-1} as described in Section 4.1. It can be seen from Figure 4.6 that the probability of occupation of the $v = 1$ level of a mode near 64 cm^{-1} is virtually unchanged on increasing the temperature from 100 to 260 K. Therefore, similar spectra were expected in this work, i.e. the splitting of the bridge bonded peak. However, the split structure seen by Engström and Ryberg at 100 K is not seen in the spectrum presented in Figure 4.5. The full width at half maximum (FWHM) of the bands in Figure 4.5 are larger than the corresponding values in the work by Engström and Ryberg, as expected above an order-disorder transition [23]. However, careful curve-fitting to the data precludes locating bands of similar intensity at 378 and 385 cm^{-1}.

There are further anomalies that arise from the work by Engström and Ryberg. Their experiment at 50 K, which gives a single peak at 379 cm^{-1}, states that 379 cm^{-1} is the unperturbed position of the Pt-CO_{bridge} peak. This has two implications. Firstly, this maintains that the Pt-CO_{bridge} peak for $^{12}C^{16}O$ and $^{13}C^{16}O$ have the same energy, whereas there is a separation of 7 cm^{-1} in their $^{12}C^{18}O$ and $^{13}C^{18}O$ spectra, shown in Figure 4.4. Secondly, since the doublet feature in Figure 4.4 has features at 378 cm^{-1} and 385 cm^{-1}, and the experiment at 50 K gives the Pt-CO_{bridge} peak to be 379 cm^{-1}, using the theory employed in Fermi resonance cases, this gives a value of 384 cm^{-1} for the combination band. However, this is not confirmed by the suggested combination of the frustrated rotation of atop bonded CO (423 cm^{-1} from Hassel [21]) and the frustrated translation of bridge bonded CO (64 cm^{-1} from Graham [20]), which gives a combination band at 359 cm^{-1} (423 cm^{-1} – 64 cm^{-1}), a full 25 cm^{-1} below the required value to obtain a Fermi resonance as described in the experiments by Engström and Ryberg [17, 18]. Also, in the EELS work by Steininger *et al.* [12] * it was suggested that there

* In EELS (e.g. the study of Steininger *et al.*[12]),the intensity of EELS peaks are proportional to $(\Delta E)^{-3}$,where ΔE is the energy gap from the elastic peak.

was an overtone of the frustrated rotation of atop bonded CO at 820 cm^{-1}, giving a value of 410 cm^{-1} for the frustrated rotation. It is interesting that this value was not considered in any of the calculations by Engström and Ryberg [17, 18], particularly because it would lead to a combination band value that is even further away from the required value of 384 cm^{-1}.

It is possible, due to the extensive acquisition time for each spectrum recorded by Engström and Ryberg, that there is some isotopic contamination in their $^{12}C^{16}O$ spectrum. Contamination with $^{13}C^{16}O$ would give a second peak in the bridging region of the $^{12}C^{16}O$ spectrum due to the Pt-$^{13}C^{16}O$ stretch of bridge bonded $^{13}C^{16}O$, and would also account for the broadening of the Pt-CO_{atop} stretch on the low wavenumber side. If isotopic contamination was the cause of the peak at 378 cm^{-1}, rather than a Fermi resonance, then only one peak would be present in this part of the spectrum, as observed in Figure 4.5.

4.4 Conclusions

- The use of synchrotron far-infrared radiation allows the collection of high quality data from the Pt(111) - c(4 × 2) CO system in minutes rather than hours, even under conditions where the metal-adsorbate vibrational bands become broad.

- The Pt-C stretch from atop and bridging $^{12}C^{16}O$ is readily obtained from half monolayer coverage of Pt(111) at 260 K, but no evidence is seen for a Fermi resonance splitting of the metal-adsorbate stretching vibration of the bridge bonded species.

- The results presented in this chapter, therefore, cast some doubt on the origins of the splitting of the peak previously reported by Engström and Ryberg.

4.5 *Further Work*

In order to investigate the temperature dependence of the Pt-CO stretching vibrations, synchrotron far-infrared RAIR spectra need to be taken over a range of temperatures. Spectra covering the range 50 K to 300 K would be the most useful as this covers all the adsorption temperatures investigated by this work and the work by Engström and Ryberg. It is anticipated that this suggested set of experiments would show just two bands in each spectrum, one at about 380 cm^{-1} and one at about 465 cm^{-1}, which could be assigned to the Pt-CO_{bridge} and Pt-CO_{atop} stretching vibrations respectively. If this was the case then no band due to a Fermi resonance would be seen and the theory of the Fermi resonance could be argued to be incorrect.

4.6 *References*

1. D. F. Shriver, P. W. Atkins, and C. H. Langford, Inorganic Chemistry, Second Edition, Oxford University Press, Oxford, (1994).
2. P. W. Atkins, Physical Chemistry, Fifth Edition, Oxford University Press, Oxford, (1994).
3. H. B. Lyon and G. A. Somorjai, J. Chem. Phys. 46 7 (1967) 2539.
4. A. E. Morgan and G. A. Somorjai, J. Chem. Phys. 51 8 (1969) 3309.
5. R. M. Lambert and C. M. Comrie, Surf. Sci. 46 (1974) 61.
6. W. L. Winterbottom, Surf. Sci. 36 (1973) 195.
7. D. M. Collins, J. B. Lee, and W. E. Spicer, Surf. Sci. 55 (1976) 389.
8. R. A. Shigeishi and D. A. King, Surf. Sci. 58 (1976) 379.
9. F. M. Hoffmann and A. M. Bradshaw, J. Catal. 44 (1976) 328.
10. G. Ertl, M. Neumann, and K. M. Streit, Surf. Sci. 64 (1977) 393.
11. H. Froitzheim, H. Hopster, H. Ibach, and S. Lehwald, Appl. Phys. 13 (1977) 147.
12. H. Steininger, S. Lehwald, and H. Ibach, Surf. Sci. 123 2-3 (1982) 264.
13. B. E. Hayden and A. M. Bradshaw, Surf. Sci. 125 3 (1983) 787.

14. R. G. Tobin and P. L. Richards, Surf. Sci. 179 2-3 (1987) 387.
15. D. Hoge, M. Tushaus, E. Schweizer, and A. M. Bradshaw, Chem. Phys. Lett. 151 3 (1988) 230.
16. I. J. Malik and M. Trenary, Surf. Sci. 214 1-2 (1989) L237.
17. U. Engstrom and R. Ryberg, Phys. Rev. Lett. 78 10 (1997) 1944.
18. U. Engstrom and R. Ryberg, J. Chem. Phys. 115 1 (2001) 519.
19. P. Jakob, Phys. Rev. Lett. 79 15 (1997) 2919.
20. A. P. Graham, J. Chem. Phys. 109 21 (1998) 9583.
21. M. Hassel, J. Chem. Phys. 114 1 (2001) 530.
22. Galactic Industries Corporation, Grams-386, (1993).
23. E. Schweizer, B. N. J. Persson, M. Tushaus, D. Hoge, and A. M. Bradshaw, Surf. Sci. 213 1 (1989) 49.

Chapter Five – Studies of Carbon Monoxide Adsorption on Pt(110) [b]

5.1 Introduction

Bulk platinum metal has a face centred cubic structure [1]. When this is cut along the (110) plane, as defined by Miller indices [2], this leads to the (1×1) surface shown in Figure 5.1.

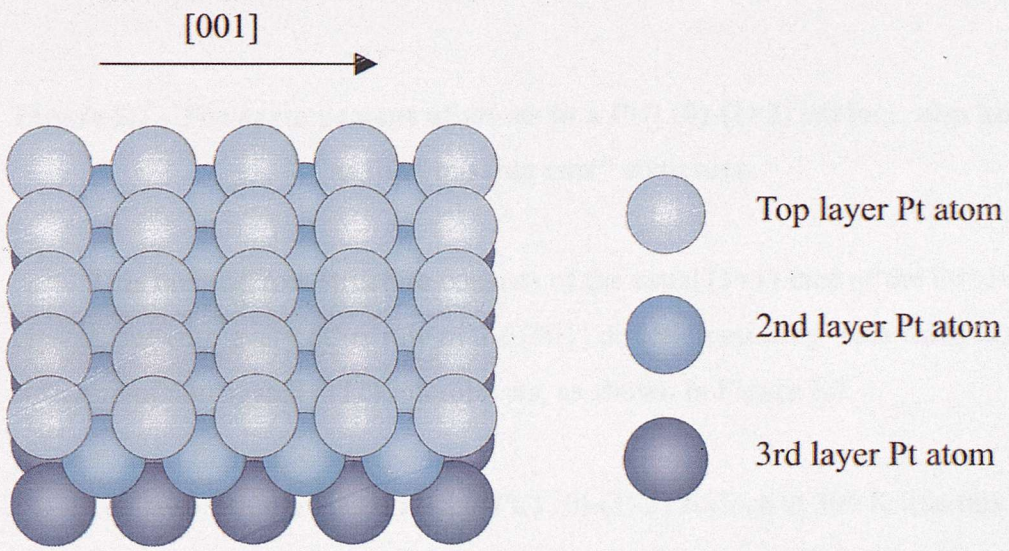

Figure 5.1 –The arrangement of atoms in a Pt(110)-(1×1) surface.

The clean Pt(110)-(1×1) surface has been shown by medium energy ion scattering (MEIS) [3] and low energy electron diffraction (LEED) [4] to reconstruct when placed in UHV to give a (1×2) "missing row" structure, shown in Figure 5.2.

---

b) Portions of this chapter have been previously published.
C.J. Baily, M. Surman, A.E. Russell, Surf. Sci. 523 (2003) 111.

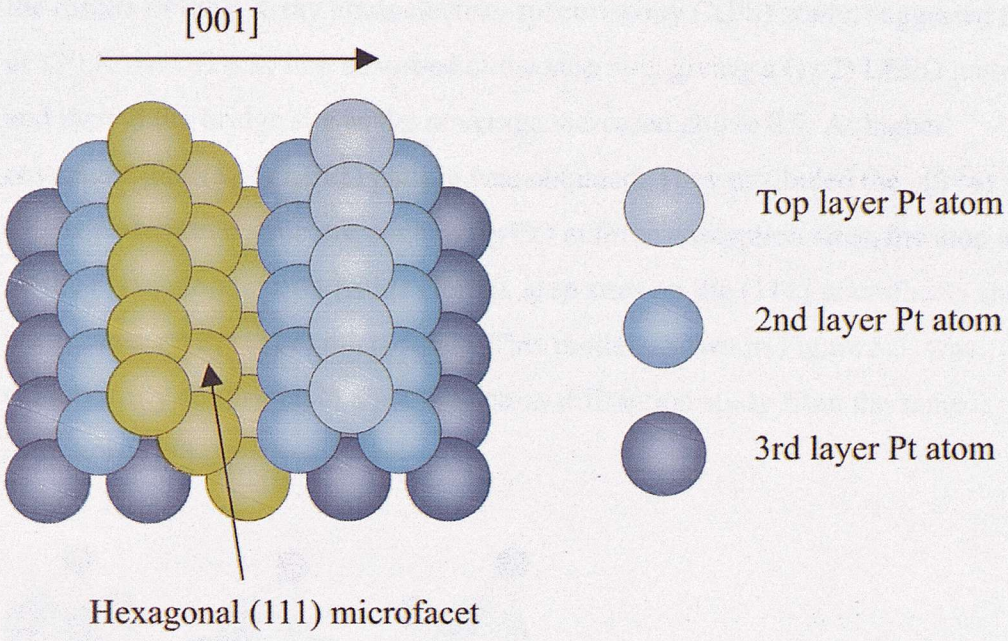

Figure 5.2 –The arrangement of atoms in a Pt(110)-(1×2) surface, also known as the "missing row" structure.

This missing row structure consists of the usual (1×1) face of the Pt(110) crystal, but with every other row in the [001] direction missing. This leads to a structure of corrugated (111) microfacets, as shown in Figure 5.2.

The adsorption of CO onto this Pt(110)-(1×2) surface at 300 K lifts this reconstruction to give the platinum surface a (1×1) structure [3-7]. Scanning tunnelling microscopy (STM) has shown this progressing by homogeneous nucleation of small 1×1 patches [8]. Below 250 K the mobility of surface Pt atoms is reduced and the adsorption of CO does not lift the reconstruction [5, 7].

There have been many studies published regarding the lifting of the (1×2) reconstruction upon the adsorption of CO on Pt(110) [5, 7-10]. The LEED studies of Jackman *et al.* [5, 9] and Ferrer and Bonzel [7] have shown that when CO was adsorbed on Pt(110)-(1×2) below 250 K the LEED pattern changed from (1×2) to *c*(8×4). Upon heating the sample to 325 K, the LEED pattern changed to (1×1) corresponding to that of the lifted reconstruction. Freyer *et al.* [10], interpreting

the results of their X-ray photoelectron spectroscopy (XPS) study, suggested that at 120 K the CO was first adsorbed at the atop site, giving a (1×2) LEED pattern, and then at the bridge site as the coverage increased above 0.5. At higher coverages the *c*(8×4) LEED pattern was obtained. They attributed the *c*(8×4) LEED pattern to a structure containing CO at three adsorption sites; the atop site on the [110] atomic rows (ridge atoms), atop sites on the (111) microfacets and bridge sites on the (111) microfacets. This model, shown in Figure 5.3, was subsequently confirmed in a photoelectron diffraction study from the same laboratory [11].

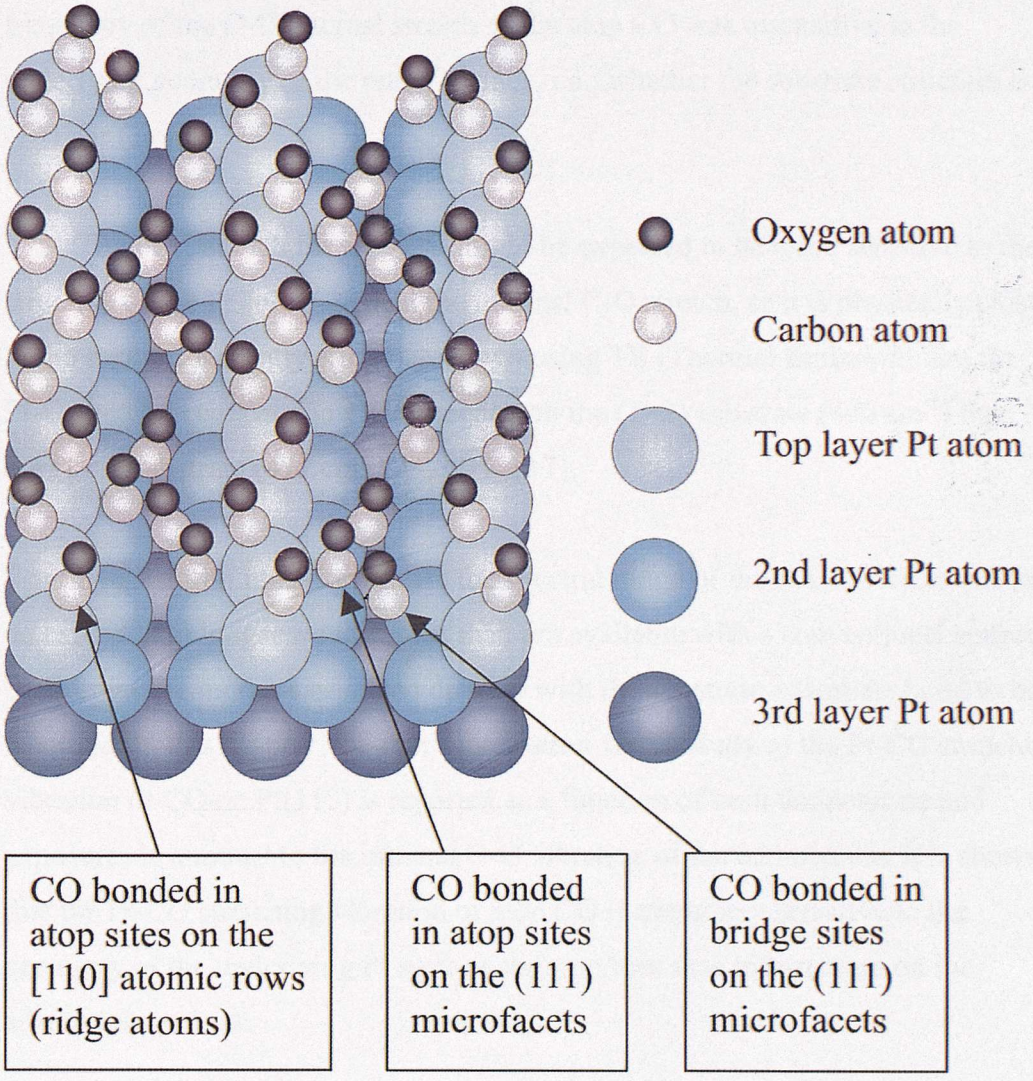

Figure 5.3 – Suggested structure for the c(8×4) LEED pattern observed due to the high coverage chemisorption of CO on Pt(110)-(1×2), from [11].

The adsorption of CO on Pt(110) has also received considerable attention using vibrational spectroscopies, including, HREELS [12-14], RAIRS [12, 15, 16], and SFG [14]. The C-O stretching vibration is sensitive to the type of adsorption site (atop or bridged); bands are observed around 2100 cm^{-1} for atop bonded CO, and at approximately 1850 cm^{-1} for the bridge-bonded species. However, there is some disagreement in the literature regarding the presence of a bridge bonded species on the Pt(110)-(1×2) surface. Hoffman *et al.* [13] found evidence for this species using HREELS at 160 K, whilst Sharma *et al* [16] did not observe bands attributable to the bridge bonded species over the temperature range 90 to 300 K using RAIRS. The RAIRS technique also showed that the frequency of the C-O internal stretch of the atop CO was insensitive to the underlying geometry of the metal surface, i.e., whether the substrate structure is (1×1) or (1×2).

The Pt-C stretch for atop CO might be expected to be more sensitive to the structure of the Pt substrate than the internal C-O stretch, as it is physically closer to the surface. Recently King has shown using TE (Thermal Emission) that the Pt-C stretch occurs at a lower frequency on the (1×2) substrate (466 cm^{-1}) than on the (1×1) substrate (475 cm^{-1}) at 200 K [17].

Synchrotron radiation allows the spectral range of the RAIRS technique to be extended to longer wavelengths than are available with a conventional source and allows the modes associated directly with the substrate-adsorbate bond to be recorded. In this chapter, the first synchrotron far-IR study of the Pt-CO stretching vibration of CO on Pt(110) is reported as a function of both temperature and exposure. In contrast to the internal C-O vibration of the admolecule, it is shown that the Pt-CO stretching vibration of atop CO is extremely sensitive to the geometry of the underlying Pt surface and provides new information on the adsorption process.

5.2 *Experimental*

5.2.1 Ultra High Vacuum Experiments

The experimental results presented in this chapter were obtained using the UHV chamber at beamline 13.3 at Daresbury laboratory. A diagram of the chamber can be found in Chapter 2 of this thesis, Figure 2.15.

The experiments at Daresbury were carried out in a diffusion pumped UHV chamber (base pressure 1×10^{-10} mbar) equipped for LEED (low energy electron diffraction), XPS (X-ray photoelectron spectroscopy) and RAIRS (reflection absorption infrared spectroscopy). The chamber was also fitted with a QMS (quadrupole mass spectrometer), an ion gun, and TPD (temperature programmed desorption) apparatus.

The Pt(110) crystal (15×5 mm^2) could be heated by electron beam bombardment or radiatively using a well outgassed tungsten filament, and cooled by conduction to a liquid nitrogen reservoir. The crystal was cleaned by roasting in 1×10^{-7} mbar of oxygen at 950 K and annealing *in vacuo* to 1225 K, followed by cycles of 1 keV Ar^+ sputtering with a drain current of 6 μA and annealing to 1225 K. During the sputtering the crystal was translated along its long axis, which was in the plane perpendicular to the ion beam, to ensure that the whole of the surface was sputtered. The cleanliness of the crystal was confirmed by XPS and LEED.

The RAIR spectra were obtained at 4 cm^{-1} resolution with a custom vacuum interferometer based on the Nicolet impact modulator with a silicon beamsplitter and an Infrared Laboratories liquid helium cooled (4.2 K) silicon bolometer. The light was reflected at about 87°, off-normal, from the crystal surface. Interferograms were recorded in blocks of 256 scans (90 s accumulation time) and normalised to the stored current in the SRS. The apodisation function was

triangular with a notch to remove a small sideband caused by interference in the detector itself. The bands in the RAIR spectra were fitted using a Grams-386 [18] curve-fitting routine and assuming Lorenztian peak shapes without deconvoluting the instrument resolution.

After quickly heating the crystal to remove any adsorbed CO, the crystal was rapidly cooled by liquid nitrogen to minimise readsorption, then a countering heating current passed through the filament to maintain a steady temperature. This rapid cooling minimised CO adsorption from the background prior to recording a reference spectrum from the clean surface. CO was dosed by back filling the chamber.

5.2.2 Density Functional Theory Calculations

As previously described in detail in Chapter 3, the theoretical calculations were carried out using the CASTEP computer code [19], which is based on density functional theory using a plane-wave pseudopotential formalism, aided by the CERIUS^2 graphical front-end [20]. The computations were performed using the generalised gradient approximation (GGA) using ultra-soft pseudopotentials. The influence of different k-point sampling and plane-wave energy cut-offs was explored in a series of test calculations, and this led to the calculations for the structures obtained by CO adsorption on bridged and atop sites on both the (1x1) and (1x2) surfaces being performed with 60 symmetrically inequivalent k-points and a plane-wave kinetic energy cut-off of 400 eV. In each of the single point energy calculations used to determine the phonon modes of the systems, every atom that was due to be moved from its equilibrium position was moved by 0.01 Å in each of the six spatial directions.

5.3 *Results and Discussion*

5.3.1 Adsorption of CO at 310 K

A LEED pattern of the clean Pt(110)-(1×2) surface, shown in Figure 5.4, was taken before any CO dosing occurred. This shows that the reconstruction of the Pt(110) substrate is intact before exposure to CO. RAIR spectra at increasing exposures for CO adsorption on the Pt(110) surface at 310 K are shown in Figure 5.5. At the initial exposure, 0.05 L, a single peak is observed at 471 cm^{-1}. The position of this peak shifts to higher wavenumbers as the exposure is increased until a value of 480 cm^{-1} is reached upon saturation. The LEED pattern, shown in Figure 5.6, confirmed that the (1x1) substrate structure was present after CO adsorption, i.e. the reconstruction had lifted. No significant change in band intensity or FWHM (8 cm^{-1}) of the peak on increasing exposure was observed. There is no evidence of a second absorption band in the region 200 cm^{-1} to 550 cm^{-1} at any coverage.

The single peak observed is assigned to the Pt-CO stretching vibration of atop CO adsorbed on the ridge Pt atoms. Complementary studies on the Pt(111) surface showed the atop Pt-CO band at 464 cm^{-1}, significantly higher than the bridging species at 376 cm^{-1} [21-23]. The position of the band at 471 cm^{-1} is in good agreement with the EELS data reported by Klünker *et al.* [14] in which the metal-CO vibration for CO on Pt(110) at 300 K was found at 472 cm^{-1}. The shift in frequency with increasing coverage may reflect either completion of the CO-induced lifting of the reconstruction or the influence of dipole coupling as the coverage increases. The CO molecules adsorbed on the atop sites of the ridge atoms along the [110] axis are tilted [11, 16]. Strong mutual depolarization within this adlayer readily explains the fact that the band intensity does not increase with coverage. There is no evidence of CO occupying bridged sites in agreement with the mid-IR studies of Sharma *et al.* [16].

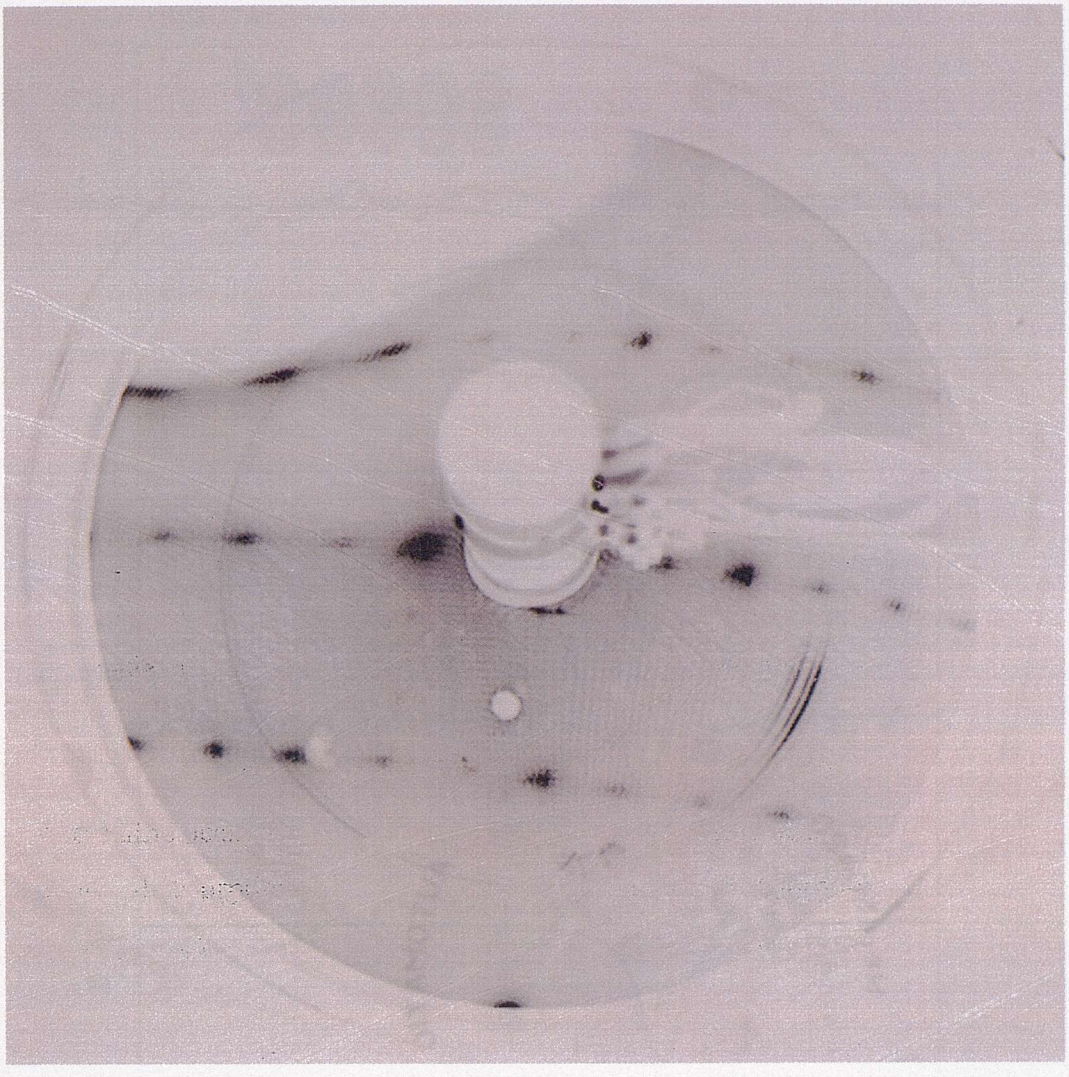

Figure 5.4 – LEED pattern obtained before the room temperature adsorption of CO on a Pt(110) surface. The (1×2) pattern indicates that the structure of the Pt(110)-(1×2) substrate is still intact. Note that this figure shows the "negative" of the recorded LEED pattern.

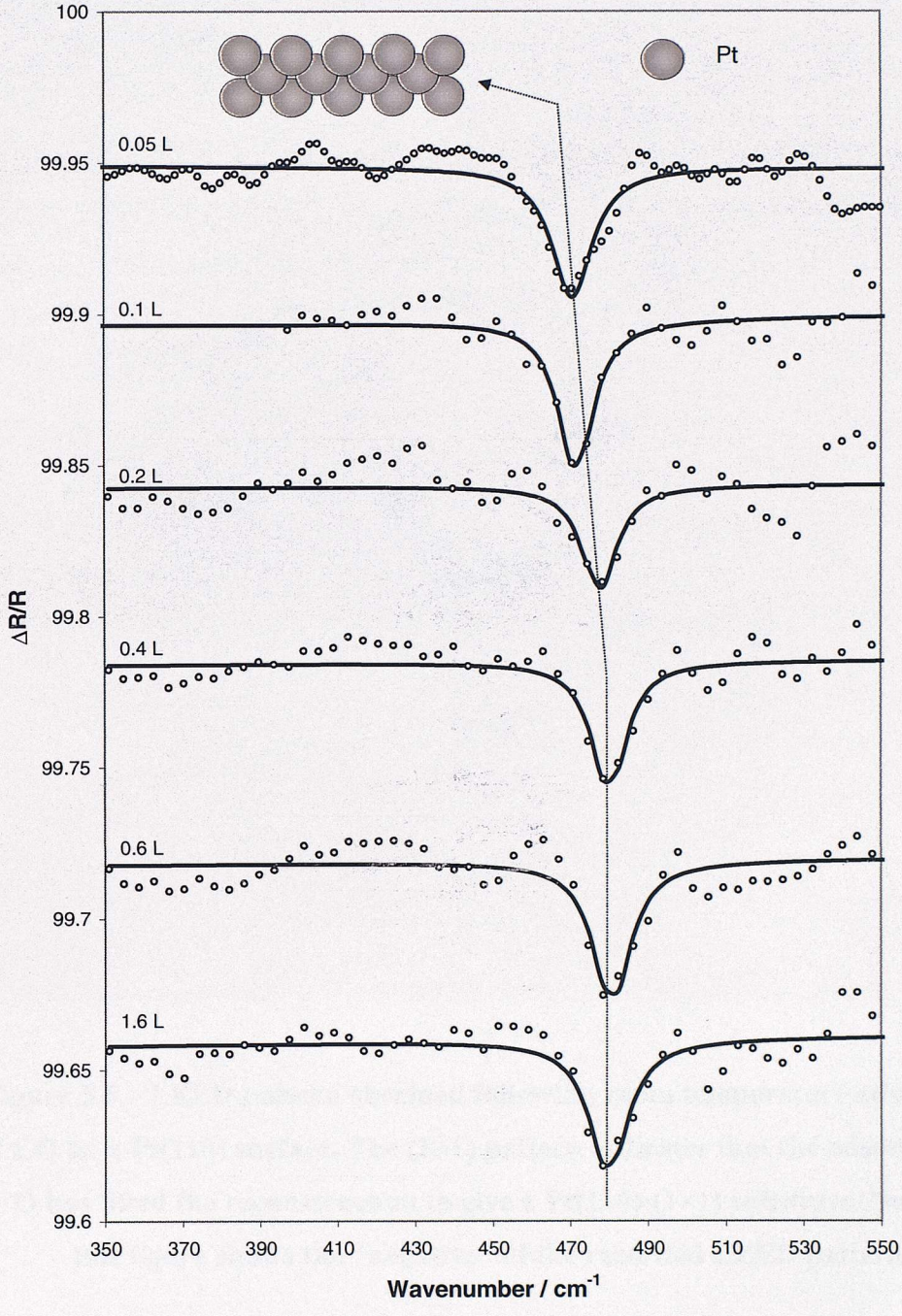

Figure 5.5 - RAIR spectra, obtained at 8 cm^{-1} resolution, showing the adsorption of CO on the Pt(110) surface at 310 K at increasing exposures [*]. The spectra have been offset vertically for clarity. Data points are shown as open circles and the Lorentzian fits as solid lines.

[*] As there is no increase in peak intensity as the CO exposure increases, the values of exposure quoted in Figure 5.5 are significantly lower than the true exposures.

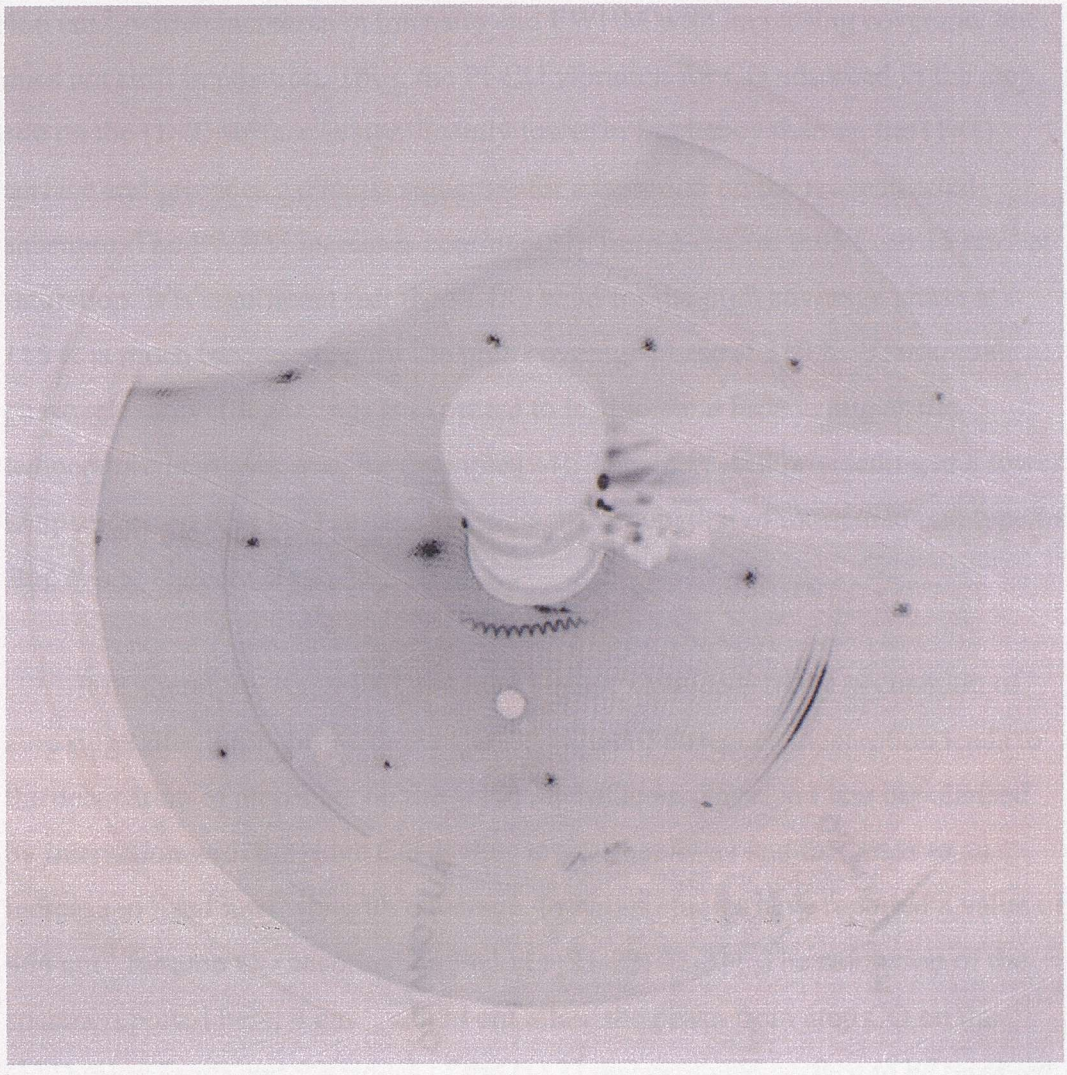

Figure 5.6 – LEED pattern obtained following room temperature adsorption of CO on a Pt(110) surface. The (1×1) pattern indicates that the adsorption of CO has lifted the reconstruction to give a Pt(110)-(1×1) substrate. Note that this figure shows the "negative" of the recorded LEED pattern.

5.3.2 Adsorption of CO at 115 K

RAIR spectra recorded as a function of exposure of the (1×2) surface at 115 K are presented in Figure 5.7. LEED recorded after the infrared measurements gave a similar pattern to that shown in Figure 5.4, and so confirmed the retention of the (1×2) reconstruction. A single band develops at

466 cm^{-1}, which increases in intensity and FWHM with increasing coverage, but does not shift in position. Thus, the Pt-CO vibration for CO adsorbed in the atop site on the (1×2) surface is significantly lower in frequency than on the (1×1) surface and provides a distinct signature for adsorption on the reconstructed substrate. The FWHM increases continuously from 6 cm^{-1} at 0.05 L, to 15 cm^{-1} at saturation. It is significant that the Pt-CO band for the high coverage phase at 115 K is much broader than for the high coverage phase at 310 K. Vibrational phase relaxation (dephasing) is expected to lead to band broadening as the temperature increases, see, for example [24]. This increased broadening at a lower temperature on the (1×2) surface suggests the occupation of more than one type of atop site at high coverage.

It is, therefore, suggested that initial adsorption leads to the occupation of atop ridge sites, probably with the CO axis tilted. Subsequent adsorption leads to the occupation of atop sites on the (111) microfacets. These are less depolarised by interaction with the ridge CO as they are further away and this leads to an increase in band intensity with coverage. Previous studies have reported a value of 464 cm^{-1} for atop CO adsorbed on Pt(111) [21-23, 25-31]. The resolution of the spectra reported here, 4 cm^{-1}, would not allow the peaks from atop CO on the (111) microfacets and the ridges of the (1×2) reconstructed surface to be resolved; 464 cm^{-1} and 466 cm^{-1}, respectively.

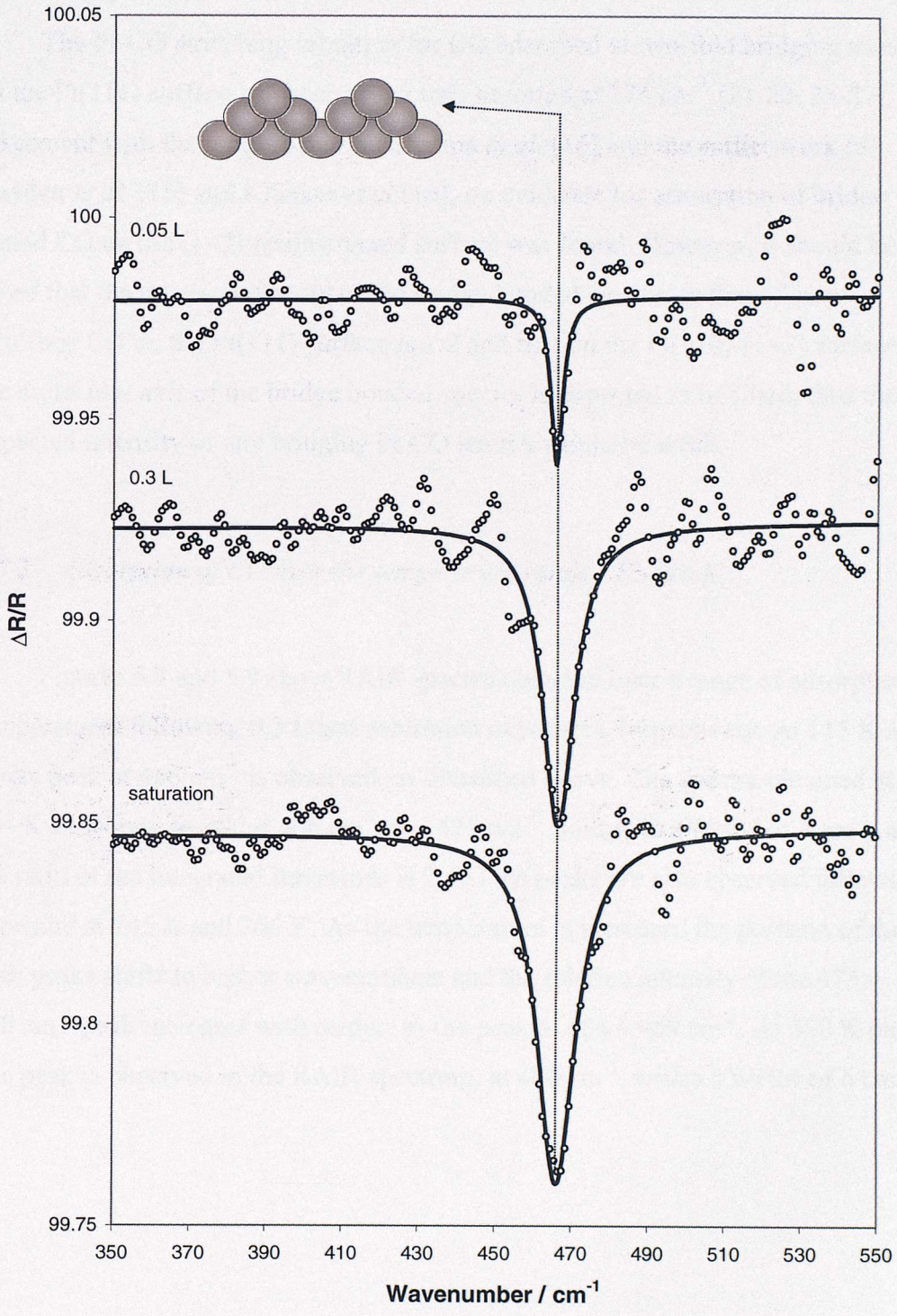

Figure 5.7 - RAIR spectra, obtained at 4 cm^{-1} resolution, following increasing exposure to CO on the Pt(110)-(1×2) surface at 115 K. The spectra have been offset vertically for clarity. Data points are shown as open circles and the Lorentzian fits as solid lines.

The Pt-CO stretching vibration for CO adsorbed at two-fold bridging sites on the Pt(111) surface has been previously reported at 376 cm^{-1} [21-23, 25-27]. In agreement with the recent paper by Sharma *et al.* [16] and the earlier work of Hayden *et al.* [15] and Klünker *et al* [14], no evidence for adsorption of bridge bound CO on the (1×2) reconstructed surface was found. However, it should be noted that the relative intensity of the bridge bonded species to that of atop adsorbed CO on the Pt(111) surface is 1:2 and that on the Pt(110)-(1×2) surface the molecular axis of the bridge bonded species is expected to be tilted, thus the expected intensity of any bridging Pt-CO stretch would be weak.

5.3.3 Adsorption of CO over the temperature range 115-310 K

Figures 5.8 and 5.9 show RAIR spectra obtained over a range of adsorption temperatures following 0.3 L and saturation exposures, respectively. At 115 K a single peak at 466 cm^{-1} is observed, as discussed above. The spectra obtained at 204 K show two peaks, at 466 cm^{-1} and 475 cm^{-1}, both with FWHM of 7 cm^{-1}, and the ratio of the integrated intensities is 2:1. Two peaks are also observed following exposure at 245 K and 266 K. As the temperature is increased the position of the both peaks shifts to higher wavenumbers and the relative intensity of the 475 – 478 cm^{-1} peak increases with respect to the peak at 466 – 469 cm^{-1}. At 310 K only one peak is observed in the RAIR spectrum, at 480 cm^{-1}, with a FWHM of 6 cm^{-1}.

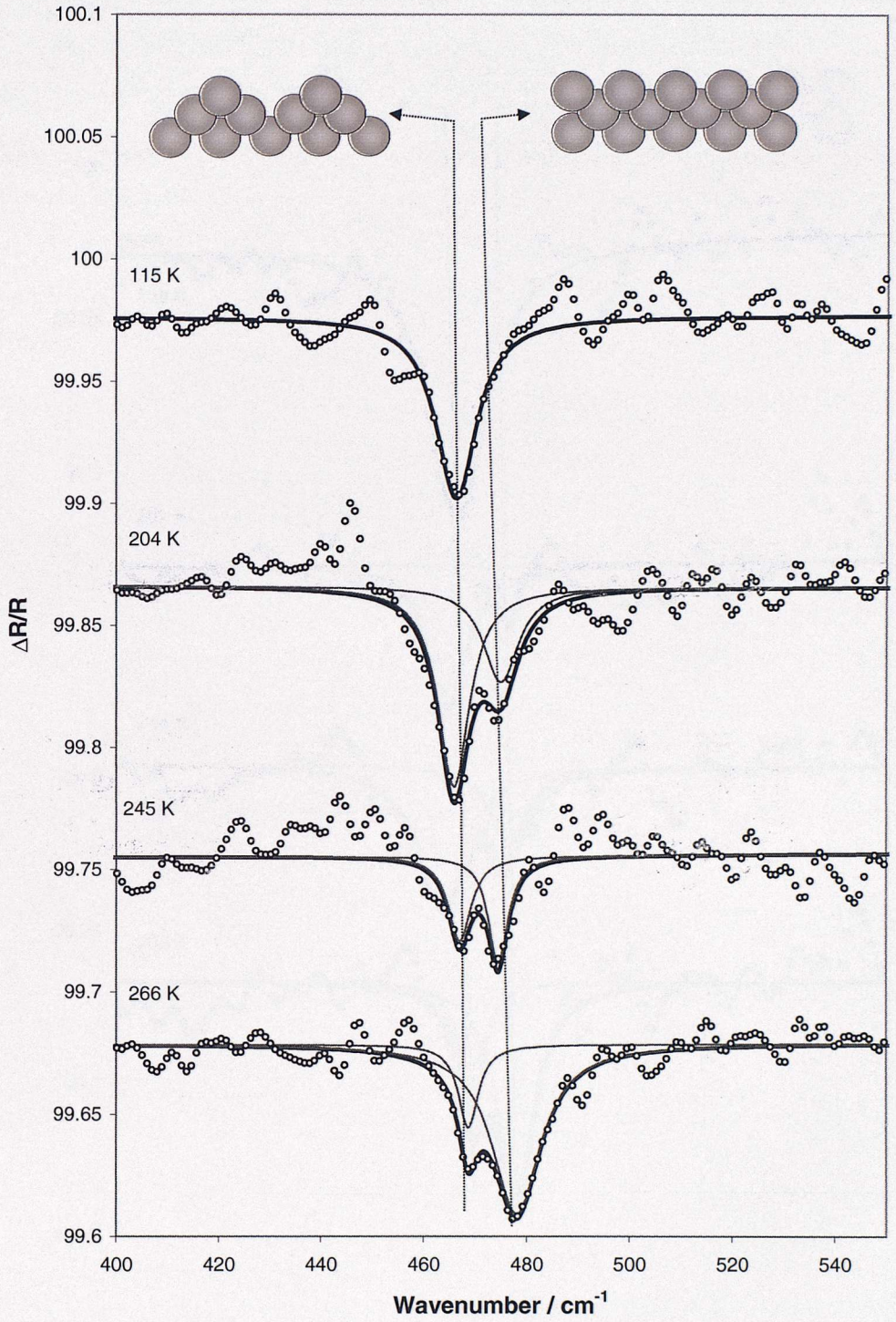

Figure 5.8 - RAIR spectra, obtained at 4 cm^{-1}, following exposure of 0.3 L CO on the Pt(110)-(1×2) surface over the temperature range from 115 K to 266 K. The spectra have been offset vertically for clarity. Data points are shown as open circles and the Lorentzian fits as solid lines.

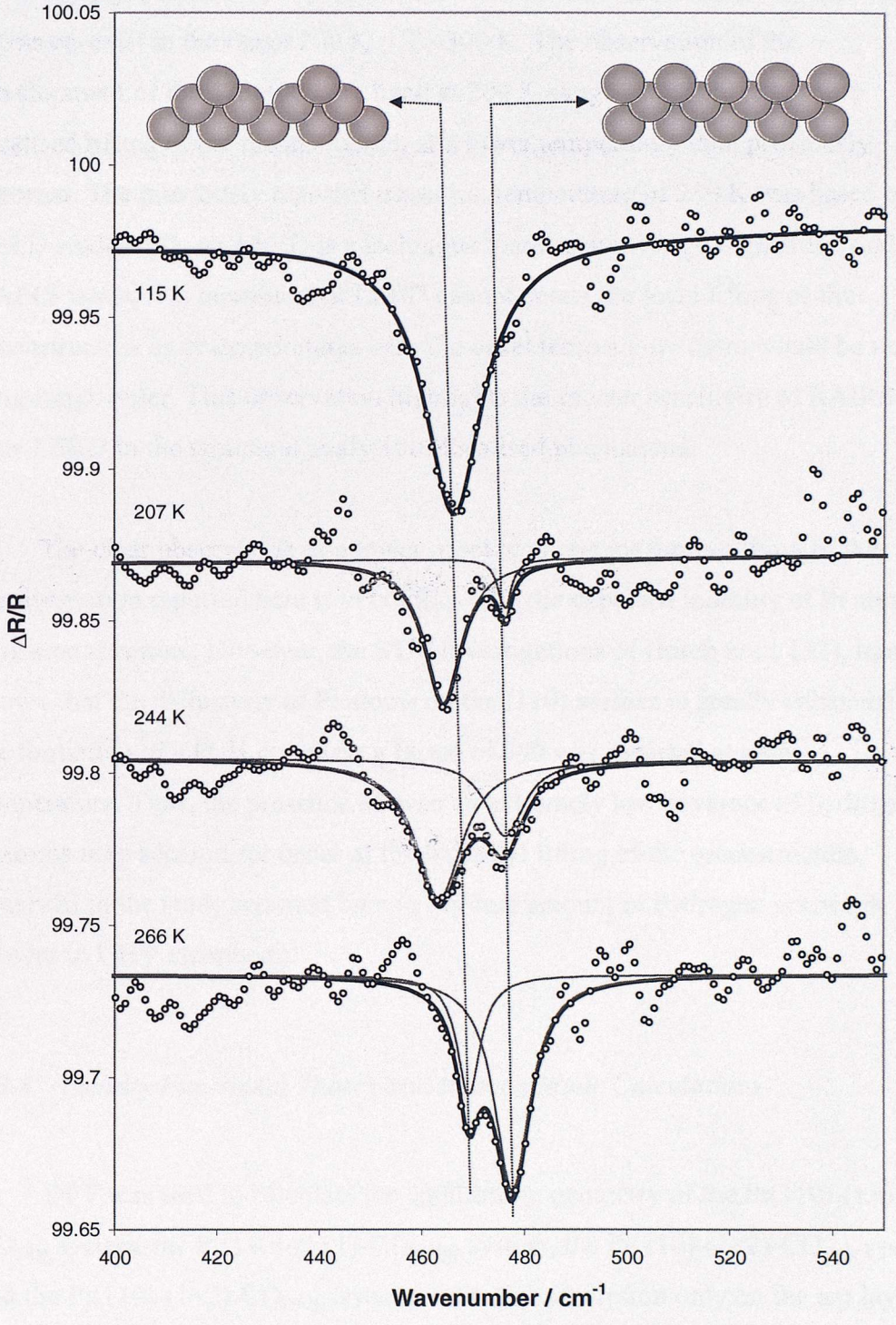

Figure 5.9 - RAIR spectra, obtained at 4 cm^{-1}, following saturation exposure of CO on the Pt(110)-(1×2) surface over the temperature range from 115 K to 266 K. The spectra have been offset vertically for clarity. Data points are shown as open circles and the Lorentzian fits as solid lines.

Clearly, patches of CO adsorbed onto islands of (1×1) and (1×2) substrate atoms co-exist in the range 200 K < T <300 K. The observation of the development of the 475-480 cm^{-1} band at 204 K suggests the onset of some localised lifting of the reconstruction at a lower temperature than previously reported. The previously reported transition temperature of 250 K was based on LEED studies [7]. As LEED is a technique that requires long-range order, and RAIRS is not, it is possible that LEED cannot detect the local lifting of the reconstruction as at temperatures near the onset temperature there would be no long-range order. This observation highlights the greater sensitivity of RAIRS over LEED in the structural analysis of localised phenomena.

The clear observation of a lower onset temperature for the lifting of the reconstruction reported here is in conflict with the expected mobility of Pt atoms at this temperature. However, the STM investigations of Horch *et al.* [32], have shown that the diffusivity of Pt atoms on the (110) surface is greatly enhanced by the formation of a Pt-H complex; a factor of 500 was reported at room temperature. Thus, the presence of even an extremely low coverage of hydrogen adatoms may account for onset of the localized lifting of the reconstruction observed in the study reported here (a residual amount of hydrogen is always present in UHV chambers).

5.3.4 Density Functional Theory and Phonon Mode Calculations

DFT was used to calculate the equilibrium geometry of the Pt(110)-(1×1)-CO_{atop} system, the Pt(110)-(1×1)-CO_{bridge} system, the Pt(110)-(1×2)-CO_{atop} system and the Pt(110)-(1×2)-CO_{bridge} system, with CO adsorption only on the top layer platinum atoms in all cases. These systems are shown more clearly in Figures 5.10, 5.11, 5.12 and 5.13 respectively.

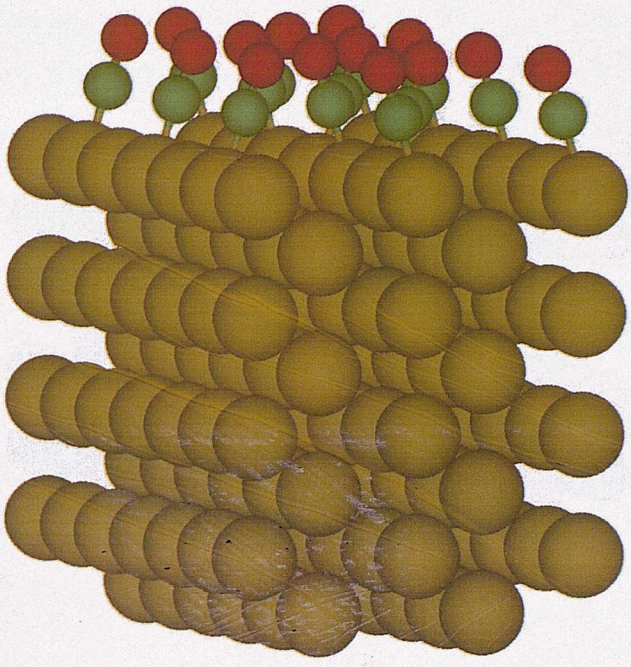

Figure 5.10 – Space filled representation of the equilibrium geometry of the Pt(110)-(1×1)-CO_{atop} system, as determined by DFT calculations.

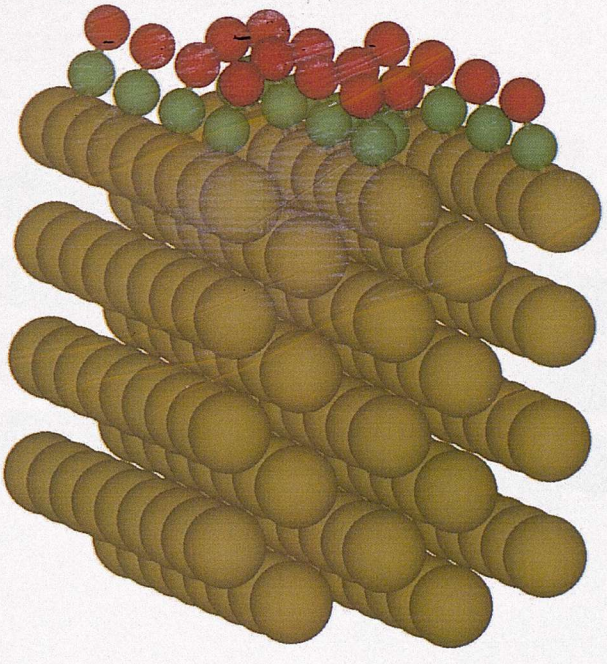

Figure 5.11 – Space filled representation of the equilibrium geometry of the Pt(110)-(1×1)-CO_{bridge} system, as determined by DFT calculations.

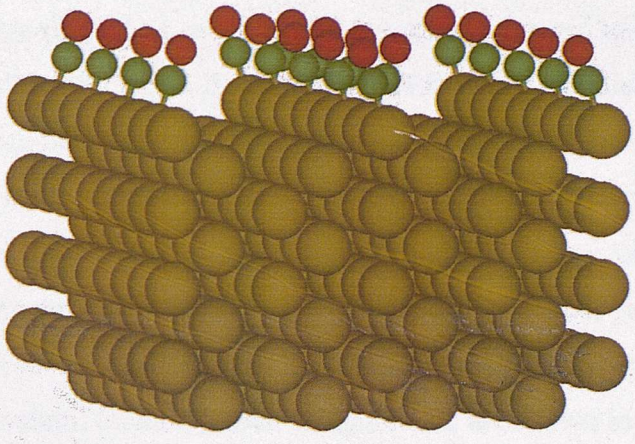

Figure 5.12 – Space filled representation of the equilibrium geometry of the Pt(110)-(1×2)-CO_{atop} system, as determined by DFT calculations.

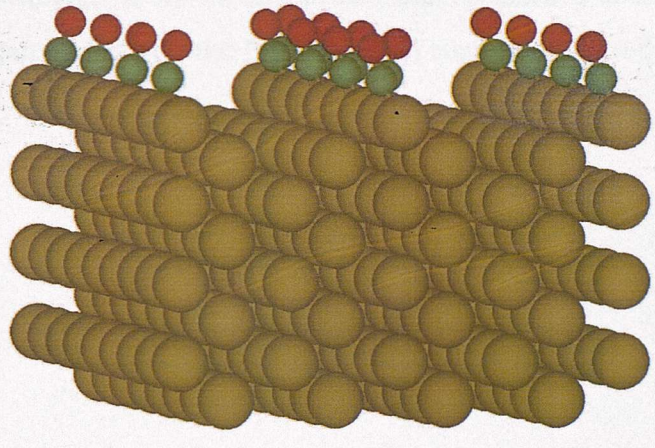

Figure 5.13 – Space filled representation of the equilibrium geometry of the Pt(110)-(1×2)-CO_{bridge} system, as determined by DFT calculations.

Once the equilibrium geometries had been calculated, the force constant matrices were determined. In a similar way to Hassel's work on the Pt(111)-CO system [33], the platinum atoms were fixed in position for the force constant matrix calculations since their relatively large mass, compared to CO, means that in reality they will barely move. The accuracy of Hassel's calculations shows the fixing of the platinum substrate to be a valid approximation. The carbon and oxygen atoms in each of the four cases were moved in turn in each of the six spacial directions, and the energy of each perturbed system was calculated. These energies were then put into a matrix which, when diagonalised, yielded the phonon modes of each system and the associated atomic movements. The phonon modes for each system, including their assignments, are shown in Table 5.1.

Only two of the calculated modes have the possibility of being infrared active, the C-O symmetric stretch and the Pt-CO symmetric stretch. The frustrated rotations are not infrared active because their dipole changes are parallel to the surface, and the antisymmetric stretches are infrared inactive because they create a local quadrupole which gives no net dipole change, and hence no detection by RAIRS. In Table 5.2, the results of the DFT calculations for the Pt-CO symmetric stretches of atop and bridge bonded CO on Pt(110)-(1×1) and Pt(110)-(1×2) substrates are compared to the experimental results presented in this chapter, and a set of cluster calculations on the Pt(110)-(1×1) surface by Curulla *et al.* [34].

	Position of vibrational band / cm^{-1}			
	Atop (1×1)	Atop (1×2)	Bridge (1×1)	Bridge (1×2)
C-O symmetric stretch	2181	2171	2040	2020
C-O antisymmetric stretch	2104	2118	1960	1956
Pt-CO symmetric stretch	470	481	377	382
Pt-CO antisymmetric stretch	463	466	398	372
Pt-CO frustrated rotation	443	431	536	525
Pt-CO frustrated rotation	401	396	404	406
Pt-CO frustrated rotation	379	385	421	425
Pt-CO frustrated rotation	377	354	409	399

Table 5.1 – Calculated vibrational modes and the corresponding energies for CO adsorbed in atop and bridge sites on Pt(110)-(1×1) and Pt(110)-(1×2) surfaces.

	Position of vibrational band / cm^{-1}		
Vibrational Mode	Experiment	DFT calculations	Cluster calculations [34]
Atop (1×1)	478	470	459
Atop (1×2)	470	481	-
Bridge (1×1)	not seen	377	343
Bridge (1×2)	not seen	382	-

Table 5.2 – Comparison of the experimental energies of the Pt-CO symmetric stretches of atop and bridge bonded CO on Pt(110)-(1×1) and Pt(110)-(1×2) with energies calculated using DFT and *ab initio* cluster model calculations.

There are two main observations emanating from the DFT calculations. The first is that the DFT calculations are clearly much more accurate at determining the positions of the Pt-CO modes, than the cluster calculations. This improved accuracy is shown in both the atop and bridge cases on the (1×1) substrate. The improvement in the atop case can be seen by simply comparing the values obtained by both calculation methods to the experimental value of 478 cm^{-1}. Although the bridge case is not seen on the Pt(110) surface, it would be expected to have a value similar to that of bridge-bonded CO on the Pt(111) surface, 376 cm^{-1} [21]. Comparing the value of 377 cm^{-1}, obtained by DFT calculations, with the value of 343 cm^{-1}, from the cluster calculations, again highlights the improved accuracy of the DFT calculations.

There are two major reasons for DFT calculations giving more accurate results than cluster calculations. The first of these is that the limited number of substrate atoms used in cluster calculations leads to a poor description of the band

structure of the metallic substrate. Secondly, DFT allows dipole coupling between the CO molecules to be included in the calculation, due to the summation over the whole of the periodic substrate.

The second observation is that the DFT calculations predict the peak position of CO on the (1×2) substrate to be higher than on the (1×1) substrate, whereas the experimental data clearly shows that the Pt-CO stretch on the (1×1) substrate is higher in energy. This anomaly could be due to the fact that the DFT calculations have an uncertainty and the peak values are only 11 cm^{-1} apart by calculation, and 8 cm^{-1} apart by experiment. If the uncertainty of the calculations was greater than 11 cm^{-1}, then if the value of the uncertainty was subtracted from the calculated value of the Pt(110)-(1×2)-CO_{atop} stretch, and added to the Pt(110)-(1×1)-CO_{atop} stretch, the energy of the Pt(110)-(1×1)-CO_{atop} stretch would become higher than that of the Pt(110)-(1×2)-CO_{atop} stretch. This uncertainty in the DFT calculations could be the reason for the disagreement in the relative peak positions of the Pt-CO_{atop} stretches.

Overall, the calculations show good agreement with experiment in the case of the Pt-CO stretches, since both calculated values are within 11 cm^{-1} of their respective experimental values.

5.4 Conclusions

- The far-infrared RAIRS experiments presented in this chapter have shown that the Pt-CO stretching vibration, unlike the internal CO stretch, of CO adsorbed in atop sites is a sensitive probe of the structure of the underlying Pt(110) surface.
- This signature of the Pt structure has allowed the lifting of the reconstruction to be followed as a function of temperature and, for the first time, allowed detection of localised lifting of the (1×2) reconstruction at a temperature 50 K lower than previously reported.

- The DFT calculations showed good agreement with the experimental values of the Pt-CO stretches. These calculations were also shown to be significantly more accurate than cluster calculations on the same adsorbate-substrate system.

5.5 Further Work

The results in this chapter give a detailed description of the bonding of CO to the Pt(110) substrate over the temperature range 100 - 300 K. The next step for the RAIRS experiments would be to investigate the bonding of CO on platinum surfaces that had been modified by other metals. As suggested by the introduction in Chapter one, ruthenium would be an interesting modifier to study because it leads to a reduction in the CO poisoning of platinum-based catalysts. As ruthenium leads to a reduction in CO poisoning, it would be expected that CO would bind less strongly to the modified surface than the pure platinum surface, and give Pt-CO stretching peaks at lower energy.

If RAIRS experiments on ruthenium-modified platinum surfaces were undertaken, then complementary DFT calculations would be of great use as a predictive tool to aid the assigning of the peaks in the far-infrared spectra. The calculations would be of even more importance in the case of mixed-metal substrates, rather than pure platinum, as there would be a greater number of possible adsorption sites for CO, given the large number of possible arrangements of both types of metal atom on the surface, and in the second layer of the substrate.

5.6 References

1. D. F. Shriver, P. W. Atkins, and C. H. Langford, Inorganic Chemistry, Second Edition, Oxford University Press, Oxford, (1994).

2. P. W. Atkins, Physical Chemistry, Fifth Edition, Oxford University Press, Oxford, (1994).
3. P. Fenter and T. Gustafsson, Phys. Rev. B 38 15 (1988) 10197.
4. P. Fery, W. Moritz, and D. Wolf, Phys. Rev. B 38 11 (1988) 7275.
5. T. E. Jackman, J. A. Davies, D. P. Jackson, W. N. Unertl, and P. R. Norton, Surf. Sci. 120 2 (1982) 389.
6. C. M. Comrie and R. M. Lambert, J. Chem. Soc., Faraday Trans. 72 (1976) 1659.
7. S. Ferrer and H. P. Bonzel, Surf. Sci. 119 2-3 (1982) 234.
8. T. Gritsch, D. Coulman, R. J. Behm, and G. Ertl, Phys. Rev. Lett. 63 10 (1989) 1086.
9. T. E. Jackman, J. A. Davies, D. P. Jackson, P. R. Norton, and W. N. Unertl, 15 5 (1982) L99.
10. N. Freyer, M. Kiskinova, G. Pirug, and H. P. Bonzel, Appl. Phys. A-Mater. Sci. Process. 39 3 (1986) 209.
11. M. Nowicki, A. Emundts, G. Pirug, and H. P. Bonzel, Surf. Sci. 478 3 (2001) 180.
12. S. R. Bare, P. Hofmann, and D. A. King, Surf. Sci. 144 2-3 (1984) 347.
13. P. Hofmann, S. R. Bare, and D. A. King, Phys. Scr. T4 (1983) 118.
14. C. Klunker, M. Balden, S. Lehwald, and W. Daum, Surf. Sci. 360 1-3 (1996) 104.
15. B. E. Hayden, A. W. Robinson, and P. M. Tucker, Surf. Sci. 192 1 (1987) 163.
16. R. K. Sharma, W. A. Brown, and D. A. King, Surf. Sci. 414 1-2 (1998) 68.
17. F. H. Scholes, A. Locatelli, H. Kleine, V. P. Ostanin, and D. A. King, Surf. Sci. 502 (2002) 249.
18. Galactic Industries Corporation, Grams-386, (1993).
19. M. C. Payne, M. P. Teter, D. C. Allan, T. A. Arias, and J. D. Joannopoulos, Rev. Mod. Phys. 64 4 (1992) 1045.
20. Acelrys, CERIUS, (1993).
21. M. Surman, P. L. Hagans, N. E. Wilson, C. J. Baily, and A. E. Russell, Surf. Sci. 511 1-3 (2002) L303.

22. U. Engstrom and R. Ryberg, Phys. Rev. Lett. 78 10 (1997) 1944.
23. U. Engstrom and R. Ryberg, J. Chem. Phys. 112 4 (2000) 1959.
24. E. Schweizer, B. N. J. Persson, M. Tushaus, D. Hoge, and A. M. Bradshaw, Surf. Sci. 213 1 (1989) 49.
25. H. Steininger, S. Lehwald, and H. Ibach, Surf. Sci. 123 2-3 (1982) 264.
26. H. Frotzheim, H. Hopster, H. Ibach, and S. Lehwald, Appl. Phys. 13 (1977) 147.
27. H. Hopster and H. Ibach, Surf. Sci. 77 (1978) 109.
28. D. Hoge, M. Tushaus, E. Schweizer, and A. M. Bradshaw, Chem. Phys. Lett. 151 3 (1988) 230.
29. I. J. Malik and M. Trenary, Surf. Sci. 214 1-2 (1989) L237.
30. R. Ryberg, Phys. Rev. B 40 12 (1989) 8567.
31. R. Ryberg, Phys. Rev. B 44 23 (1991) 13160.
32. S. Horch, H. T. Lorensen, S. Helveg, E. Laegsgaard, I. Stensgaard, K. W. Jacobsen, J. K. Norskov, and F. Besenbacher, Nature 398 6723 (1999) 134.
33. M. Hassel, J. Chem. Phys. 114 1 (2001) 530.
34. D. Curulla, A. Clotet, J. M. Ricart, and F. Illas, J. Phys. Chem. B 103 (1999) 5246.

Chapter Six – Far Infrared Studies of Benzene and Pyridine Adsorption on Pt(110)

6.1 Introduction

Surface reactions of unsaturated hydrocarbons on transition metals are of great interest in catalysis. In the 1970's this interest led to a number of studies being carried out on the adsorption and simple surface reactions of acetylene, ethylene and benzene on well defined nickel and platinum surfaces [1-8].

Unsaturated hydrocarbons may be adsorbed in different ways depending on the reactivity of the surface [9], as shown in Figure 6.1. The first case, A, shows hydrocarbons adsorbed with the C=C bond parallel to the surface by forming a π-donor bond between the C-C π-orbitals and the surface. The second case, B, involves the rehybridisation of carbon 2sp electrons to form σ-bonds between the carbon atoms and the metal surface. The third case, C, specifically concerns benzene adsorption. This suggests that one hydrogen atom is removed from the benzene molecule, allowing a σ –type dissociative bonding through one of the ring carbon atoms, with the plane of the ring inclined at an angle with respect to the surface.

It is known from vibrational spectroscopy of molecules that the state of hybridisation has a direct effect on the structure and, therefore, the vibrational spectrum of the molecule [10]. It follows from this that, by observing the vibrational frequencies of adsorbed molecules and comparing them to gas phase spectra, information about the hybridisation and bonding scheme of the adsorbate should be able to be deduced.

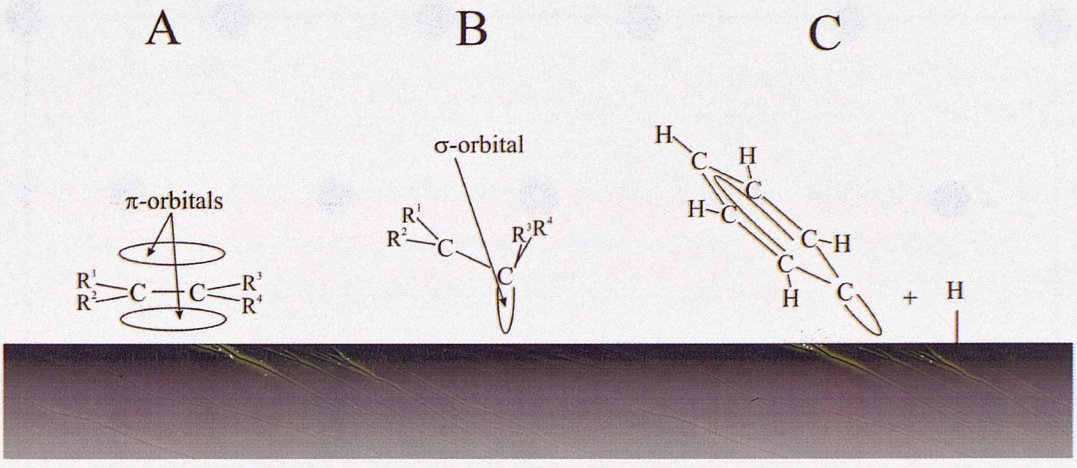

Figure 6.1 – Different adsorption geometries for hydrocarbons on metal surfaces. A = π-bonded, B = σ-bonded, and C = dissociative σ-bonding of benzene.

6.1.1 Benzene adsorption on metal surfaces

For benzene adsorbed on Pt(111) at 300 K, Gland and Somorjai [7] and Stair and Somorjai [8] reported a LEED pattern which was suggestive of three domains of a metastable $\begin{pmatrix} 4 & -2 \\ 0 & 4 \end{pmatrix}$ structure. The LEED pattern is diffuse at low exposures of benzene and reveals sharp reflections only after dosing with about 50 L. For even higher exposures (300 L) the pattern changed to three domains of $\begin{pmatrix} 4 & -2 \\ 0 & 5 \end{pmatrix}$, shown in Figure 6.2. Gland and Somorjai [7] explained the first structure as benzene π-bonded with its ring parallel to the surface, as in case A in Figure 6.1. In the second structure, it was thought that benzene was inclined to the surface, as in case C in Figure 6.1. However, subsequent Auger studies by Stair and Somorjai [8] led them to believe that in both structures benzene is adsorbed with its ring inclined at an angle to the surface. In both room temperature cases, no information concerning whether the carbon atoms were above atop Pt sites, bridge Pt sites, or three-fold hollow Pt sites was able to be deduced from the experiments carried out.

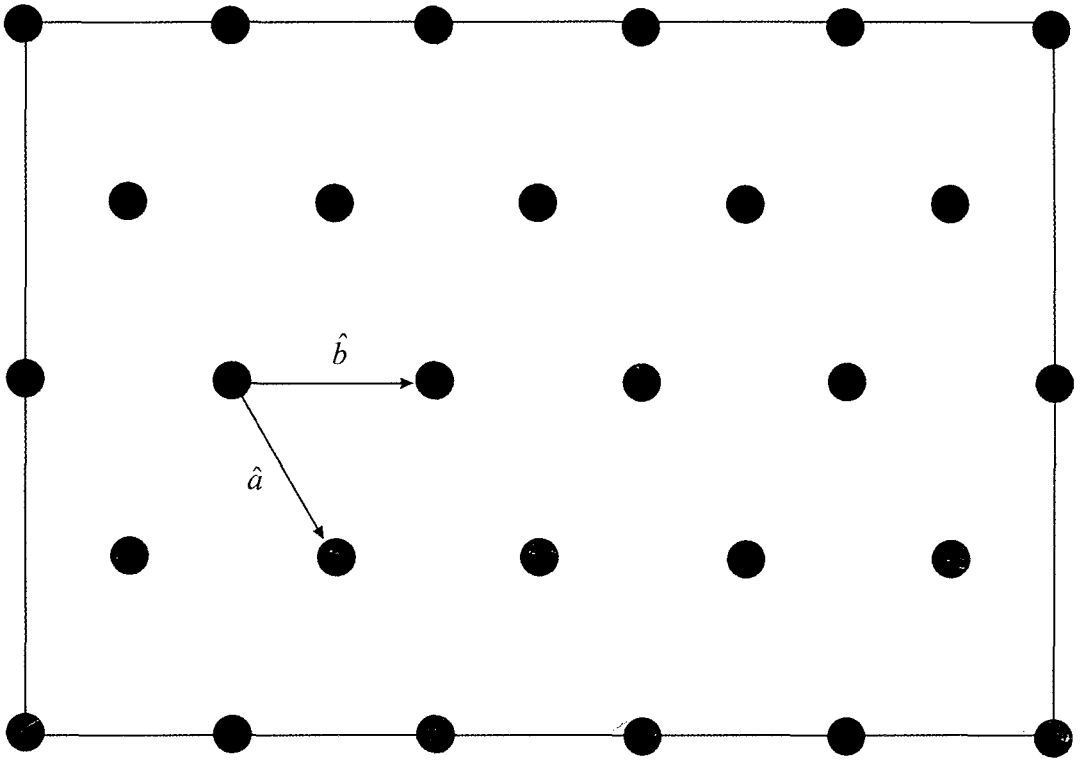

$$\text{Pt(111)-}\begin{vmatrix} 4\hat{a} & -2\hat{b} \\ 0 & 5\hat{b} \end{vmatrix}\text{-benzene}$$

Figure 6.2 –Real space surface structure showing the rectangular domains for very high exposure benzene adsorption on Pt(111) at 300 K, from Gland and Somorjai, and Stair and Somorjai [7, 8].

The first vibrational analysis of up to 10 L of benzene and benzene-d^6 adsorbed on Pt(111) at 140 K to 320 K was carried out by Lehwald *et al.* [11]. Their EELS studies showed that saturation occurs after exposures of 2 to 3 L, and that multilayers of benzene formed after exposures of more than 5 L. The EELS data presented gives six main peaks. By comparison with the spectrum of benzene-d^6, and with the vibrational spectra of liquid hydrocarbons, such as benzene and cyclohexane, Lehwald *et al.* were able to assign each of these peaks, as shown in Table 6.1. By comparing the number and frequencies of the observed losses to possible adsorption models, Lehwald *et al.* deduced that there was no rehybridisation and that benzene adsorbs on Pt(111) predominantly via π–

bonding, with its ring parallel to the surface, as in case A in Figure 6.1. From these studies it was still not possible to obtain information about the bonding site of benzene at the Pt(111) surface.

It should be noted that there are two losses attributed by Lehwald *et al.* [11] to a Pt-C mode, one at 570 cm^{-1} and one at 360 cm^{-1}. It is possible that this could be caused by two different types of mode being present; a translational stretch occurring at 360 cm^{-1}, and a mode due to a rocking of the benzene on the surface, occurring at 570 cm^{-1}.

Observed Peak Position on Pt(111) / cm^{-1}	Approximate Type of Mode	Peak Position in Free Benzene / cm^{-1}
3000	ν_{CH}	3062
1420	δ_{CC}	1310
1130	δ_{CH}	1150
920	ν_{CH}	673
830	ν_{CH}	673
570	ν_{CPt}	-
360	ν_{CPt}	-

Table 6.1 – Assignment of the peaks in the EELS studies of benzene adsorption on Pt(111) by Lehwald *et al.*, from Lehwald *et al* [11].

The picture suggested by Lehwald *et al.* for benzene adsorption on Pt(111) is in agreement with the later electronic energy loss spectroscopy studies by Netzer and Matthew [12]. They do not observe a loss feature at around 7 eV, which is assigned in UV absorption spectroscopy of benzene to a $\pi \rightarrow \pi^*$ transition. Since this transition has a dipole moment in the plane of the benzene molecule, if the molecule is orientated parallel to the surface, as in case A, surface selection rules state that no feature will be seen.

A diffuse LEED study of benzene adsorption on Pt(111) at 170 K carried out by Wander *et al.* [13] showed that, for low coverages of benzene, the benzene molecule adsorbs so that two opposite carbon atoms lie in atop positions, and the other four carbon atoms lie in two-fold bridge sites. This adsorption picture is shown below in Figure 6.3

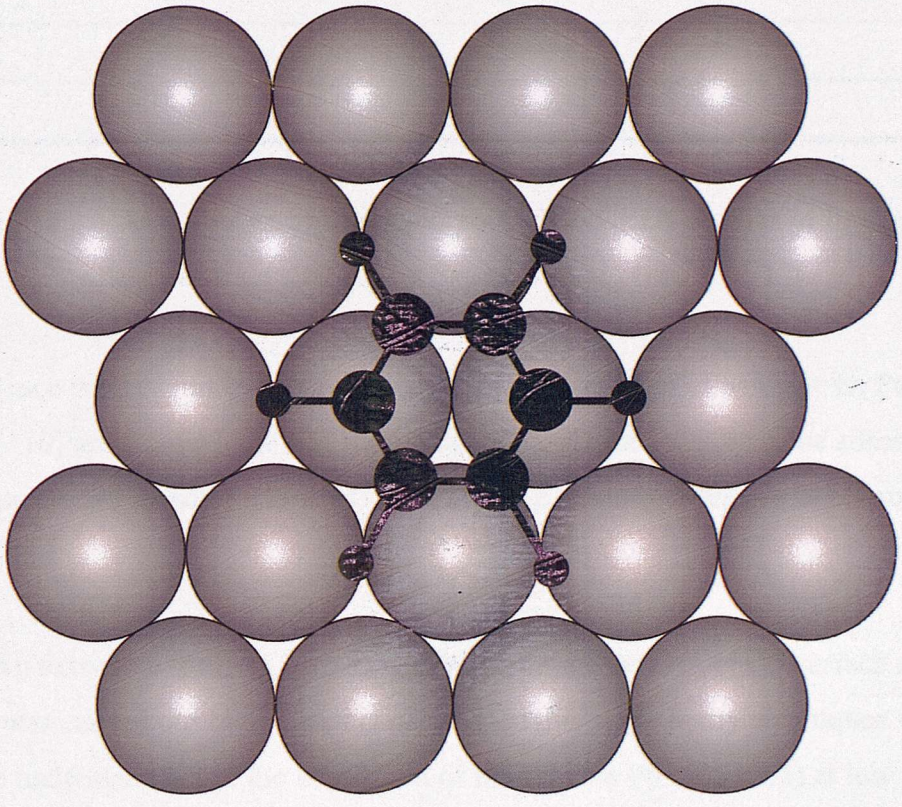

Figure 6.3 – Benzene adsorption geometry for low coverage adsorption of benzene on Pt(111) at 170 K, from Wander *et al.* [13].

The first vibrational study of benzene adsorbed at saturation coverage on the Pt(110)-(1x2) surface was carried out by Surman *et al.* using HREELS to record the vibrational spectra at room temperature [14]. In contrast to the LEED studies of benzene adsorption on Pt(111) [7, 8], LEED studies of benzene adsorption on Pt(110) by Surman *et al.* showed that no ordered overlayer was formed and that the reconstruction of the Pt(110)-(1 × 2) substrate was not lifted. The HREELS studies showed many loss peaks, which are shown in Table 6.2.

Observed Peak Position on Pt(110) / cm^{-1}	Approximate Type of Mode	Peak Position in Free Benzene / cm^{-1}
3025	ν_{CH}	3062
1435	δ_{CC}	1310
1120	δ_{CH}	1150
910	ν_{CH}	673
565	ν_{CPt}	-
340	ν_{CPt}	-

Table 6.2 – Assignment of the peaks in the HREELS studies of benzene adsorption on Pt(110) by Surman *et al.*, from [15-17].

Since the assignments of the peaks for the adsorption of benzene on Pt(111) and Pt(110) are almost identical, Surman *et al.* concluded that benzene adsorbs in the same orientation on Pt(110) as on Pt(111), i.e. parallel to the surface through π -bonding.

An extensive study of benzene adsorbed on the Pt(110)-(1x2) surface at 100 K was carried out by Zebisch *et al.* [18]. In this study many techniques were used to understand better the adsorption of benzene on Pt(110)-(1x2) at low temperature. Their TPD data showed three distinct desorption peaks for deuterated benzene at 185 K, 280 K and 400 K. The peak at 185 K was attributed to physisorbed benzene, whereas the other two peaks were assigned to chemisorbed benzene. This predicts that for any room temperature study of benzene on Pt(110)-(1x2), eg Surman *et al.* [15-17], there will be only one form of chemisorbed benzene present. The LEED data presented by Zebisch *et al.* shows that there is no ordered LEED pattern for saturated adsorption of benzene on Pt(110)-(1x2). Their ARUPS and NEXAFS data suggest that, at low temperature, benzene could adsorb parallel to the (111) microfacets using a similar adsorption geometry to that suggested by Wander *et al.* [13], as shown in Figure 6.4.

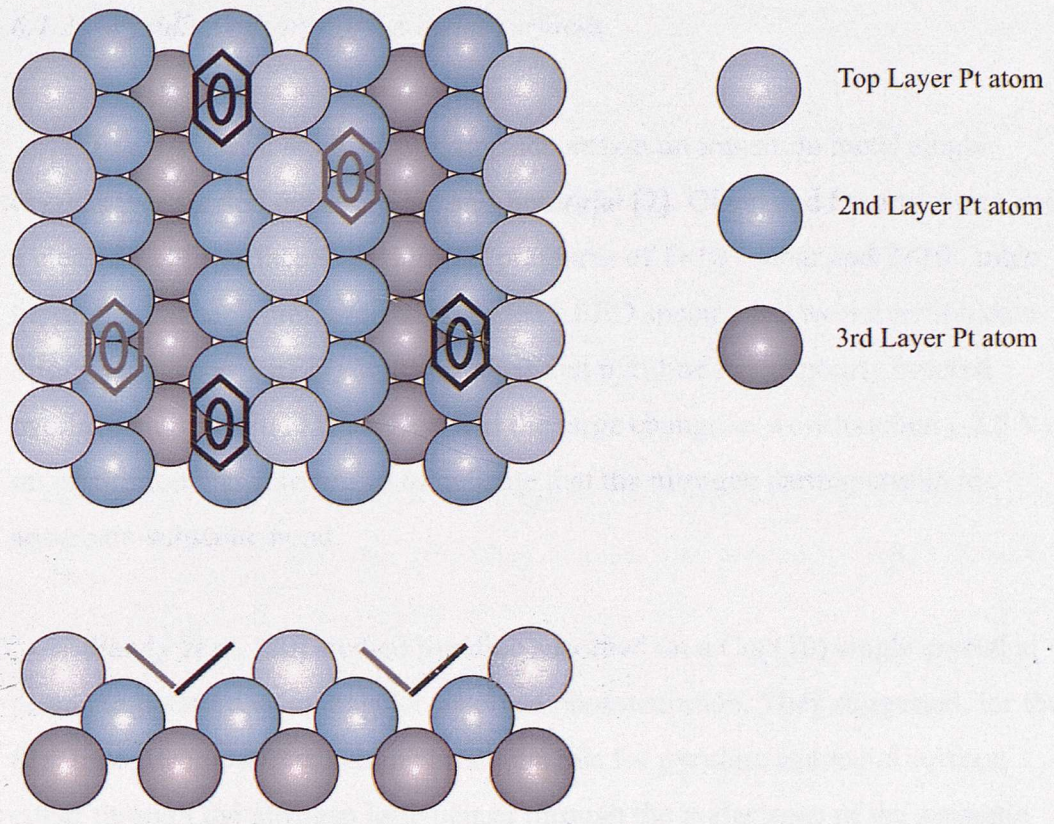

Figure 6.4 – Top view and side view of the adsorption geometry for saturation coverage benzene adsorbed on Pt(110)-(1x2) at 100 K, adapted from Zebisch *et al.* [18].

Thomas *et al.* [19] have also studied benzene adsorption on Pt(110)-(1x2) at low temperature (130 K). Their HREELS spectrum of high coverage benzene adsorption also gave two Pt-C peaks, in similar positions to the work by Surman *et al.* [15-17], though the peak at 340 cm^{-1} was quoted in the table, but not seen in the spectrum. By using a combination of C-H stretching modes and combination modes in HREELS, and UV spectra peaks, two basic bonding models were suggested. The first of these models, at low coverage, is that benzene is distorted upon adsorption forming a 1,3-cyclohexadiene species which coordinates to the surface primarily through two opposite carbon atoms. The second of these models, at high coverage, is that benzene is undistorted on adsorption onto the Pt(110)-(1x2) surface.

6.1.2 Pyridine adsorption on metal surfaces

The first UHV study of pyridine adsorption on transition metal single crystals was carried out by Gland and Somorjai [7]. Gland and Somorjai exposed a clean Pt(111) surface to pyridine at pressures of 1×10^{-8} mbar and 2×10^{-7} mbar for an hour at each pressure and recorded LEED spectra and workfunction data throughout. Their LEED studies showed that pyridine forms poorly ordered overlayers on the Pt(111) surface, and the large change in workfunction (-2.5 V) on adsorption was interpreted to indicate that the nitrogen participates in the adsorbate-substrate bond.

Bandy *et al.* [20] studied pyridine adsorbed on a Cu(110) single crystal at room temperature using angular-resolved photoemission. They suggested, for the first time, two possible bonding arrangements for pyridine at a metal surface; either through the nitrogen lone-pair or through the π-electrons of the aromatic ring. These are shown as model 1 and model 2 respectively in Figure 6.5. In their experiment Bandy *et al.* adsorbed 2 L of pyridine onto a clean Cu(110) surface at room temperature and then recorded their photoemission spectra. They found that the angular behaviour of pyridine was quite different to that of benzene, which strongly suggested that they have different adsorption orientations. Since benzene is known to bond via π-electron bonding [11, 14, 15, 17], as in model 2, it is surmised that pyridine bonds through the nitrogen lone-pair, as in model 1.

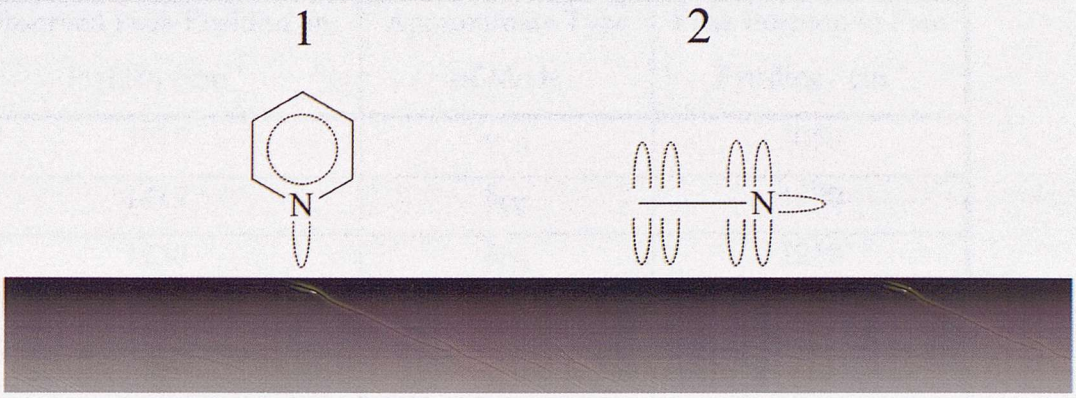

Figure 6.5 – Two possible bonding models for pyridine at a metal surface. Model 1 using the nitrogen lone-pair and model 2 using π-electron bonding, from Bandy *et al.* [20].

The first UHV vibrational study of pyridine adsorption on transition metal surfaces was carried out by Demuth *et al.* [21]. They used EELS and UPS to monitor the adsorption of pyridine on Ag(111) at 140 K as a function of coverage. They showed that, for exposures of less than 0.4 L, pyridine bonds using π-electrons, as in model 2 in Figure 6.5. Once the coverage exceeded 0.5 L the pyridine went through a compressional phase transition where it bonds to the silver surface via the nitrogen lone-pair, as in model 1 in Figure 6.5.

Surman *et al.* report the first UHV vibrational studies of pyridine on the Pt(110) single crystal face [16, 17]. They showed HREELS data for pyridine adsorption at both low exposure (0.2 L) and saturation at 300 K. The assignment for the saturation spectrum is shown in Table 6.3. The spectra are similar in many ways, but the most striking difference is the loss at 820 cm^{-1} which is present only in the low exposure spectrum and is assigned to an out-of-plane CH bend. This mode at 820 cm^{-1} is most dipole active if the molecule is adsorbed parallel to the surface, and is forbidden if the molecule is adsorbed perpendicular to the surface. This interpretation agrees with that of Demuth *et al.* [21] in that it suggests that pyridine also adsorbs on Pt(110) with its ring parallel to the surface at low coverage and at an angle to the surface at high coverage.

Observed Peak Position on Pt(110) / cm^{-1}	Approximate Type of Mode	Peak Position in Free Pyridine / cm^{-1}
3015	ν_{CH}	3050
1415	δ_{CC}	1500
1230	δ_{CH}	1218
1035	δ_{CH}	1070
745	γ_{CH}	730
432	-	385
300	ν_{CPt}	-

Table 6.3 – Assignment of the peaks in the HREELS studies of pyridine adsorption at saturation on Pt(110) by Surman *et al.*, from [17].

The work in this chapter investigates the substrate-adsorbate stretch for both benzene and pyridine adsorbed on Pt(110). Previous studies have been performed using HREELS as the tool for vibrational analysis [14, 15, 17]. In this work synchrotron far-infrared RAIRS is used because of its improved resolution over HREELS to investigate the substrate-adsorbate stretches in more detail, and to give a better idea of the adsorption site of each adsorbate.

6.2 Experimental

The experimental results presented in this chapter were obtained using the UHV chamber at beamline 13.3 at Daresbury laboratory. A diagram of the chamber can be found in Chapter 2 of this thesis, Figure 2.15.

The experiments at Daresbury were carried out in a diffusion pumped UHV chamber (base pressure 1×10^{-10} mbar) equipped for LEED (low energy electron diffraction), XPS (X-ray photoelectron spectroscopy) and RAIRS (reflection absorption infrared spectroscopy). The chamber was also fitted with a QMS

(quadrupole mass spectrometer), an ion gun, and TPD (temperature programmed desorption) apparatus.

The Pt(110) crystal (15×5 mm^2) could be heated by electron beam bombardment or radiatively using a well outgassed tungsten filament, and cooled by conduction to a liquid nitrogen reservoir. The crystal was cleaned by roasting in 2×10^{-7} mbar of oxygen at 925 K and annealing *in vacuo* to 1225 K, followed by cycles of 1 keV Ar^+ sputtering with a drain current of 6 μA and annealing to 1225 K. During the sputtering the crystal was translated along its long axis, which was in the plane perpendicular to the ion beam, to ensure that the whole of the surface was sputtered. The cleanliness of the crystal was confirmed by XPS and LEED.

The RAIR spectra were obtained at 8 cm^{-1} resolution with a custom vacuum interferometer based on the Nicolet impact modulator with a silicon beamsplitter and an Infrared Laboratories liquid helium cooled (4.2 K) silicon bolometer. The light was reflected at about 87°, off-normal, from the crystal surface. Interferograms were recorded in blocks of 256 scans (90 s accumulation time) and normalised to the stored current in the SRS. The apodisation function was triangular with a notch to remove a small sideband caused by interference in the detector itself.

The liquid samples, benzene and pyridine, were placed in separate glass sample tubes, which were attached to the gas line via a KF to mini flange adaptor. Each sample was purified by repeated freeze-pump-thaw cycles to remove dissolved contaminants, in particular air. The samples were dosed by back-filling the chamber, and their purity was checked by mass spectrometry before each experiment.

6.3 *Results and Discussion*

6.3.1 Far-Infrared studies of Pt(110)-benzene at 320 K

After rapidly heating the Pt(110) crystal to 700 °C to remove any adsorbed molecules, in particular CO, the crystal was allowed to cool, during which a series of background noise tests were carried out. As the rate of cooling of the crystal became slower, the noise in the tests also became less. When this noise was consistently below a value of 0.015 % peak-to-peak, a background spectrum was taken. Following this, 3 L of benzene was dosed into the chamber, with the Pt(111) crystal held at 320 K, and then a set of four sample spectra were taken. These four sample spectra were all used to create one average sample spectrum, which was then used with the background spectrum to create the difference spectrum shown in Figure 6.6.

There are three bands in the far-infrared spectrum, shown in Figure 6.6, of benzene adsorbed on Pt(110). The broad band (FWHM = 25 cm^{-1}) at 310 cm^{-1} is assigned to the Pt-benzene stretch of π–bonded benzene on the Pt(110) surface. This is in acceptable agreement with the value of 340 cm^{-1} obtained by Surman *et al.* [17] and Thomas *et al.* [19]. The "derivative" style feature at 470 cm^{-1} and 490 cm^{-1} is indicative of CO being pre-adsorbed in the background spectrum. Due to the large peak height of the peak at 470 cm^{-1} (0.07 %), this peak is assigned to the Pt-CO stretch of a large amount of CO adsorbed on the Pt(110)-(1 × 1) surface in the background spectrum, as shown in the higher coverage spectra in Figure 5.5 in Chapter 5 of this thesis. The peak at 490 cm^{-1} is assigned to the Pt-CO stretch of CO adsorbed on a benzene covered Pt(110)-(1 × 1) surface. This chemical shifting of the Pt-CO peak position occurs because the CO interacts with the co-adsorbed benzene. It is likely that some of the CO is displaced by the adsorption of the benzene, since the peak height of the peak at 470 cm^{-1} is about four times larger than that of the peak at 490 cm^{-1}. A breakdown of the difference spectrum in Figure 6.6 into background and sample spectra is shown schematically in

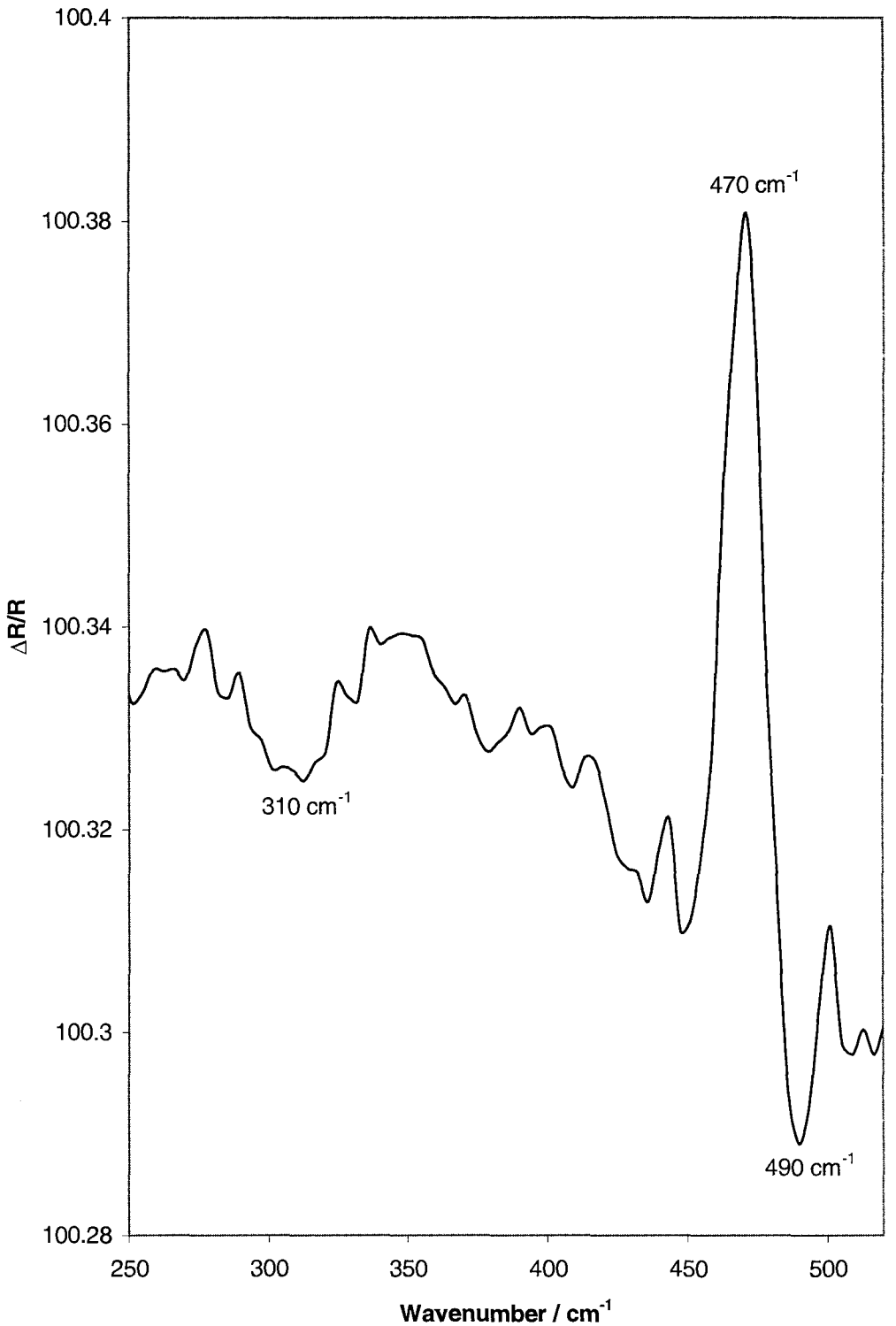

Figure 6.6 – Averaged synchrotron far-infrared RAIR spectrum, with baseline correction, of 3L of benzene adsorbed on Pt(110)- (1 × 1) at 320 K, with a large amount of pre-adsorbed CO.

Figure 6.7.

As the peak at 470 cm^{-1} is due to a large amount of CO adsorption, the reconstruction of the underlying Pt(110) substrate will have been lifted to be (1x1) in nature. It is believed that this is the substrate structure on which benzene was adsorbed in the RAIRS experiment reported in this chapter.

Since benzene was adsorbed at room temperature, it must be chemisorbed in a disordered way, as determined by the LEED studies of Surman *et al.* [14]. The broad nature of the Pt-benzene stretch at 310 cm^{-1} also suggests that there is a large amount of disorder in the benzene chemisorption.

Due to the fact that a saturation amount of benzene was adsorbed, it would be logical that, as stated by Thomas *et al.* [19], the benzene molecule was undistorted during adsorption. This leaves two basic possible adsorption geometries – flat on ridge Pt atoms, as suggested by Surman *et al.* [16], or tilted on the (111) microfacets, as suggested by Zebisch *et al.* [18]. Given that, in RAIRS, only vibrations with components of changes in dipole moment perpendicular to the surface are able to be seen, this means that the tilted benzene (tilted by an angle of 30° to the plane of the macroscopic surface [18]) will have a component of dipole change of any in-plane vibrational modes perpendicular to the surface. Since none of these in-plane modes are seen in Figure 6.6, this shows that the data is consistent with the adsorption of benzene parallel to the surface, although confirm or exclude any other orientation. Combining this observation with the fact that the only other room temperature study of benzene on Pt(110) also supported the view that benzene adsorbed parallel to the surface, leads to the suggestion that benzene adsorbs in a mixture of local geometries on ridge Pt atoms at room temperature, as shown in Figure 6.8.

Spectrum Name	Description	Spectrum
Background	Pt(110)-(1x2) with a large amount of CO adsorbed	470 cm^{-1} = ν(Pt-CO)
	Dose 3 L benzene	
Sample	Pt(110)-(1x2) with co-adsorbed benzene and smaller amount of CO	310 cm^{-1} = ν(Pt-benzene); 490 cm^{-1} = ν(Pt-CO)
Difference	Sample - Background (in percent)	

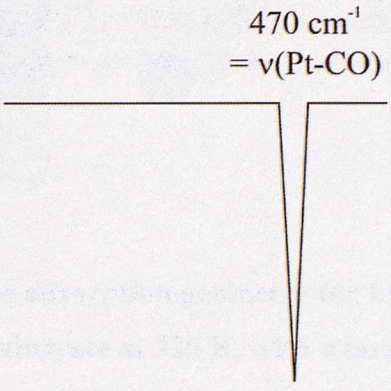

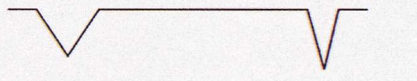

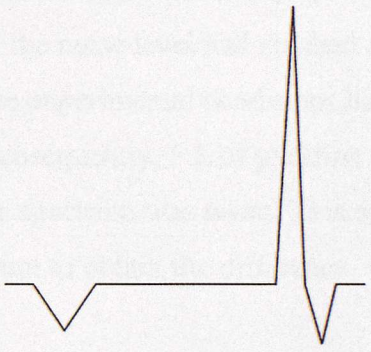

Figure 6.7 – Breakdown of difference spectrum in Figure 6.6 into background and sample spectra

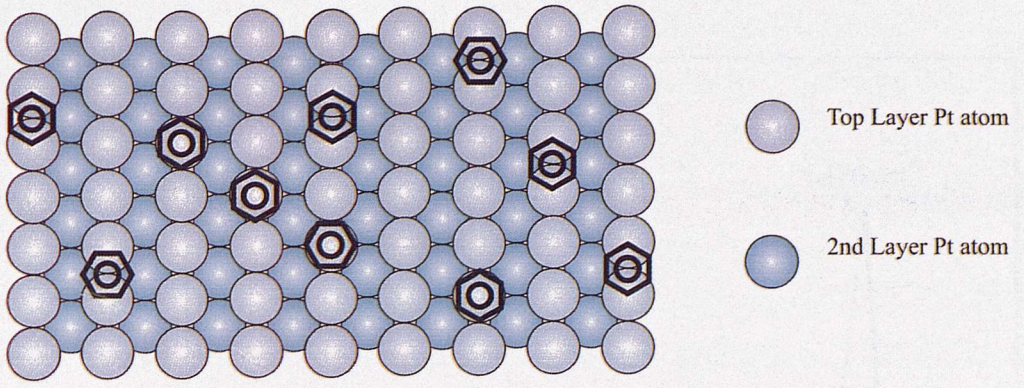

Figure 6.8 –Suggested disordered benzene adsorption geometry for high coverage benzene on a Pt(110)- (1 × 1) substrate at 320 K, with a large amount of pre-adsorbed CO.

6.3.2 Far-Infrared studies of Pt(110)-pyridine at 320 K

The pyridine studies were carried out in a very similar manner to the benzene studies. Prior to the RAIRS experiment taking place, the crystal was heated to remove any adsorbed molecules, and the noise level had reached a consistent value of less than 0.02 %. Once these experimental conditions had been obtained, a background spectrum was taken. Subsequently, 5 L of pyridine was dosed into the chamber, at 320 K, and a sample spectrum was taken. This sample spectrum was used with the background spectrum to obtain the difference spectrum shown in Figure 6.9.

The spectrum obtained after the adsorption of 5 L of pyridine onto the Pt(110)-(1 × 1) surface is very similar to that of benzene adsorption on the same surface, as both have the "derivative" feature with similar peak intensity ratios. This comparison leads to a similar assignment of the two bands present in the RAIR spectrum in Figure 6.9, [17]. Therefore the peak at 470 cm^{-1} is assigned to the Pt-CO stretch of a large amount of CO adsorbed on a Pt(110)-(1 × 1) surface in the background spectrum and the peak at 490 cm^{-1} is assigned to the Pt-CO stretch of CO co-adsorbed on a pyridine covered Pt(110)-(1 × 1) surface.

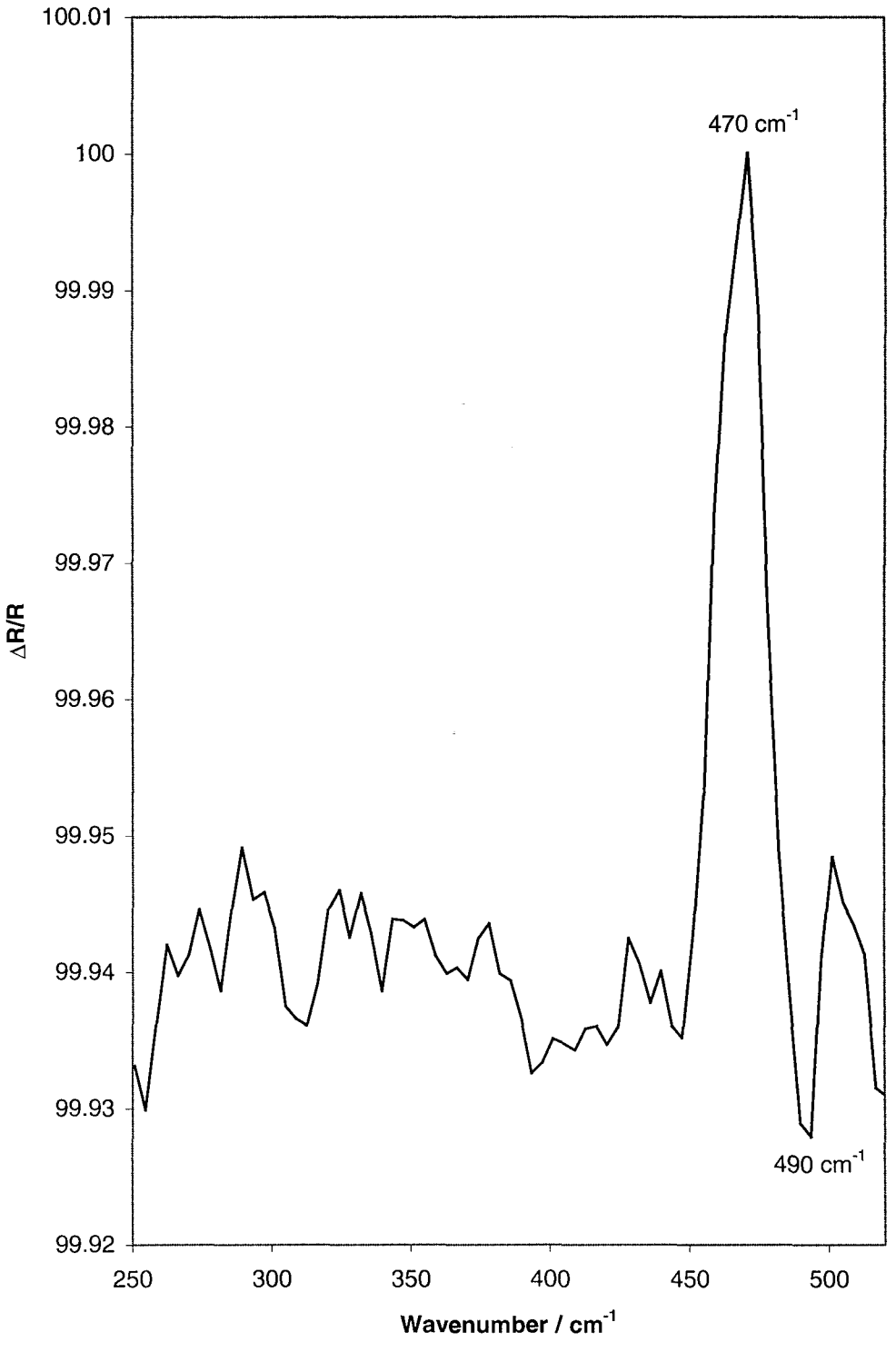

Figure 6.9 –Synchrotron far-infrared RAIR spectrum, with baseline correction, of 5 L of pyridine adsorbed on Pt(110)- (1 × 1) at 320 K with a large amount of pre-adsorbed CO.

Given the large exposure of pyridine in this experiment, it is expected that the adsorbate should bond to the surface through its nitrogen lone pair, as suggested by Surman *et al.* [16, 17]. In the energy range of this far-infrared experiment two peaks should be observed at 300 cm^{-1} and 432 cm^{-1} as seen by Surman *et al.* [16, 17] which would give some information on the Pt-pyridine stretch. Neither of these peaks are present in Figure 6.9. It is possible that the reason for not observing any Pt-pyridine band is that the absorption coefficient of the Pt-NC_5H_5 stretch may be significantly less than that of the Pt-C_5H_5N stretch, the bonding occurring via the nitrogen lone pair in this high coverage situation.

6.4 Conclusions

- This chapter reports the first detection of the Pt(110)-benzene stretch using far-infrared RAIRS as the vibrational detection technique.
- In the cases of benzene and pyridine adsorption on Pt(110) it was shown that both adsorbates could freely adsorb onto a surface covered with a large amount of pre-adsorbed CO, and that the peak from the pre-adsorbed CO could be observed.
- The observation of the Pt-CO peak means that the dosing of either of these molecules can be used as a method of recording the Pt-CO peak from pre-adsorbed CO.
- Since this new experimental protocol for the detection of the Pt-CO stretch is now known, it should be possible to prepare any platinum surface covered in CO, therefore negating the effects of background CO adsorption, and leave it in UHV until a low enough infrared signal-to-noise ratio is obtained before recording the background spectrum, displacing the CO and then recording the sample spectrum.

6.5 *Further Work*

Further synchrotron far-infrared experiments investigating benzene adsorption and low and high coverage pyridine adsorption should be carried out in an environment containing significantly less CO, and with a more stable beam. This would lead to a less noisy spectrum where the only peaks present would be due to benzene or pyridine, and hence a better chance of detecting these peaks. A decrease in beam stability in particular leads to the recording of more noisy spectra, as highlighted by the high levels of noise in the spectra shown in this chapter, which were taken during a period of ring instabilities at the SRS.

It would also be interesting to undertake some UHV scanning tunnelling microscopy (STM) experiments on these Pt-benzene and Pt-pyridine systems. Since STM gives a real space map of the surface it should be possible to first of all gain an image of the platinum substrate and therefore know the positions of the surface platinum atoms. Then if another image of the surface, covering the same area, were taken after dosing either benzene or pyridine, this would show the geometry of the adsorbate molecules. A series of similar experiments and calculations have been carried out on analogous transition metal surfaces, in which the adsorption sites of benzene have been clearly determined [22-25]. Any tilting of the benzene or pyridine on the surface at room temperature could be determined by ARUPS or NEXAFS, as in the low temperature work by Zebisch *et al.* [18].

6.6 *References*

1. H. Ibach, H. Hopster, and B. Sexton, Appl. Phys. 14 (1977) 21.
2. H. Ibach, H. Hopster, and B. Sexton, Appl. Surf. Sci. 1 (1977) 1.
3. H. Ibach and S. Lehwald, J. Vac. Sci. Technol. 15 (1978) 407.
4. J. E. Demuth and D. E. Eastman, Phys. Rev. B 13 (1976) 1523.

5. J. C. Bertolini, G. Dalmai-Imelik, and J. Rousseau, Surf. Sci. 67 (1977) 478.
6. J. C. Bertolini, J. Massardier, and G. Dalmai-Imelik, Faraday Trans. 74 (1978) 1720.
7. J. L. Gland and G. A. Somorjai, Surf. Sci. 38 (1973) 157.
8. P. C. Stair and G. A. Somorjai, J. Chem. Phys. 67 (1977) 4361.
9. R. B. Mayes and P. B. Wells, Advan. Catalysis 23 (1974) 123.
10. G. Herzberg, Molecular Spectra and Molecular Structure. II. Infrared and Raman Spectra of Polyatomic Molecules, Van Nostrand, Princeton, (1945).
11. S. Lehwald, H. Ibach, and J. E. Demuth, Surf. Sci. 78 (1978) 577.
12. F. P. Netzer and J. A. D. Matthew, Solid State Commun. 29 (1979) 209.
13. A. Wander, G. Held, R. Q. Hwang, G. S. Blackman, M. L. Xu, P. Deandres, M. A. Vanhove, and G. A. Somorjai, Surf. Sci. 249 1-3 (1991) 21.
14. M. Surman, S. R. Bare, P. Hofmann, and D. A. King, Surf. Sci. 126 1-3 (1983) 349.
15. G. L. Nyberg, S. R. Bare, P. Hofmann, D. A. King, and M. Surman, Appl. Surf. Sci. 22-3 (1985) 392.
16. M. Surman, PhD Thesis, Chemistry Department, Liverpool University, (1982).
17. M. Surman, S. R. Bare, P. Hofmann, and D. A. King, Surf. Sci. 179 2-3 (1987) 243.
18. P. Zebisch, M. Stichler, P. Trischberger, M. Weinelt, and H. P. Steinruck, Surf. Sci. 396 1-3 (1998) 61.
19. F. S. Thomas, N. S. Chen, L. P. Ford, and R. I. Masel, Surf. Sci. 486 1-2 (2001) 1.
20. B. J. Bandy, D. R. Lloyd, and N. V. Richardson, Surf. Sci. 89 (1979) 344.
21. J. E. Demuth, K. Christmann, and P. N. Sanda, Chem. Phys. Lett. 76 2 (1980) 201.
22. G. Treboux and M. Aono, J. Phys. Chem. B 101 23 (1997) 4620.

23. J. Yoshinobu, M. Kawai, I. Imamura, F. Marumo, R. Suzuki, H. Ozaki, M. Aoki, S. Masuda, S. Tanaka, M. Kamada, and M. Aida, J. Electron Spectrosc. Relat. Phenom. 88 (1998) 997.

24. M. Doering, H. P. Rust, B. G. Briner, and A. M. Bradshaw, Surf. Sci. 410 2-3 (1998) L736.

25. P. Sautet and M. L. Bocquet, Phys. Rev. B 53 8 (1996) 4910.

Chapter Seven – Preliminary UHV Electrochemical Transfer Experiments

7.1 Introduction

The study of electrode-electrolyte interfaces is of great importance due to the large number of industrial catalytic processes that are electrochemical in nature. While a wide range of electrochemical studies covering many research fields have been and continue to be investigated [1], it is apparent that traditional electrochemical techniques used in most studies can only deal with the macroscopic characteristics of the interface. Consequently, little microscopic information, such as the surface electronic structure, atomic composition, and morphology of the electrode materials, is known.

Advances in UHV surface analytical techniques [2] have shown that both atomic and molecular level information can be obtained at the solid-gas interface. Many of these UHV techniques use electron emission or electron scattering to probe the surface, and thus cannot be used *in situ* in the electrochemical environment. Therefore, in order to determine the structure, composition, and chemical state of the electrode surface, the *ex situ* analysis of the electrode surface by these powerful techniques, before and immediately after removal from the liquid electrochemical environment, would be highly beneficial.

This multidisciplinary method, however, requires a controlled transfer of a well-characterised sample between the UHV surface analysis chamber and the electrochemical cell. The first reported use of such a transfer system was by Hubbard in 1980 [3]. He described a set of apparatus that consisted of a UHV system connected to an electrochemical cell through a suitable vacuum interlock. The UHV chamber was equipped for LEED, Auger spectroscopy, photoelectron spectroscopy and thermal desorption mass spectroscopy. This allowed the surface

characterisation of samples before and after the electrochemical experiments. The electrochemical cell consisted of the standard three-electrode arrangement comprising a working electrode (the sample), reference electrode (such as Ag / AgCl / KCl) and a counter electrode. This enabled the current to be measured while a potential was applied to the working electrode – the basic principle of electrochemistry. The cell used by Hubbard was made from glass, and air was removed and excluded from the solutions to stop unwanted oxidation. The transfer experiment devised by Hubbard began with characterisation of the sample in UHV. Once this was complete, an inert atmosphere was introduced and the cell was filled with electrolyte. Next, the surface was electroanalytically characterised, following which the chamber was re-evacuated and the electrode surface and electrodeposited layers were re-characterised in UHV by LEED and related techniques.

The next report of a transfer system was in 1983 by Homa *et al.* [4], employing a three-chamber approach to the apparatus. This consisted of one chamber in which to characterise the samples under UHV conditions. The samples were transferred to a second UHV chamber, separated from the first by a valve, by a magnetically coupled manipulator without loss of UHV conditions. Ultra pure argon was introduced into the second chamber to provide an inert atmosphere for wet electrochemical studies. A thin-layer cell could then be formed in the second chamber using a combined Pd / H counter / reference electrode, which had been prepared in a third UHV chamber attached to the system.

Homa *et al.* used an all-Teflon electrolyte delivery system to allow dilute HF to be used as the electrolyte, because HF would have etched an all-glass system. The electrolyte was first applied to the horizontal surface of the Pd / H counter / reference electrode as a single drop and then the cell raised to bring the electrolyte into contact with the single-crystal electrode under potential control in the second chamber. Following the electrochemical analysis of the surface, the sample and electrode were separated and the small amount of electrolyte was volatised as the pressure was rapidly pumped down to about 10^{-8} Torr in the

second chamber. The sample was then returned to the first chamber to be re-examined using various UHV techniques. This system is very similar to that of Hubbard [3], with the main differences being the change of electrolyte and reference / counter electrode and the use of a third chamber to prepare the electrochemical cell.

Ross and Wagner [5] also employed a three-chamber approach to their transfer system. They use two manipulators to move the sample. The first is a vertical offset manipulator, which moves the sample in the UHV chamber, and the second is a horizontal magnetic manipulator, which transfers the sample from the UHV chamber to the electrochemical chamber. The sample was held on the horizontal manipulator during the electrochemical experiments. As in the experiments by Homa *et al.* [4], Ross and Wagner used a Pd / H reference electrode, but a separate counter electrode made from Pt was used. In a similar way to Hubbard [3], Ross and Wagner introduced their electrolyte from an external reservoir via a PTFE capillary tube to form a drop on the counter / reference ring-disc, which could be sandwiched between the ring-disc and the sample to make electrical contact.

Some years later, other research groups built similar apparatus designed for electrochemical transfer experiments [6-14]. These all used the three-chamber approach, with a horizontal manipulator to move the sample between chambers, and various different reference electrodes were employed.

As suggested in the opening paragraph of this chapter, this type of electrochemical transfer system can be used to investigate many electrochemical industrial processes. One such process is the fuel cell reaction, in which platinum is used as both the cathode and anode in order to convert fuels, like methanol, into carbon dioxide and water, proving energy to power vehicles [15]. Unfortunately, if methanol is used directly as the fuel, the process goes via a CO-like intermediate, which poisons the catalyst. If the methanol is reformed to hydrogen before being used as the fuel, the hydrogen contains about 1 % CO from this

process. It has been shown that even a very small amount of CO, 100 ppm, greatly reduced the performance of the catalyst [15]. Due to the importance of this process, a large amount of electrochemical research has been carried out on the interaction of CO with platinum surfaces, and methods to alter the surface to reduce its susceptibility to poisoning have been investigated.

An important type of electrochemical experiment to perform on platinum electrodes is to adsorb CO onto the surface at a fixed potential, then monitor the current as the potential is increased linearly with time. This type of experiment is called a CO stripping experiment, or CO electrooxidation, and gives rise to an increase in current at the point where CO is oxidised off the surface. The lower the potential at which the stripping peak occurs, the easier the desorption from the surface in question. This is important because, due to the CO poisoning of platinum, any change in the electrode that can aid the removal of CO is of great benefit.

Clavilier *et al.* performed a set of CO stripping experiments on Pt(110) and Pt(111) electrodes made from beads [16]. They carried out their experiments in 0.1 M perchloric acid solution because of the absence of adsorption of supporting electrolyte anions, thus avoiding a competition process with adsorbing CO, and used a reversible hydrogen electrode (RHE) as the reference electrode. The CO was adsorbed onto both surfaces by bubbling CO through the solutions whilst holding the potential of the surfaces at 0.085 V vs RHE. CO was then eliminated from both solutions by bubbling the solutions with argon, following which the potentials were ramped at 50 mVs^{-1} and the spectra were recorded. The Pt(110) surface gave a CO stripping peak position of 0.68 V vs RHE, whereas the Pt(111) surface gave a CO stripping peak position of 0.75 V vs RHE. This implied that CO desorbs more easily from the Pt(110) electrode.

A similar type of experiment was carried out by Friedrich *et al.* on a Pt(111) single crystal, and on the same crystal once its surface had been modified with ruthenium [17]. The ruthenium deposition was performed under potential control

in 0.1 M sulphuric acid containing 5 mM $RuCl_3$, giving a ruthenium coverage of about 50 %. Their experiments were also carried out in 0.1 M perchloric acid solution, but with a rate of potential ramping after CO adsorption of 1 mVs^{-1}. The ruthenium modified Pt(111) surface gave a CO stripping peak potential of 0.5 V vs RHE, a negative shift of 0.25 V compared with the clean Pt(111) surface [16]. This indicates that the presence of ruthenium on the surface dramatically improves the so-called CO tolerance of the platinum surface.

A set of Monte Carlo simulations for CO electrooxidation on Pt-Ru surfaces were performed by Koper *et al.* in 1999 [18]. These simulations showed many predicted CO electrooxidation voltammograms for various ruthenium coverages ranging from pure platinum to pure ruthenium, and for various CO diffusion rates, using a sweep rate of 50 mVs^{-1}. The main conclusion from these calculations was that CO mobility is vital for the Pt-Ru surface to be more active than the pure element platinum and ruthenium. Comparing the results of the calculations for ruthenium coverages of 50 % with different CO diffusion rates, with the results of Friedrich *et al.* [17], where the ruthenium coverage was also 50 %, showed that the best match for peak shape and position came from the calculation with the higher CO diffusion rate, thus suggesting that CO is quite mobile on the surface.

Following the electrochemical research by Clavilier *et al.* [16] and Friedrich *et al.* [17], which yielded macroscopic data concerning the bonding of CO to the platinum and modified platinum surfaces in an electrochemical environment, transfer experiments were carried out by various groups [11, 12, 14, 19]. In these investigations, electrochemical transfer experiments were carried out on atomically well-characterised platinum single crystal surfaces, which had been modified by bismuth or ruthenium.

The first electrochemical transfer experiments on these types of systems were carried out by Gasteiger *et al.* [19]. They investigated the electrocatalytic activity of different sputter-cleaned Pt-Ru bulk alloys as a function of their ruthenium surface concentration. Each sample was cleaned in UHV by sputter-

anneal cycles until shown to be clean by AES. The surface composition was determined by LEIS analysis. The sample was then transferred from UHV to an inert atmosphere in which it was brought into contact with the CO saturated 0.5 M sulphuric acid solution and CO was deposited onto the samples at a potential of 0.075 V vs Pd / H. A series of CO stripping experiments were then carried out on each sample at a sweep rate of 20 mVs^{-1}. The lowest CO stripping peak potential, and hence the most active catalyst for CO desorption, was the Pt-Ru alloy with a surface composition of 50 % ruthenium, which is consistent with the results of Friedrich *et al.* [17] and Koper *et al.* [18]. Similar CO stripping experiments were also performed on Pt-Ru alloys with almost identical percentages of ruthenium in the surface layer, as shown by LEISS, but prepared by different techniques. One had been prepared by sputtering, which left the random distribution of the bulk alloy intact at the surface, giving a random distribution of single ruthenium atoms in the surface layer. The other was prepared by annealing, which caused the ruthenium to cluster, causing large, spread-out islands of ruthenium atoms on the surface, as suggested by a set of Monte Carlo calculations by Vurnes *et al.* [20]. The CO stripping peak potential for the sputtered surface is roughly 0.1 V less than on the annealed surface. This can be explained by the increased number of Pt-Ru pairs in the sputtered surface, which are believed to be important in the bi-functional nature of the ruthenium enhancement of CO desorption from a Pt-Ru surface.

Hayden and co-workers have studied the electrooxidation of CO on ruthenium modified Pt(110) and Pt(111) single crystals using electrochemical transfer techniques [12, 14]. Both crystals were modified by ruthenium overlayers, which were deposited by metal vapour deposition (MVD) in the UHV chamber. These ruthenium overlayers were then characterised by LEED, XPS and LEISS before and after transfer to the electrochemical cell where they were studied using cyclic voltammetry. The coverage of ruthenium on both surfaces was monitored by XPS and LEISS. The values of ruthenium coverage given by XPS were always larger than those given by LEISS. This was attributed to the formation of ruthenium clusters following deposition.

CO stripping experiments were carried out using four different types of Pt(110)-Ru surfaces [12]. These surfaces were created following (a) MVD deposition at 300 K, (b) annealing at 625 K, (c) annealing at 750 K and (d) annealing at 1050 K. The XPS and LEISS data indicated that the higher the annealing temperature, the more ruthenium dissolved from the surface into the bulk of the crystal. The lowest CO stripping peak potential was for surface (b) – the lowest annealing temperature. This surface was the most effective at stripping the CO than surface (a) because it had ruthenium incorporated in the top layer, through annealing, rather than by a similar coverage in the adsorbed phase. Increased annealing caused the ruthenium to dissolve further into the bulk, where its ability to promote CO electrooxidation was negligible. This explains why the CO stripping peak potential was increased after further annealing above 625 K.

The electrooxidation of CO on Pt(111) modified by ruthenium was shown to be characterised by two oxidation peaks (at about 0.6 V and 0.7 V vs RHE) in the stripping voltammetry [14], both at potentials significantly lower than that found on Pt(111) under similar conditions [16]. This overall promotion was associated with the bi-functional mechanism. The first of the two promoted oxidation peaks (0.6 V) was attributed to fast oxidation kinetics of CO adsorbed on platinum sites adjacent to a ruthenium cluster. The second oxidation peak (0.7 V) was then associated with the oxidation of CO adsorbed on platinum sites that lay at least one platinum atom away from the ruthenium sites. The higher potential of this second oxidation peak was attributed to the extra energy required for the CO to diffuse across the surface to the Pt-Ru edge before desorbing.

In order to determine the platinum surface sites that the CO molecules were being desorbed from, Lin *et al.* combined CO electrooxidation experiments after electrochemical transfer with *in situ* mid-infrared FTIR studies [13, 21]. Their first set of experiments concerned polycrystalline platinum, polycrystalline ruthenium, and a Pt-Ru (50:50) alloy [21]. Their electrooxidation experiments agreed with previous reports [12, 14, 17, 19] that the Pt-Ru alloy gave the most promotion to CO electrooxidation. Their infrared data showed that the peak

position of the C-O vibration of CO adsorbed in atop sites on these three surfaces are quite different. On the polycrystalline platinum the peak position was 2070 cm^{-1}, on the Pt-Ru alloy the peak position was 2060 cm^{-1}, and on the polycrystalline ruthenium the peak position was 2010 cm^{-1}.

In the second set of experiments by Lin *et al.* the electrooxidation of CO on a ruthenium modified Pt(111) electrode was studied [13]. The ruthenium was deposited under potential control, and the coverage was calculated by AES in the UHV chamber. This allowed different ruthenium coverages to be studied by CO electrooxidation and *in situ* mid-infrared FTIR. The electrooxidation experiments showed again that the presence of ruthenium on the platinum surface greatly improved the promotion of CO electrooxidation. The infrared experiments showed that, on low ruthenium coverage Pt(111) surfaces, CO adsorbed on the platinum in atop and two-fold bridge sites (in a ratio of roughly 5:1, atop:bridge). As the ruthenium coverage increased the peak due to the $C\text{-}O_{bridge}$ stretch soon disappeared, and a new peak due to atop bonded CO adsorbed on ruthenium grew in. This highlights the importance of CO adsorption on ruthenium as a part of the CO electrooxidation process.

The work in this chapter describes the addition of an electrochemical transfer system to the UHV chamber on beamline 13.3 at Daresbury, and gives results from initial transfer experiments. These results show that the transfer system enables samples to be transferred from one chamber to another whilst keeping the sample clean. The initial ruthenium deposition experiments highlight how complicated these experiments are to perform, but show great potential to yield important results concerning the bonding of CO to Pt-Ru substrates.

7.2 *Experimental*

The experimental results presented in this chapter were obtained using the UHV chamber at beamline 13.3 at Daresbury laboratory. A diagram of the chamber can be found in Chapter 2 of this thesis, Figure 2.15.

The experiments at Daresbury were carried out in a diffusion pumped UHV chamber (base pressure 1×10^{-10} mbar) equipped for LEED (low energy electron diffraction), XPS (X-ray photoelectron spectroscopy) and RAIRS (reflection absorption infrared spectroscopy). The chamber was also fitted with a QMS (quadrupole mass spectrometer), an ion gun, and TPD (temperature programmed desorption) apparatus.

The Pt(110) and Pt(111) crystals (15×5 mm^2) could be heated by electron beam bombardment or radiatively using a well outgassed tungsten filament, and cooled by conduction to a liquid nitrogen reservoir. The crystals were cleaned by roasting in 2×10^{-7} mbar of oxygen at 925 K and annealing *in vacuo* to 1225 K, followed by cycles of 1 keV Ar^+ sputtering with a drain current of 6 μA and annealing to 1225 K. During the sputtering the crystals were translated along their long axes, which were in the plane perpendicular to the ion beam, to ensure that the whole of the surfaces were sputtered. The cleanliness of the crystals was confirmed by XPS and LEED.

The RAIR spectra were obtained at 8 cm^{-1} resolution with a custom vacuum interferometer based on the Nicolet impact modulator with a silicon beamsplitter and an Infrared Laboratories liquid helium cooled (4.2 K) silicon bolometer. The light was reflected at about 87°, off-normal, from the crystal surface. Interferograms were recorded in blocks of 256 scans (90 s accumulation time) and normalised to the stored current in the SRS. The apodisation function was triangular with a notch to remove a small sideband caused by interference in the detector itself.

7.3 *Results and Discussion*

7.3.1 Modification of beamline 13.3 for transfer experiments

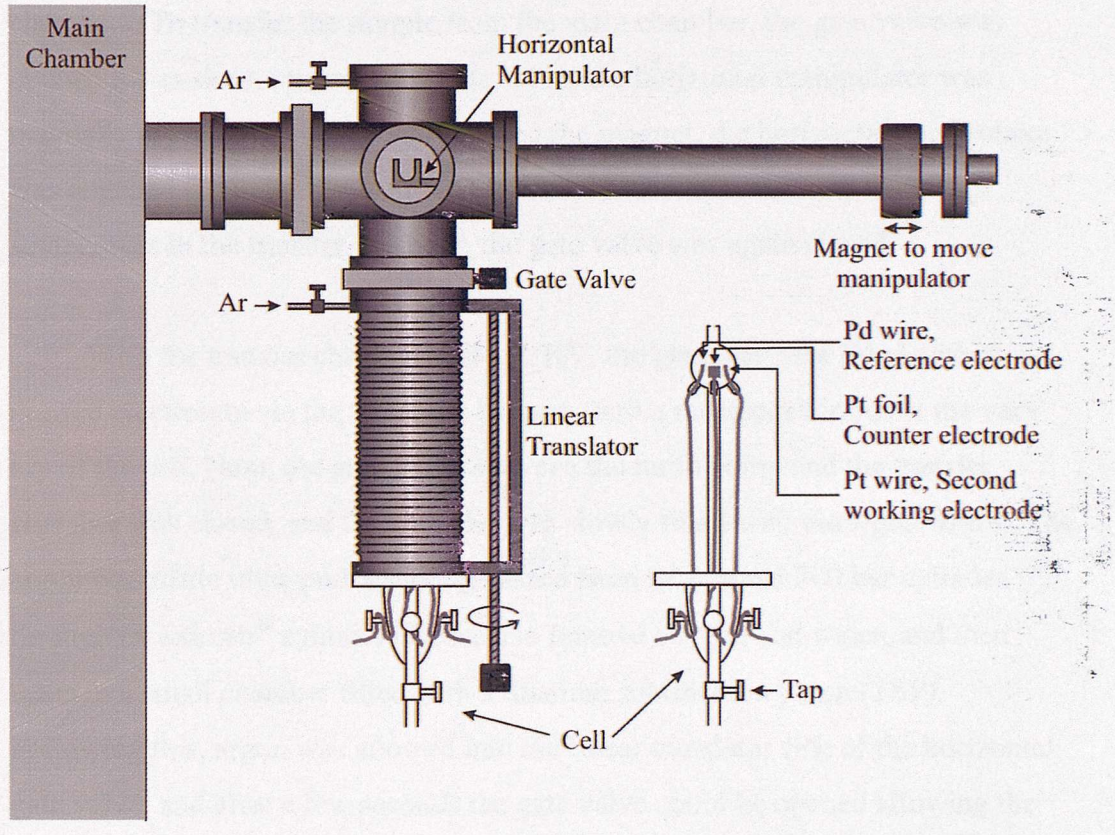

Figure 7.1 – Side view of the transfer system on station 13.3 at the SRS at Daresbury

Figure 7.1 shows a diagram of the transfer system that was developed and built on station 13.3 as a part of this project. This apparatus allows the sample to be characterised in the main chamber under UHV conditions by XPS, RAIRS and LEED, transferred from this chamber to the transfer chamber, have electrochemical experiments carried out in an atmosphere of ultra-pure argon, and be transferred back to the main chamber for re-characterisation. It employed the

three chamber method as used by various other groups [4-7] and described earlier in this chapter.

The transfer chamber was normally pumped by a turbo pump, and had a typical base pressure of 10^{-8} mbar. So as not to make the pressure in the main chamber lower than its usual 10^{-10} mbar, a closed gate valve separated these two chambers. To transfer the sample from the main chamber, the gate valve was opened for as short a time as possible, while the horizontal manipulator was manually moved into the chamber. Using the magnet, the horizontal manipulator was engaged around the stub and retracted with the stub attached. Once the sample was in the transfer chamber, the gate valve was again closed.

With the transfer chamber still at UHV, the glass cell was filled with the desired electrolyte via the tap at the bottom, until a meniscus formed at the very top of the cell. Next, the gate valve between the turbo pump and the transfer chamber was closed, and the chamber was slowly filled with ultra-pure argon. The argon was made ultra-pure by being passed from its original 300 bar cylinder through an oxisorb® cylinder (Messer) to remove oxygen and water, and then through a small chamber fitted with a titanium sublimation pump (TSP). Following this, argon was allowed into the linear translator side of the horizontal gate valve, and after a few seconds the gate valve could be opened allowing the cell to be moved slowly towards the sample by using the linear translator, to make contact between the meniscus of the electrolyte and the sample.

Once contact had been achieved, the electrodes were connected to the corresponding outputs on the potentiostat. The potentiostat was connected to a waveform generator, in order to perform electrochemical experiments, and to a chart recorder, to record the data on paper. Once the desired electrochemical experiments had been completed, the cell was moved down past the gate valve, and the gate valve is closed. Next, the argon supply was turned off, and the transfer chamber was pumped by a sorption pump to remove as much moisture as possible. When the sorption pump had been pumping for about 20 minutes, the

gate valve to the turbo pump was opened, and the chamber was pumped until it reached a pressure close to 10^{-8} mbar. Once this was achieved, the gate valve separating the two chambers was opened, and the stub was transferred back to the vertical manipulator in the main chamber to be characterised, and the horizontal manipulator was retracted, and the gate valve closed.

7.3.2 Far-Infrared studies of Pt(110) after a single electrochemical transfer

The Pt(110) crystal was cleaned and characterised in UHV as described in Section 7.2, and shown to be free of any adsorbates. The crystal was then heated to 700 K, and allowed to cool, during cooling 0.5 L of CO was allowed into the chamber to adsorb on the previously clean surface.

The crystal was then transferred into the transfer chamber, which was subsequently closed off from the main chamber by shutting the gate valve. Next, the transfer chamber was filled with dry nitrogen, and remained in this environment for a couple of minutes to simulate an electrochemical transfer experiment. After this, the transfer chamber was pumped down to 10^{-8} mbar and the crystal was transferred back into the main chamber.

Following this, a background spectrum of the CO covered Pt(110) surface was taken. Then, as indicated in Section 6.4 of Chapter 6, 2 L of pyridine was dosed into the chamber to displace as much of the CO as possible, after which a series of sample spectra were recorded and subsequently added together. The difference spectrum (sample spectrum divided by background spectrum) for this "dummy" transfer is shown in Figure 7.2.

In the far-infrared RAIR spectrum shown in Figure 7.2 there are two downward peaks at 486 cm^{-1} and 560 cm^{-1}, and one upward peak at 470 cm^{-1}. The peak at 486 cm^{-1} is due to the Pt-CO stretch on a partially pyridine covered surface. The upward peak at 470 cm^{-1} is due to the Pt-CO stretch on a non-pyridine covered surface, which was the case in the background spectrum.

Although the peak at 470 cm^{-1} is not clear, due to the relatively large amount of noise (about 0.15 % in this experiment), similar features were seen in Chapter 6 in which other CO perturbation experiments carried out entirely in UHV, using both pyridine and benzene as perturbation molecules giving the basis for this assignment of the 470 cm^{-1} and 486 cm^{-1} peaks. The origin of the peak at 560 cm^{-1} is unclear. The most plausible assignment of this peak is that it is a Pt-pyridine mode, as seen by Nyberg *et al.* [22] but not assigned by them.

Since Figure 7.2 shows that the most important peak, the Pt-CO peak at 470 cm^{-1}, is barely detectable above the noise, pyridine is shown to be a less satisfactory molecule for displacing CO from a platinum surface than first thought. This could be due to the fact that, in this "dummy" transfer experiment, the CO was dosed on purpose by back-filling the chamber, rather than simply being adsorbed from the background, as in the pyridine experiment in Figure 6.9 in Chapter 6. This could lead to the CO adlayer being packed closer together, and hence harder to displace. Another problem in using pyridine as a displacing molecule is the fact that it showed signs of a detectable infrared spectrum in the region of interest, which could mask any chemically important peaks following transfers in the future.

This "dummy" transfer has shown that, aside from the problems encountered by using pyridine to displace CO, no features associated with the transfer procedure are present in the infrared spectrum. The combination of this information with the fact that the peak at 470 cm^{-1} is in exactly the same position as in the pyridine and benzene experiments carried out in Chapter 6, shows that the process of transferring the crystal from the UHV chamber into the dry nitrogen environment and back into the UHV chamber was successful in keeping the cleanliness of the crystal intact. This, therefore, augurs well for future real electrochemical transfer experiments where ultra-pure argon will be used as the inert atmosphere instead of dry nitrogen.

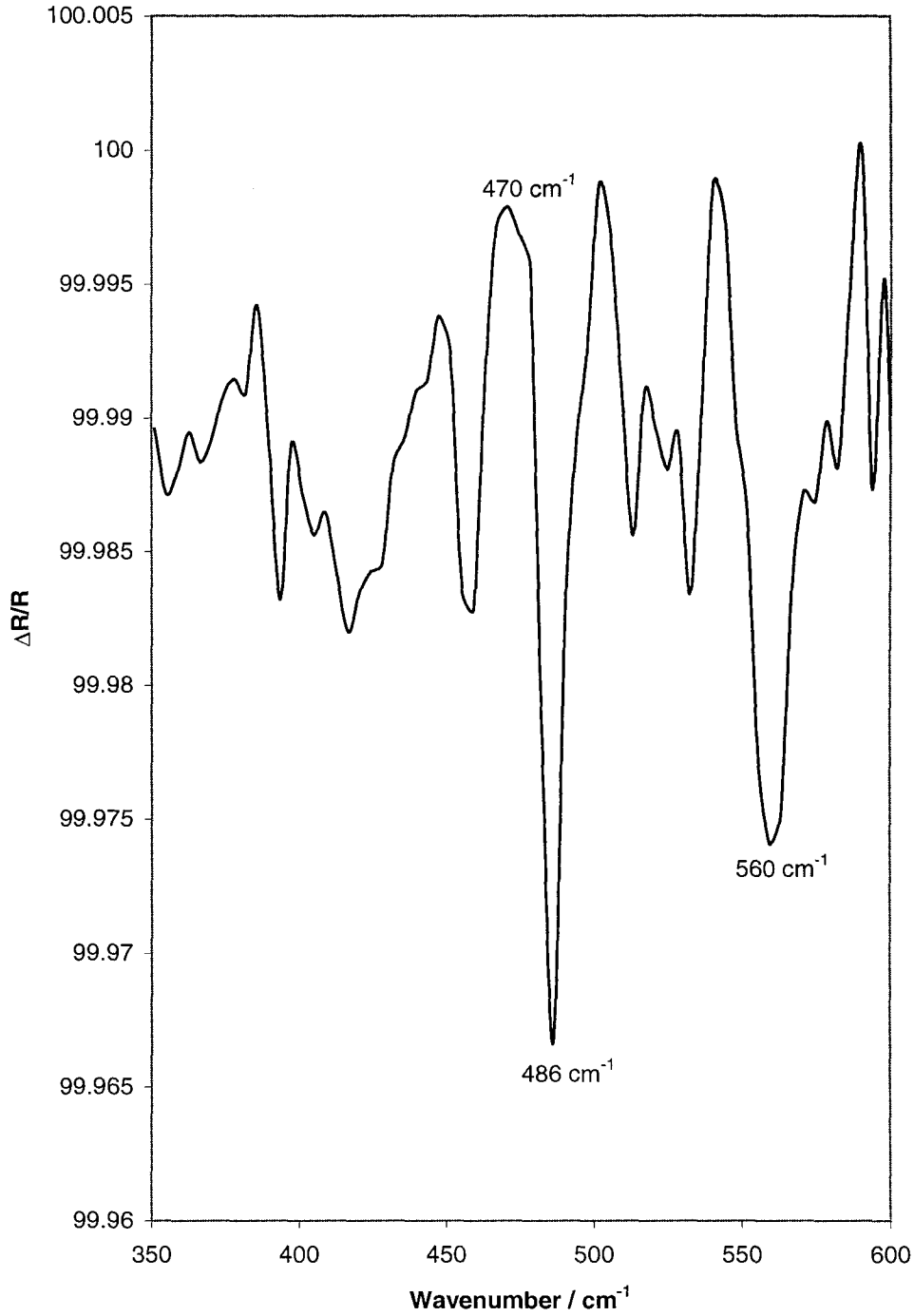

Figure 7.2 – Far-infrared RAIR spectrum of a CO covered Pt(110) crystal after the attempted displacement of CO by dosing pyridine. This infrared measurement occurred after a single transfer of the CO covered Pt(110) crystal from the UHV chamber into a chamber with a dry nitrogen atmosphere, and back into the UHV chamber.

7.3.3 *Under potential deposition of ruthenium on Pt(111)*

A clean Pt(111) crystal was prepared in UHV by the typical procedures of sputtering, annealing and roasting in oxygen. An XPS spectrum was taken prior to transferring the crystal from the UHV chamber, which confirmed its cleanliness. Once the crystal was in the transfer chamber, the chamber was filled with an atmosphere of ultra-pure argon. Meanwhile, the electrochemical cell had been filled with an electrolyte consisting of 0.15 mM $RuCl_3$ in 0.1 M perchloric acid solution as used by Lin *et al.* [13]. Next, the electrochemical cell was slowly moved up towards the crystal until meniscus contact was formed. A potential of 0 V vs Pd / H was passed for 5 minutes, during which a small current, about – 5 μA, was detected. The chamber was then pumped down and the crystal transferred back into the UHV chamber for characterisation. An XPS spectrum of the region that should contain the most intense ruthenium peaks was taken. This spectrum showed no signs of any ruthenium peaks, so it was assumed that very little ruthenium was deposited onto the surface. Despite repeating this experiment many times, using longer deposition times, no ruthenium was ever seen in the XPS spectra recorded.

Since the crystal heating mechanism had broken during the many transfer attempts, the (111) nature of the crystal could not be assumed to be intact. It was much more likely that by this stage the platinum crystal had become polycrystalline in nature. A CO stripping experiment was performed on the polycrystalline platinum crystal following the attempted ruthenium deposition. As shown by Friedrich *et al.* [17], the presence of ruthenium on a platinum surface lowers the peak potential of electrooxidised CO. This experiment was carried out in the transfer chamber in the ultra pure argon atmosphere. A 0.1 M perchloric acid solution was bubbled with CO until saturation and then made to form a meniscus contact (of 2 mm radius) with the platinum crystal, which was held at 0.05 V vs RHE. The solution was then changed to clean 0.1 M perchloric acid. The stripping CV was then run from 0.05 V to 0.9 V (called DL - CO strip in Figure 7.3) using a scan rate of 100 mVs^{-1}, and then a background CV was

recorded over the same potential range (called DL - Background in Figure 7.3). A separate CO stripping experiment was performed at Southampton University using a polycrystalline platinum disc electrode (radius 6 mm) as the working electrode, and also in 0.1 M perchloric acid solution, but this time cycling between 0 V and 1.55 V vs RHE. The CO stripping scan is shown as "Soton – CO strip" in Figure 7.3 and the background scan is shown as "Soton - background".

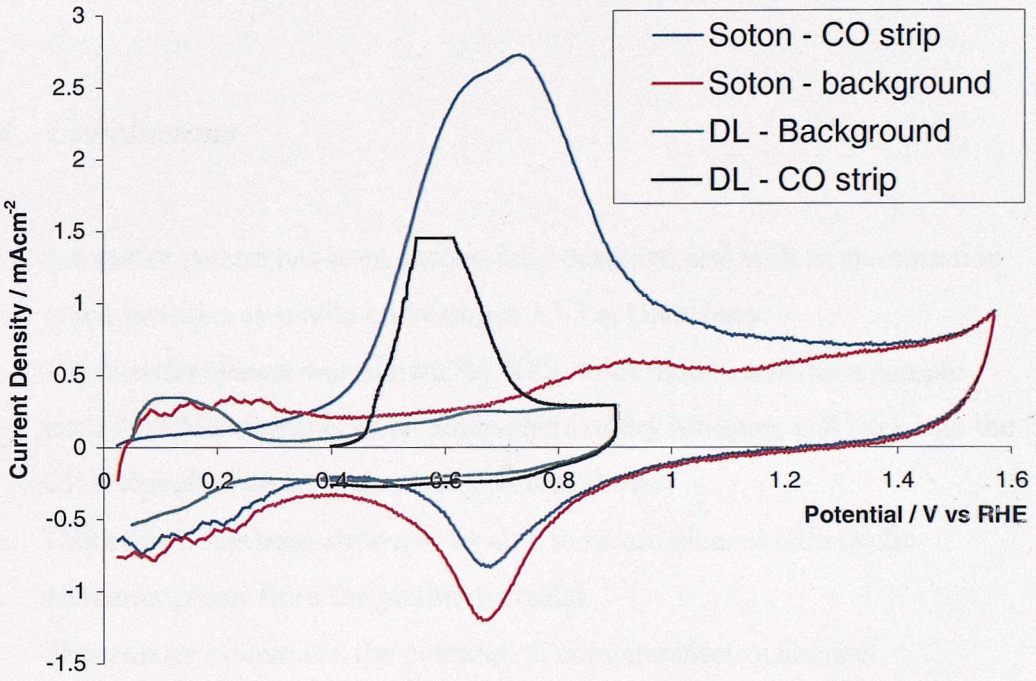

Figure 7.3 – Set of CO stripping and background CVs of polycrystalline platinum in 0.1 M perchloric acid at a scan rate of 100 mVs^{-1}. Note that the flat top of the "DL – CO strip" CV is because the pen reached the upper limit of the chart recorder.

Since the area under the CO stripping CV on the DL platinum surface is about a third of that of the CO stripping CV on the Southampton platinum surface, and the effective surface area of the DL surface is about a tenth of the Southampton surface, this shows that only a very small amount of CO has been adsorbed on the DL platinum surface. It is this small amount of CO adsorption

that is believed to cause the shift of the CO stripping peak to lower potential, rather than any promotion from ruthenium. The lack of promotion is also highlighted by the fact that both CO stripping curves have almost identical electrooxidation onset potentials, unlike in the promoted case, observed by Friedrich *et al.* [17], where ruthenium promotion lowered the onset potential by about 0.15 V. It has therefore been shown, by both XPS and cyclic voltammetry, that it was not possible to deposit ruthenium onto the platinum surface under the experimental conditions described in this section.

7.4 Conclusions

- A transfer system has been successfully designed and built as an extension to the facilities available on beamline 13.3 at Daresbury.
- The transfer system was shown, by XPS, to be able to transfer a sample from the UHV chamber to an atmosphere of dry nitrogen, and back into the UHV chamber whilst maintaining its cleanliness.
- This system has been shown to be able to record clear ex-situ cyclic voltammograms from the platinum crystal.
- The transfer system has the potential to combine electrochemical experiments, which mirror industrial processes more closely, with the powerful UHV analytical techniques, in particular far-infrared RAIRS.

7.5 Further Work

As pyridine was found not to be useful as a displacement molecule for CO on platinum surfaces, other molecules need to be tested for their suitability. The three most important criteria for suitability are effective displacement of CO from a platinum surface in UHV conditions (a useful way to test this would be to see if the displacement molecule had a higher desorption temperature than CO from the substrate surface), no detectable RAIRS features in the far-infrared region of the

spectrum, and that the molecule is able to be pumped quickly from the UHV chamber. All molecules to be tested should be used in the place of pyridine in experiments that are the same as described in Section 7.3.2.

Since it was not possible to detect ruthenium in the XPS spectra after under potential deposition, this experiment needs to be repeated with some modifications. The most beneficial modification might be to increase the concentration of the ruthenium in the solution by a factor of about 100, thus increasing the likelihood of depositing ruthenium on the surface. This could overcome one of the problems encountered by using only 0.15 mM $RuCl_3$ in conjunction with the small contact area of the meniscus as compared to the large size of the sample used for the far-infrared RAIRS and XPS experiments. It would also be useful to re-design the electrochemical cell to give a larger meniscus size and hence contact area, and therefore deposit ruthenium over a larger surface area. It might also be interesting to change the electrolyte from perchloric acid to sulphuric acid, as used by Davies and co-workers [12, 14].

It could also be helpful to try to use metal vapour deposition (MVD) to deposit ruthenium on the platinum surface in the UHV chamber before trying a UPD experiment, as MVD have been shown to be easier to implement and characterise [12, 14], and would give a useful set of data to compare future UPD results to.

Once ruthenium can be deposited onto the platinum surface by UPD, its coverage can be quantitatively monitored by XPS. Following this, far-infrared RAIR spectra of CO adsorbed on these surfaces can be recorded using the displacement method described in Section 7.3.2. Since the far-infrared region of the spectrum contains the substrate-CO stretching vibrations, which are far more sensitive to the bonding site of the CO [23], this will give a great amount of information on the exact nature of the bonding of CO on these mixed Pt-Ru substrates.

7.6 References

1. J. O. M. Bockris, B. E. Conway, E. Yeager, and R. E. White, Comprehensive Treatise of Electrochemistry, Plenum, New York, (1981).
2. G. A. Somorjai, Chemistry in Two Dimensions: Surfaces, Cornell University Press, New York, (1981).
3. A. T. Hubbard, Acc. Chem. Res. 13 (1980) 177.
4. A. S. Homa, E. Yeager, and B. D. Cahan, J. Electroanal. Chem. 150 1-2 (1983) 181.
5. P. N. Ross and F. T. Wagner, 13 (1984) 69.
6. M. Wasberg, L. Palaikis, S. Wallen, M. Kamrath, and A. Wieckowski, J. Electroanal. Chem. 256 1 (1988) 51.
7. L. W. H. Leung, T. W. Gregg, and D. W. Goodman, Rev. Sci. Instrum. 62 7 (1991) 1857.
8. L. W. H. Leung, T. W. Gregg, and D. W. Goodman, Langmuir 7 12 (1991) 3205.
9. D. E. Gardin and G. A. Somorjai, Rev. Sci. Instrum. 64 5 (1993) 1305.
10. X. P. Xu, H. Bojkov, and D. W. Goodman, J. Vac. Sci. Technol. A-Vac. Surf. Films 12 4 (1994) 1882.
11. B. E. Hayden, A. J. Murray, R. Parsons, and D. J. Pegg, J. Electroanal. Chem. 409 1-2 (1996) 51.
12. J. C. Davies, B. E. Hayden, and D. J. Pegg, Electrochim. Acta 44 6-7 (1998) 1181.
13. W. F. Lin, M. S. Zei, M. Eiswirth, G. Ertl, T. Iwasita, and W. Vielstich, J. Phys. Chem. B 103 33 (1999) 6968.
14. J. C. Davies, B. E. Hayden, D. J. Pegg, and M. E. Rendall, Surf. Sci. 496 1-2 (2002) 110.
15. R. A. Lemons, J. Power Sources 29 1-2 (1990) 251.
16. J. Clavilier, R. Albalat, R. Gomez, J. M. Orts, J. M. Feliu, and A. Aldaz, J. Electroanal. Chem. 330 1-2 (1992) 489.

17. K. A. Friedrich, K. P. Geyzers, U. Linke, U. Stimming, and J. Stumper, J. Electroanal. Chem. 402 1-2 (1996) 123.
18. M. T. M. Koper, J. J. Lukkien, A. P. J. Jansen, and R. A. van Santen, J. Phys. Chem. B 103 26 (1999) 5522.
19. H. A. Gasteiger, N. Markovic, P. N. Ross, and E. J. Cairns, J. Phys. Chem. 98 2 (1994) 617.
20. G. H. Vurens, F. Vandelft, and B. E. Nieuwenhuys, Surf. Sci. 192 2-3 (1987) 438.
21. W. F. Lin, T. Iwasita, and W. Vielstich, J. Phys. Chem. B 103 16 (1999) 3250.
22. G. L. Nyberg, S. R. Bare, P. Hofmann, D. A. King, and M. Surman, Appl. Surf. Sci. 22-3 (1985) 392.
23. C. J. Baily, M. Surman, and A. E. Russell, Surf. Sci. 523 (2003) 111.

Chapter Eight – Conclusions and Further Work

8.1 Conclusions

The aim of this thesis was to investigate the bonding of small adsorbate molecules to platinum single crystal surfaces using UHV synchrotron far-infrared RAIRS and DFT calculations. The use of UHV synchrotron far-infrared RAIRS enabled the substrate-adsorbate vibration to be observed in a data collection time of a few minutes, rather than a number of hours as in other groups' experiments [1, 2]. The principal adsorbate molecule that was studied was carbon monoxide because of its large infrared absorption factor and its importance in the fuel cell process. DFT calculations were used to confirm the conclusions drawn from the CO far-infrared RAIRS experiments.

The reduced data acquisition time of far-infrared RAIRS using a synchrotron source is highlighted by the RAIR spectra reported in this thesis. This allowed even broad features to be seen, like the Pt(111)-CO_{bridge} stretch in Chapter four and the Pt(110)-benzene stretch in Chapter six.

Synchrotron radiation is orders of magnitude brighter than conventional black-body sources in the far-infrared region of the electromagnetic spectrum. This increased brightness enabled the far-infrared spectra reported in this thesis to be recorded at high resolution, which enabled peaks that were within 10 cm^{-1} of each other to be clearly resolved. This had a major impact on the RAIR spectra shown in Chapter five, as the clear resolution of the spectra with two peaks made the conclusions drawn from the work easier to make.

The RAIR spectra presented in Chapters four and five, clearly show that the Pt-CO stretching vibration is highly sensitive to both the co-ordination geometry of the CO adsorption site and the geometry of the underlying platinum substrate.

The change in co-ordination geometry gave rise to a significant difference in peak position and shape. The work on the Pt(111) surface showed that CO adsorbed in an atop site gave a Pt-CO stretch at 464 cm^{-1}, whereas the Pt-CO stretch for bridge-bonded CO was at 376 cm^{-1}. Also, the atop peak was much sharper than the bridge peak, with a FWHM value of 13 cm^{-1} compared to 19 cm^{-1}. The fact that the peak for bridge bonded CO is much lower in energy than the atop peak, and is also broader, shows that the CO is bound more weakly in bridge sites than atop sites on Pt(111).

The Pt-CO peak is also shown to be sensitive to the structure of the platinum substrate in the temperature dependant RAIR spectra presented in Chapter five. These spectra show two distinct peak positions from CO adsorbed in atop sites on the Pt(110)-(1x1) and Pt(110)-(1x2) substrates. This again shows the sensitivity of the Pt-CO stretching vibration to the platinum substrate structure, which, in the case of the Pt(110)-CO system, is further highlighted by the fact that identical mid-infrared RAIRS experiments by Sharma *et al.* [3] detected no difference in the C-O stretching peak position.

In the temperature dependant studies of the Pt(110)-CO system presented in Chapter five, another important observation is the development of the band attributed to the Pt-CO stretch of CO bonded in an atop site on the Pt(110)-(1x1) at 204 K. This band suggests the onset of some localised lifting of the reconstruction at a lower temperature than previously reported. The previously reported transition temperature of 250 K was based on LEED studies [4]. Since LEED is a technique that requires long range order, and RAIRS is not, the greater sensitivity of RAIRS than LEED allows this lifting of the Pt(110) reconstruction to be observed at a temperature 50 K lower than previously reported.

In the cases of benzene and pyridine adsorption on Pt(110) it was shown that both adsorbates could freely adsorb onto a surface partially covered with an amount of pre-adsorbed CO in an atop site, and that the peak from the pre-adsorbed CO could be observed. The observation of the Pt-CO peak means that

the dosing of either of these molecules can be used as a method of recording the Pt-CO peak from pre-adsorbed CO.

The combination of synchrotron far-infrared RAIRS with an electrochemical transfer system is unique. This enables surfaces to be characterised by typical UHV techniques, such as XPS and LEED, as well as electrochemical methods like cyclic voltammetry and CO electrooxidation, both of which are highly relevant to the issue of CO poisoning in fuel cells.

8.2 Further Work

To determine whether a Fermi resonance is present in the Pt(111)-$^{12}C^{16}O_{bridge}$ vibration a full set temperature dependant synchrotron far-infrared RAIRS experiments would need to be performed. Spectra covering the range 50 K to 300 K would be the most useful as this covers all the adsorption temperatures investigated by the work in this thesis and the work by Engström and Ryberg. It is anticipated that this suggested set of experiments would show just two bands in each spectrum, one at about 380 cm^{-1} and one at about 465 cm^{-1}, which could be assigned to the Pt-CO_{bridge} and Pt-CO_{atop} stretching vibrations respectively. If this was the case then no band due to a Fermi resonance would be seen and the theory of the Fermi resonance could be argued to be incorrect.

Further synchrotron far-infrared experiments investigating benzene adsorption and low and high coverage pyridine adsorption should be carried out in an environment containing significantly less CO, and with a more stable beam. This would lead to a less noisy spectrum where the only peaks present would be due to benzene or pyridine, and hence a better chance of detecting these peaks. A decrease in beam stability in particular leads to the recording of more noisy spectra, as highlighted by the high levels of noise in the spectra shown in this chapter, which were taken during a period of ring instabilities at the SRS.

It would also be interesting to undertake some UHV scanning tunnelling microscopy (STM) experiments on these Pt-benzene and Pt-pyridine systems. Since STM gives a real space map of the surface it should be possible to first of all gain an image of the platinum substrate and therefore know the positions of the surface platinum atoms. Then if another image of the surface, covering the same area, were taken after dosing either benzene or pyridine, this would show the geometry of the adsorbate molecules. A series of similar experiments and calculations have been carried out on analogous transition metal surfaces, in which the adsorption sites of benzene have been clearly determined [5-8]. Any tilting of the benzene or pyridine on the surface at room temperature could be determined by ARUPS or NEXAFS, as in the low temperature work by Zebisch *et al.* [9].

As pyridine was found not to be useful as a displacement molecule for CO on platinum surfaces, other molecules need to be tested for their suitability. The three most important criteria for suitability are effective displacement of CO from a platinum surface in UHV conditions (a useful way to test this would be to see if the displacement molecule had a higher desorption temperature than CO from the substrate surface), no detectable RAIRS features in the far-infrared region of the spectrum, and that the molecule is able to be pumped quickly from the UHV chamber. All molecules to be tested should be used in the place of pyridine in experiments that are the same as described in Section 7.3.2.

Since it was not possible to detect ruthenium in the XPS spectra after under potential deposition, this experiment needs to be repeated with some modifications. The most beneficial modification might be to increase the concentration of the ruthenium in the solution by a factor of about 100, thus increasing the likelihood of depositing ruthenium on the surface. This could overcome one of the problems encountered by using only 0.15 mM $RuCl_3$ in conjunction with the small contact area of the meniscus as compared to the large size of the sample used for the far-infrared RAIRS and XPS experiments. It would also be useful to re-design the electrochemical cell to give a larger meniscus size

and hence contact area, and therefore deposit ruthenium over a larger surface area. It might also be interesting to change the electrolyte from perchloric acid to sulphuric acid, as used by Davies and co-workers [10, 11].

It could also be helpful to try to use metal vapour deposition (MVD) to deposit ruthenium on the platinum surface in the UHV chamber before trying a UPD experiment, as MVD have been shown to be easier to implement and characterise [10, 11], and would give a useful set of data to compare future UPD results to.

Once ruthenium can be deposited onto the platinum surface by UPD, its coverage can be quantitatively monitored by XPS. Following this, far-infrared RAIR spectra of CO adsorbed on these surfaces can be recorded using the displacement method described in Section 7.3.2. Since the far-infrared region of the spectrum contains the substrate-CO stretching vibrations, which is far more sensitive to the bonding site of the CO [12], this will give a great amount of information on the exact nature of the bonding of CO on these mixed Pt-Ru substrates.

8.3 Final Statement

In summary, this thesis has shown that far-infrared RAIRS is a powerful technique to use in probing the substrate-adsorbate bond; the bond that is critical to the nature of the attachment of the adsorbed molecule to the surface. It has also been shown that synchrotron far-infrared RAIRS allows data in this part of the electromagnetic spectrum to be collected in a much faster time than for other techniques, e.g. thermal emission (TE) or using a black-body source, whilst maintaining a high level of sensitivity and resolution. These experiments, combined with high level DFT calculations, have also provided an improved understanding of the lifting of the Pt(110) reconstruction. The addition of liquid phase electrochemical studies to the UHV techniques present on the chamber and

the complementary calculations will give even more scope for a variety of experiments in the future.

8.4 References

1. U. Engstrom and R. Ryberg, Phys. Rev. Lett. 78 10 (1997) 1944.
2. U. Engstrom and R. Ryberg, J. Chem. Phys. 115 1 (2001) 519.
3. R. K. Sharma, W. A. Brown, and D. A. King, Surf. Sci. 414 1-2 (1998) 68.
4. S. Ferrer and H. P. Bonzel, Surf. Sci. 119 2-3 (1982) 234.
5. G. Treboux and M. Aono, J. Phys. Chem. B 101 23 (1997) 4620.
6. J. Yoshinobu, M. Kawai, I. Imamura, F. Marumo, R. Suzuki, H. Ozaki, M. Aoki, S. Masuda, S. Tanaka, M. Kamada, and M. Aida, J. Electron Spectrosc. Relat. Phenom. 88 (1998) 997.
7. M. Doering, H. P. Rust, B. G. Briner, and A. M. Bradshaw, Surf. Sci. 410 2-3 (1998) L736.
8. P. Sautet and M. L. Bocquet, Phys. Rev. B 53 8 (1996) 4910.
9. P. Zebisch, M. Stichler, P. Trischberger, M. Weinelt, and H. P. Steinruck, Surf. Sci. 396 1-3 (1998) 61.
10. J. C. Davies, B. E. Hayden, and D. J. Pegg, Electrochim. Acta 44 6-7 (1998) 1181.
11. J. C. Davies, B. E. Hayden, D. J. Pegg, and M. E. Rendall, Surf. Sci. 496 1-2 (2002) 110.
12. C. J. Baily, M. Surman, and A. E. Russell, Surf. Sci. 523 (2003) 111.